LARGE DEFORMATION FINITE ELEMENT ANALYSIS FOR POLYMER FORMING PROCESSES

By

WEINING SONG, B.Sc.

A Thesis

Submitted to the School of Graduate Studies

in Partial Fulfillment of the Requirements

for the Degree

Doctor of Philosophy

McMaster University

LARGE DEFORMATION FINITE ELEMENT ANALYSIS FOR POLYMER FORMING PROCESSES

獻給

我的妻子夏之明，
我的父母宋啓年，張亞平，

及

我的老師們

To

My wife Zhiming Xia,
my parents Qinian Song, and Yaping Zhang,

and

my Teachers

DOCTOR OF PHILOSOPHY — McMASTER UNIVERSITY

(Civil Engineering and Engineering Mechanics) — Hamilton, Ontario

TITLE: Large Deformation Finite Element Analysis for Polymer Forming Processes

AUTHOR: Weining Song, B.Sc. (Peking University, Beijing, P.R. China)

SUPERVISORS: Professors F.A. Mirza and J. Vlachopoulos

NUMBER OF PAGES: xiv, 169

ABSTRACT

The object of this work is to explore in depth a variety of polymer forming processes and to examine the behavior of polymers during processing by developing large deformation finite element models and computer tools for the numerical simulations of the processes.

Thermoforming, one of the major forming processes dealt with in this thesis, is the fabrication of numerous plastic products by use of heat, pressure and mold. Thermoforming is penetrating existing and new product categories due to ease of production, low costs, and the high performance of final products.

Axisymmetrical finite element models have been developed that include large deformation, large strain, moving boundaries, contact of polymer with rigid mold, deformation-dependent loading, free surface evolution, and material nonlinearities. The thermoplastics in the forming processes are considered as incompressible, hyperelastic materials, since there is little time for viscous dissipation. The incompressibility condition is accurately incorporated by employing the penalty method. No restriction of sheet thickness is made in the models for thermoforming so that thermoforming of single layer or multilayer composite sheets of finite thickness can be dealt with, as well as plug-assist forming of thick sheet. A simple, efficient method for passing the limit point is established in the finite element formulations, and for the first time the limit point in thermoforming is successfully simulated using this method. Numerical simulations compare well with analytical solutions for

simple geometries and experiments for thermoforming, plug-assist forming, combined plug-assist pre-stretching and vacuum forming, and compression forming. The important parameters in the processes which influence processing and products are studied, including the effects of material constants, boundary conditions, and processing sequence. For these processes, information of deformation and stress can be obtained by the developed computer models, such as deformed profile, thickness variation, the relationship between applied loading and deformation, and stress and strain variations at critical areas, which are important in process optimization and damage analysis.

The computer modeling and analysis provide a comprehensive understanding of these forming processes and could be valuable for industrial designers in the process of reducing trial-and-error procedures, optimizing their designs, minimizing material and cost, and maximizing product performance.

ACKNOWLEDGEMENTS

I wish to express my sincere and deepest appreciation to my supervisors Prof.s Farooque A. Mirza and John Vlachopoulos, for their constant guidance, valuable advice, criticism, encouragement and support throughout the research and preparation of this thesis. I want to extend this appreciation to Prof.s A.H. Hrymak, S. Pietruszczak, D.F. Stolle, for their valuable advice, thoughtful suggestions.

The financial assistances from the Department of Civil Engineering and Engineering Mechanics, and the School of Graduate Studies of McMaster University, the Natural Science and Engineering Research Council of Canada are gratefully acknowledged.

I am indebted to Janet Ryding and Rhonda MacDonald for their help in the preparation of this thesis. I also appreciate the help, encouragement and friendship from William and Barbara Corp.

Special thanks are due to my parents and my family for their love, encouragement and support.

Finally, I thank my wife, Zhiming, for her love, encouragement, direct help, understanding, moral and financial support towards completion of this thesis.

TABLE OF CONTENTS

LIST OF FIGURES

LIST OF TABLES

CHAPTER 1

INTRODUCTION

1.1 Polymer Forming Processes

As new materials, polymers have entered everyday life of human being. High performance thermoplastics have penetrated markets traditionally dominated by conventional engineering materials such as metals. Thermoforming is the fabrication of numerous plastic products by use of heat, pressure and mold. Engineering applications of thermoforming are increasing due to ease of production, low costs, and the high performance of final products.

In the process of thermoforming, a thermoplastic sheet, usually extruded from a sheet die, is heated close to the melting temperature of the polymer and formed into a mold cavity by use of pressure (or vacuum). One of the most important problems in this process is the determination and optimization of sheet thickness distribution which is a function of processing conditions and rheological properties of the softened plastic sheet.

Plug-assist forming is the process of stretching a heated thermoplastic sheet into a cavity by use of a plug. This pre-stretching process is used to promote uniformity of wall thickness distribution, allowing the formed part to have better structural properties such as high flexural strength and stiffness. Usually, after the plug completes its stroke, the cavity is sealed, and pressure (or vacuum) is applied until the sheet fills the cavity.

Generally, during forming processes, polymers behave viscoelastically and their deformation processes involve large deformation, large strain, large strain rate, contact with mold, and free surface evolution. However, in thermoforming and plug-assist forming, the processing is rapid and there is no time for viscous dissipation. Polymers undergo large elastic deformation.

Current challenges for polymer processing industry are to better understand the rheological behavior of polymers during forming and the flow, or deformation characteristics of processing, and to develop better process design (mold design, processing control design, etc.) so that higher performance products can be fabricated with less material waste and cost.

Advances in computer technology and numerical methods make it possible to solve and simulate complex problems, such as polymer forming processes, which, otherwise, could prove too expensive by trial and error experiments, or almost impossible to solve by other means. The finite element method has been proven to be one of the most powerful numerical methods to solve engineering problems. This thesis adopts the finite element method to simulate thermoforming, plug-assist forming and compression forming.

Due to the inherent material and deformation characteristics of polymer forming processes, nonlinear constitutive models, and nonlinear large deformation analysis are employed in the numerical simulation.

1.2 Aims and Thesis Outlines

The object of this work is to explore in depth a variety of polymer forming processes and to examine the behavior of polymers during processing by developing nonlinear finite element models and computer tools for the

numerical simulations of the processes.

The nonlinearities arising in the polymer forming operations are incorporated into our finite element models, including large deformation, large strain, moving boundaries, deformation-dependent loading, contact of polymer with solid mold, free surface evolution, and material nonlinearities. The thermoplastics in the forming processes are considered as incompressible, hyperelastic materials, since there is little time for viscous dissipation. The incompressibility condition is accurately incorporated by employing the penalty method. No restriction of sheet thickness is made in the models for thermoforming so that thermoforming of single layer or multilayer composite sheets of finite thickness can be dealt with, as well as plug-assist forming of thick sheet. A simple, efficient method for passing the limit point is established in the finite element formulations, and for the first time the limit point in thermoforming is successfully simulated using this method (Song et al. 1991 (a)). Detailed and comprehensive numerical simulations are compared with analytical solutions for simple geometries and experiments for thermoforming, plug-assist forming, combined plug-assist pre-stretching and vacuum forming, and compression forming. The important parameters which influence processing and products are studied, such as the effects of material constants, mold shape and processing sequence. For any of these processes, information of deformation and stress can be obtained by the developed computer models, including deformed profile, thickness variation, the relationship between applied loading and deformation, and stress and strain variations at critical areas, which are important in process optimization and damage analysis.

The computer modeling and analysis provide a comprehensive understanding of these forming processes and have the potential to be helpful for industrial designers in the process of optimizing their designs and reducing trial and error procedures.

Numerical simulation of polymer forming processes requires knowledge of the material behavior of polymers. In Chapter 2, typical deformation behavior of polymer solids and fluids are briefly described first. Then, the fundamentals of large deformation analysis are discussed, and three description methods of motion and their advantages in numerical analysis are compared. Tensor formulations of large deformation are given, as well as various stress measures and frame-independent stress rates. Nonlinear hyperelastic and viscoelastic constitutive equations for polymer solid and fluid are also presented.

Finite element analysis of large deformation based on the Lagrangian description is addressed in Chapter 3. Formulation of incremental loading and Newton-Raphson iteration for nonlinear problems is established, which takes into account bending, shearing, and membrane stretching. Deformation-dependent loading and its contribution to stiffness matrix are studied. The penalty method is used to approximate the incompressibility condition. Solution techniques and convergence criteria are described and simple numerical examples are given.

From Chapter 4 to Chapter 7, a variety of forming operations are analyzed, i.e., thermoforming, plug-assist forming, and compression forming. Polymers in these forming processes are considered as hyperelastic materials.

Thermoforming of single layer and multi-layer sheets are simulated in

Chapter 4. A historic review of numerical simulation of thermoforming is presented first. Specific material models (i.e., Mooney model and Ogden model) are described. Comparison of current simulation with analytical solutions for a simple large inflation problem confirms the validity of the finite element modeling. An efficient algorithm to pass the limit point is incorporated into the computer program and predictions are compared with experiments, including the benchmark tests of rubber sheets by Treloar (1944 b), which have not been numerically simulated before. The assumption of hyperelasticity was confirmed previously by experiments and is checked here by numerical study. Effects of material parameters on the formed product are discussed, as well as the determination of these parameters. The capability to simulate thermoforming of multilayer composite sheet is one of the unique advantages of current work.

Chapter 5 is devoted to contact problem. Contact without friction and with infinite friction are considered first, followed by discussion of contact with finite friction. Numerical schemes of various contact boundary problems are established and applied to the simulations of forming of circular cup and large rectangular part.

In Chapter 6, a brief review of the analysis of plug-assist forming is presented. A displacement-driven incremental algorithm is established to simulate plug-assist forming problems. Comprehensive comparisons of numerical simulations with the test results of Williams (1970) and Throne (1989) are conducted. A better understanding of plug-assist forming is achieved, such as the relationship of loading and deflection, the effects of material parameter and boundary condition on the formed part, and the strain states at different locations of the sheet. Combined vacuum forming and plug-assist pre-stretching is simulated

to study how the processing itself affects final thickness distribution. The computer model can provide detailed deformation and stress information, including thickness variation, extension ratios, and strain and stress contours, which could be useful to optimize forming design. Stress concentration at critical regions are also studied.

Chapter 7 is concerned with compression forming. A brief review of the state-of-art of compression forming problems is presented. Comparisons between simulations of compression without friction and with stick condition and analytical results are conducted. With Lagrangian description, material motion is easily traced. Fountain-like deformation patterns is predicted in the simulation and compared with experimental observations. Interfacial stress distribution is calculated. Compression forming of laminated composite can also be simulated with the current finite element model.

A summary of this thesis work is presented in Chapter 8. Conclusions about the numerical simulations of polymer forming processes are drawn and recommendations are provided.

CHAPTER 2
MATHEMATICAL MODELING OF FORMING PROCESSES

2.1 Deformation Characteristics of Polymer Solid and Fluid

Deformation characteristics of polymer solid and fluid are briefly discussed before attempts are made to construct constitutive models to describe the relationship between stress and deformation, and to model forming processes mathematically.

In Figures 2.1 and 2.2, flow curves of semicrystalline and tough, ductile amorphous thermoplastics (polymer solids) in the form of true strain vs. true stress are shown under constant strain rate and room temperature conditions. All materials shown in the figures are commercially available and are often used in solid-phase forming operations at temperatures below melting temperatures. Typical flow curves of metals are also shown in Figure 2.1 (f). Figure 2.1 is duplicated from Halldin and Lo (1985), while Figure 2.2 is sketched according to Ward (1983). Figures 2.1 and 2.2 show that polymer solids can undergo very large deformation before fracture even at room temperature, in contrast to metals. This is a unique feature of polymer solids. The thermoplastics shown experience rapid work hardening after initial nonlinear elastic deformation, while for the tough, ductile polymers (PC and PVC) and rubber-modified styrene (HIPS), there are strain softening regions following elastic deformation. The point where stress response transits from

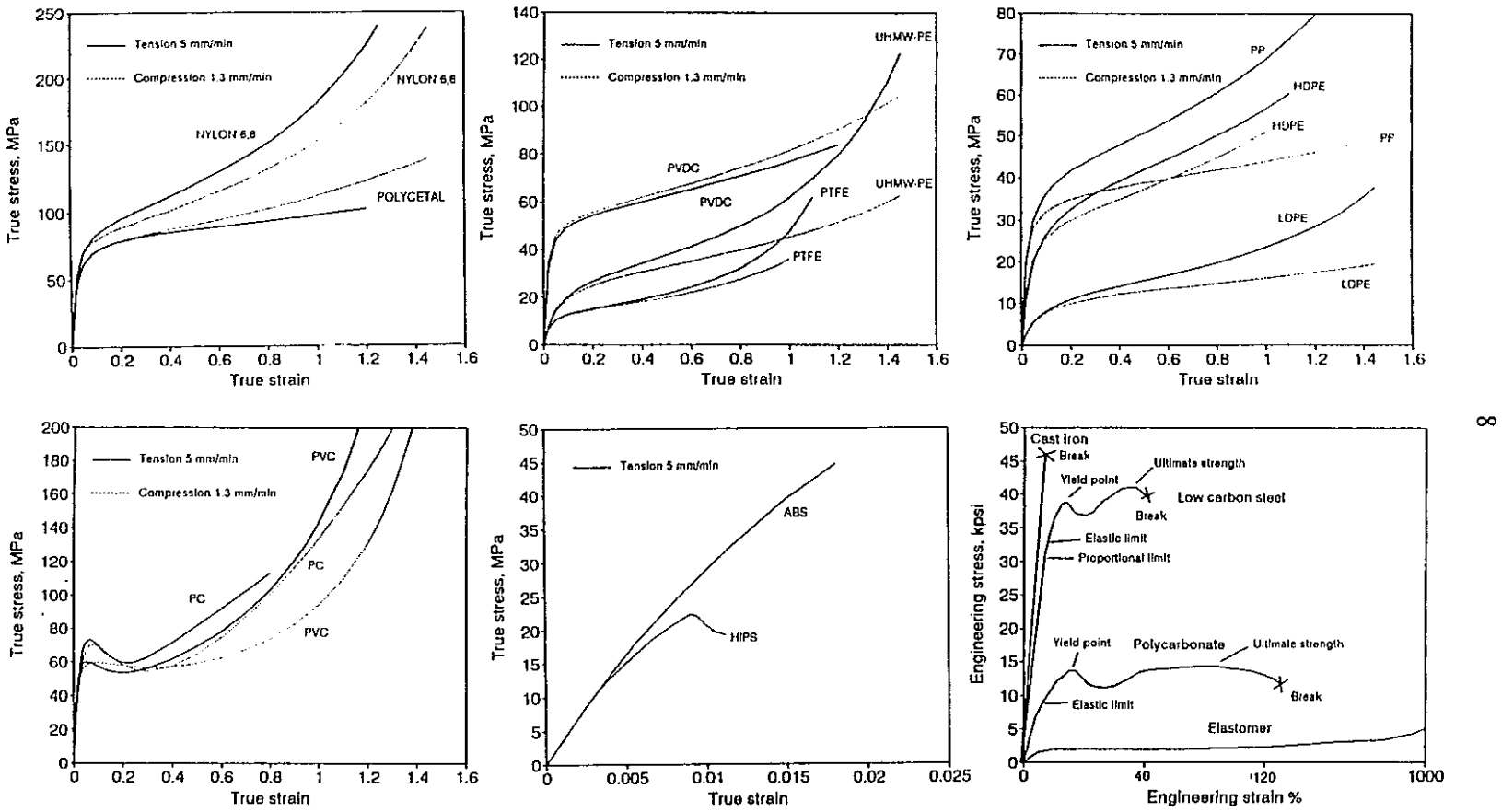

Figure 2.1 Flow curves of polymer solids at constant strain rates (T = 20 °C).

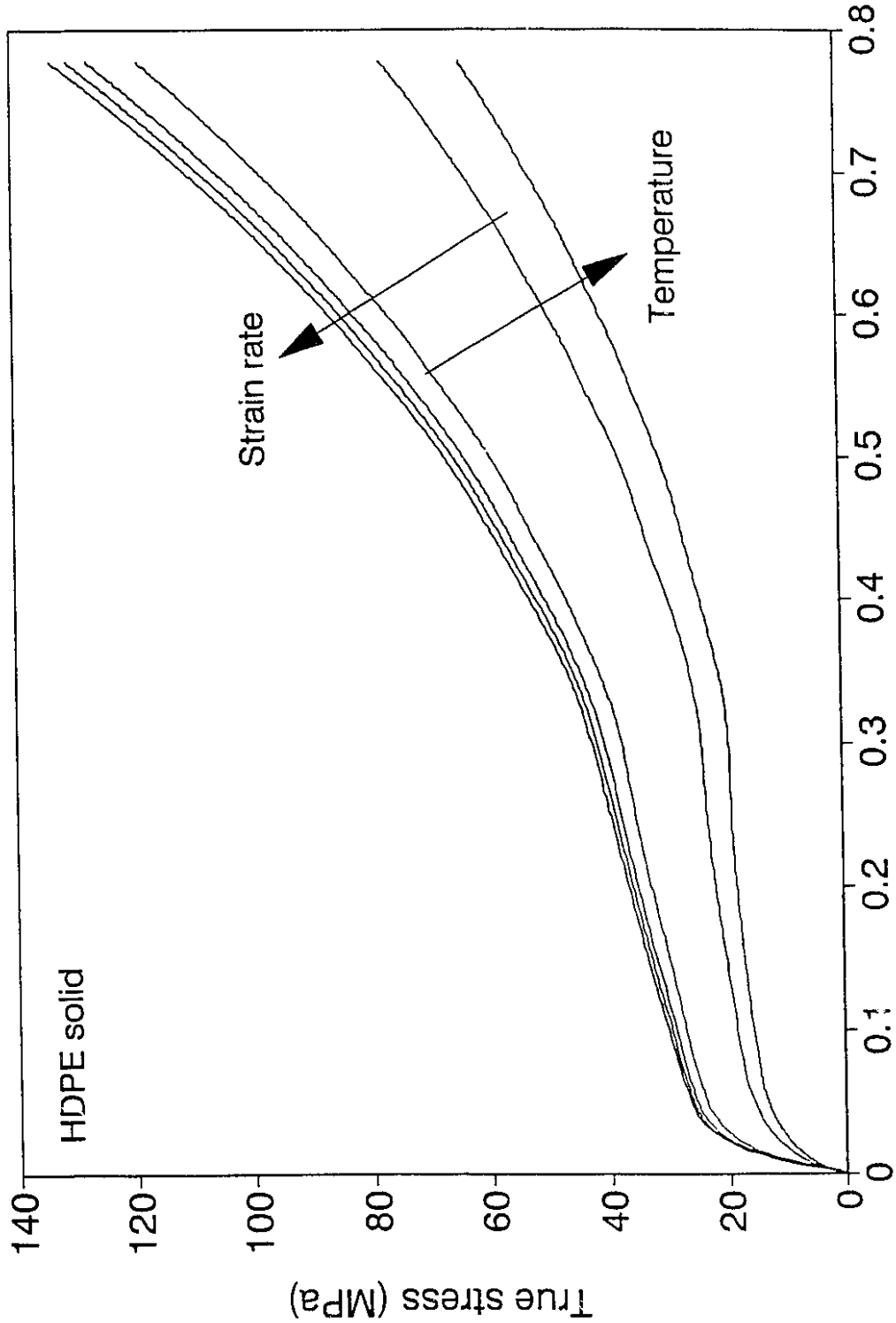

Figure 2.2 Rate- and temperature-dependent flow curves of polymer solid.

strain-hardening to strain softening is called upper yield point. Yielding is a characteristic of carbon steels and serves to introduce the concept of yield surface. For the thermoplastics shown in Figure 2.1, stress responses to strain gradually transit from nonlinear elastic to nonlinear inelastic responses. Again this phenomenon distinguishes polymer solids from metals. Figure 2.2 also demonstrates that the stress-strain behavior of polymers is strain rate dependent, as well as temperature dependent. When strain rate becomes very large, or, deformation process is very rapid, the flow curves appear to fall into an envelope, that is, there is an upper limit curve (Song, 1993).

Figure 2.3 shows the typical rheological behavior of polymer melts, which distinguish viscoelastic melts from Newtonian fluids, such as water. Of course, there is other behavior different from water. The figures reveal that viscosity of a polymer melt is a function of the rate of deformation, and that stress in a melt persists after deformation has ceased (stress relaxation). Fluid-phase polymer forming is a process where temperature is above the melting temperature of the polymer and polymer is molten.

2.2 Large Deformation Analysis

2.2.1 Description Methods of Motion

Polymer forming involves motion of polymeric material, or flow. Depending on flow characteristics, different description methods of motion can be utilized (Argyris et al. 1979). For modeling of most fluid-phase forming operations, such as extrusion and injection molding (Tucker, 1989, Vlachopoulos et al. 1992), Eulerian description is widely adopted. In thermoforming and blow molding, Lagrangian description is more suitable

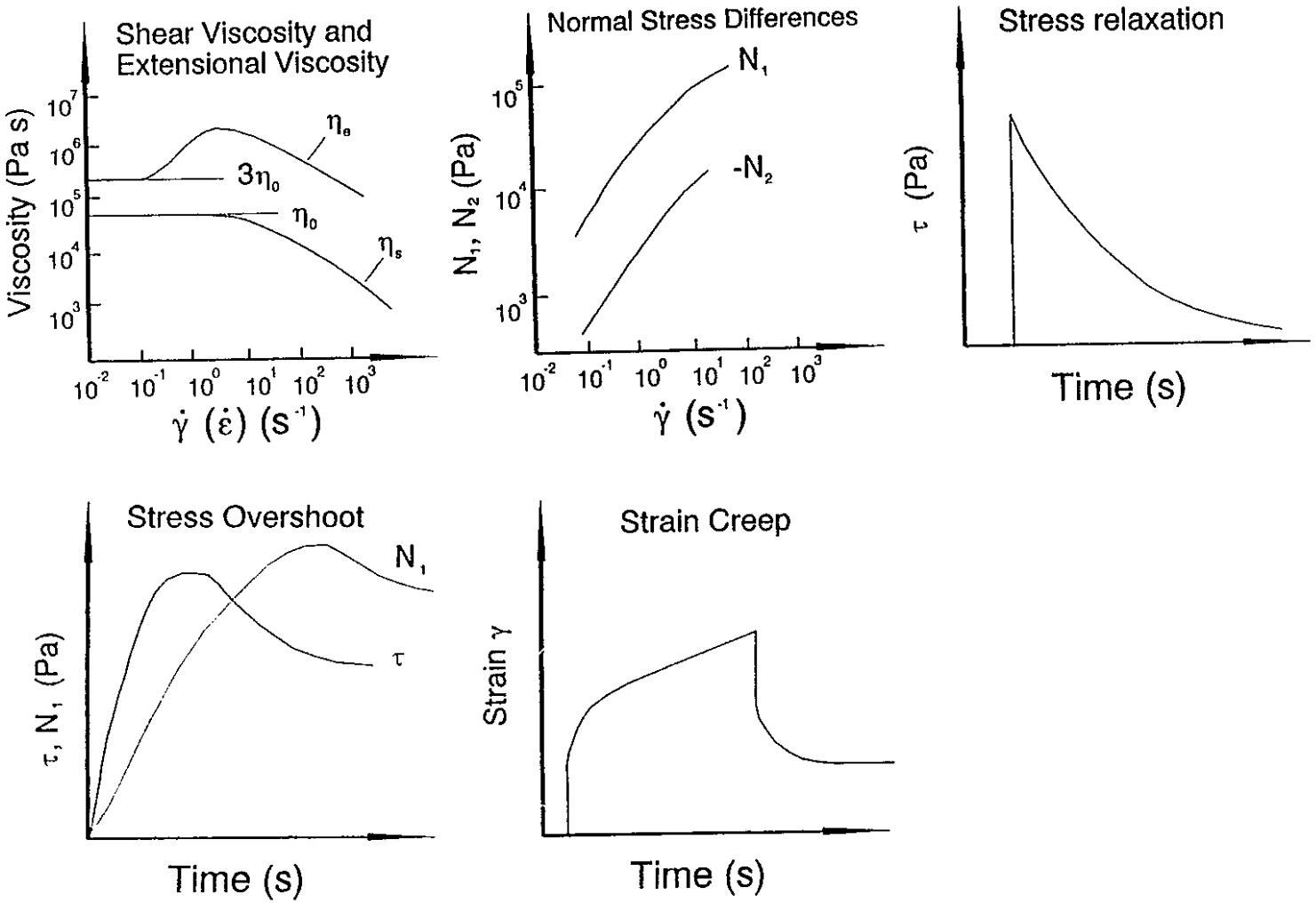

Figure 2.3 Flow characteristics of polymer melts.

(Song et al. 1991 (a), and deLorenzi and Taylor, 1991,). A mixed Eulerian and Lagrangian description has been used successfully to simulate compression forming (Mavridis, 1988) and injection molding (Mavridis et al. 1992).

In Lagrangian description, the motion of every material point of a body is traced from the beginning of process. The motion of a material point P is measured with respect to its position X in an arbitrarily chosen reference configuration, denoted as C_0, in Figure 2.4. Independent variables are position X (or ${}^0\mathrm{X}$) and time t. It should be noted that choice of reference is arbitrary, and such a choice should not affect the results of the analysis. If the reference configuration is taken as the configuration of the body at time $t = 0$, this description is called total Lagrangian (Argyris et al. 1979). If the reference is allowed to change with the motion and taken as the current configuration of the body at the current time t, it is known as updated Lagrangian description. Then the independent variables are the current position ${}^1\mathrm{x}$ and time τ (at configuration C_2), which is relative to the present time t.

In Eulerian description, material motion through a fixed region in space is determined as a function of time instead of determining deformation of every material element by following its motion in space. That is, attention is focused on what is happening in a fixed region in space as time progresses. Independent variables are the current position ${}^1\mathrm{x}$ and time t. For the material motion, ${}^1\mathrm{x}$ itself becomes dependent on time t, which, in fact, complicates material time derivatives.

In a mixed Eulerian and Lagrangian description, or arbitrary Lagrangian-Eulerian description, reference is allowed to move differently from material motion and the reference motion is controllable. This method is used

Lagrange strain $${}^{1}_{0}\bar{\bar{E}} = \left(\frac{\partial\, {}^{1}\mathbf{u}}{\partial\, {}^{0}\mathbf{X}}\right) + \left(\frac{\partial\, {}^{1}\mathbf{u}}{\partial\, {}^{0}\mathbf{X}}\right)^{T} + \left(\frac{\partial\, {}^{1}\mathbf{u}}{\partial\, {}^{0}\mathbf{X}}\right)\cdot\left(\frac{\partial\, {}^{1}\mathbf{u}}{\partial\, {}^{0}\mathbf{X}}\right)^{T}$$

Euler strain $${}^{1}\bar{\bar{\varepsilon}} = \left(\frac{\partial\, {}^{1}\mathbf{u}}{\partial\, {}^{1}\mathbf{x}}\right) + \left(\frac{\partial\, {}^{1}\mathbf{u}}{\partial\, {}^{1}\mathbf{x}}\right)^{T} - \left(\frac{\partial\, {}^{1}\mathbf{u}}{\partial\, {}^{1}\mathbf{x}}\right)\cdot\left(\frac{\partial\, {}^{1}\mathbf{u}}{\partial\, {}^{1}\mathbf{x}}\right)^{T}$$

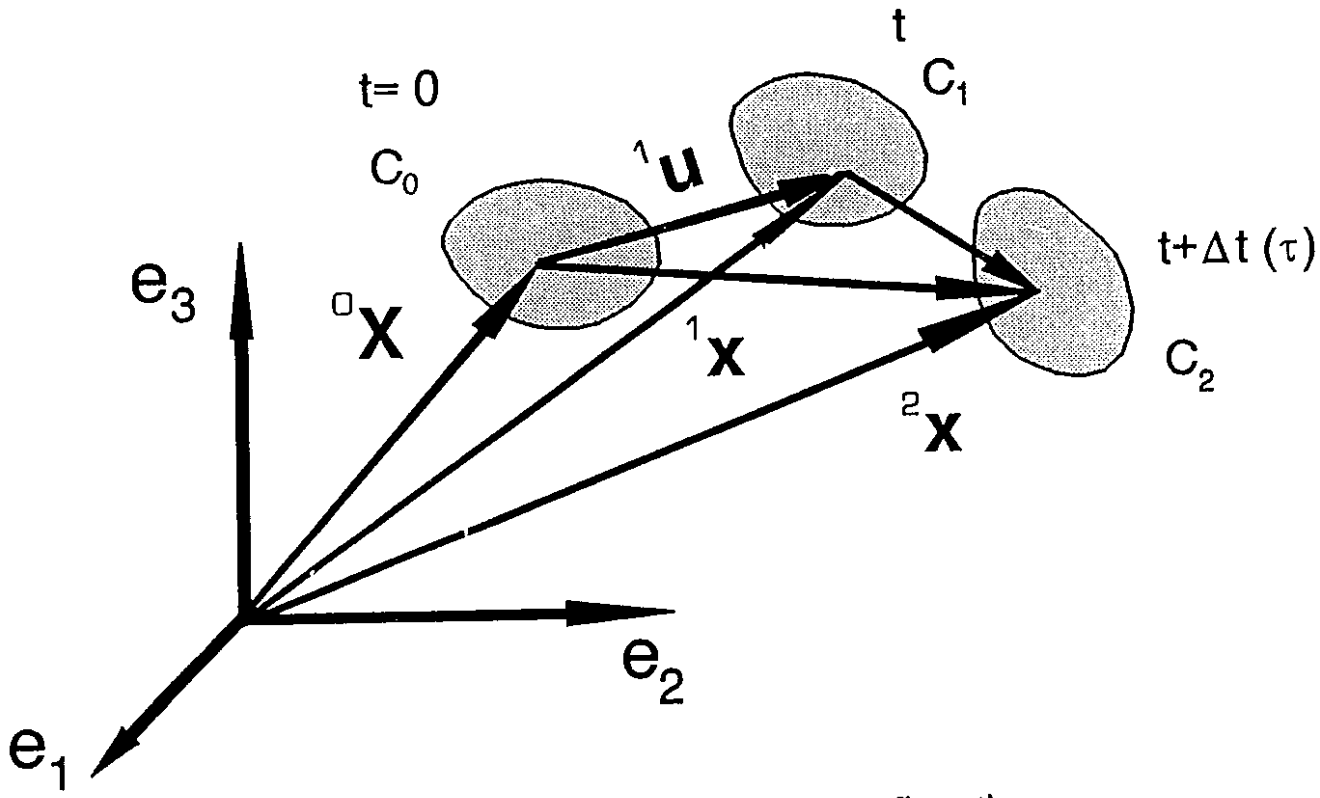

Figure 2.4 Large deformation configurations.

in fluid mechanics with a finite difference method (Hirt et al. 1974), and with a finite element method (Argyris et al. 1985) to solve Navier-Stokes equations, and also used in finite element analysis of fluid-solid interaction problems (Kennedy and Belytschko, 1981, Liu et al. 1986).

In finite element applications to nonlinear problems in continuum mechanics, especially large deformation problems, it is important to choose a description method which is suitable to describe the problem, and describes the problems in the most effective and simplest way. The Lagrangian approach requires less complex governing equations, compared to the pure Eulerian approach. This is due to the absence of convection terms, and simple updating techniques for path- and history-dependent materials in Lagrangian description. This is particularly suitable for thermoforming simulation and blow molding of polymer where a thin sheet undergoes large deformation. However, this approach is significantly limited when material deformation becomes very large such as steady fluid flow. Lack of control over finite element mesh movement results in distorted meshes with large changes in element dimensions, which adversely affects the accuracy of solution. But restoring to a pure Eulerian approach in which mesh remains stationary introduces other difficulties such as appropriate representation of free boundary. Eulerian mesh is less suited for domains whose boundaries, or interfaces, move substantially. Arbitrary Lagrangian-Eulerian description reserves the advantages of both approaches and is ideally suited for a variety of complex problems, such as squeezing flow, fluid-structure interaction, etc.

2.2.2 Kinematics of Motion

Large deformation analysis must be undertaken since in polymer forming operations, some extension ratios can be as large as 8, or 10. Total Lagrangian description of motion is used in this project. Each material point is traced throughout the whole process, and deformed body motion is measured with respect to its initial state. Detailed descriptions of large deformation analysis are presented by Hibbit et al. (1970), and Oden (1972).

We use ${}^0\mathbf{X}$, the initial position vector of a material point in the initial configuration C_0, as convected (material) coordinate system to describe motion, i.e.

$$\begin{cases} {}^1\mathbf{x} = {}^0\mathbf{X} + {}^1\mathbf{u}({}^0\mathbf{X}, t) \\ {}^2\mathbf{x} = {}^0\mathbf{X} + {}^2\mathbf{u}({}^0\mathbf{X}, t) \end{cases} \tag{2.2.1}$$

as shown in Figure 2.4, where ${}^1\mathbf{x}$ and ${}^2\mathbf{x}$ are the new locations at time t in configuration C_1 and at time $t+\Delta t$ in configuration C_2, respectively. $\mathbf{u}$ is displacement vector, and the left superscript represents the configuration where quantity is measured.

The deformation gradient from reference configuration C_0 to current configuration C_1 is defined by,

$${}^1_0\overline{\overline{\mathbf{F}}} = \frac{\partial {}^1\mathbf{x}}{\partial {}^0\mathbf{X}} \tag{2.2.2}$$

where ${}^1\mathbf{x}$ is, by assumption, the first vector of vector dyadic ${}^1_0\overline{\overline{\mathbf{F}}}$, and the left subscript indicates the reference configuration. Both the left superscript and subscript are sometimes omitted for simplicity.

The left and right Cauchy-Green deformation tensors are

$$\begin{cases} {}^1\overline{\overline{\mathbf{B}}} = {}^1\overline{\overline{\mathbf{F}}} \cdot {}^1\overline{\overline{\mathbf{F}}}^T \\ {}^1\overline{\overline{\mathbf{C}}} = {}^1\overline{\overline{\mathbf{F}}}^T \cdot {}^1\overline{\overline{\mathbf{F}}} \end{cases} \tag{2.2.3}$$

When moving from C_0 to C_1, deformation of an infinitesimal arc is

$$\begin{aligned} {}^1ds^2 - {}^0ds^2 &= {}^1\mathbf{x} \cdot {}^1\mathbf{x} - {}^0\mathbf{X} \cdot {}^0\mathbf{X} \\ &= 2\, {}^1_0\overline{\overline{\mathbf{E}}} : {}^0\mathbf{X}\, {}^0\mathbf{X} = 2\, \gamma_{ij}\, {}^0X_i\, {}^0X_j \\ &= 2\, {}^1\overline{\overline{\varepsilon}} : {}^1\mathbf{x}\, {}^1\mathbf{x} = 2\, \varepsilon_{ij}\, {}^1x_i\, {}^1x_j \end{aligned} \tag{2.2.4}$$

where the Lagrange strain tensor is

$${}^1_0\overline{\overline{\mathbf{E}}} = \frac{1}{2}\left({}^1\overline{\overline{\mathbf{C}}} - \overline{\overline{\mathbf{I}}}\right) = \frac{1}{2}\left[\left(\frac{\partial^1\mathbf{u}}{\partial^0\mathbf{X}}\right) + \left(\frac{\partial^1\mathbf{u}}{\partial^0\mathbf{X}}\right)^T + \left(\frac{\partial^1\mathbf{u}}{\partial^0\mathbf{X}}\right)^T \cdot \left(\frac{\partial^1\mathbf{u}}{\partial^0\mathbf{X}}\right)\right] \tag{2.2.5}$$

$\overline{\overline{\mathbf{I}}}$ is identity tensor, and the Euler strain tensor is

$${}^1\overline{\overline{\varepsilon}} = \frac{1}{2}\left(\overline{\overline{\mathbf{I}}} - {}^1\overline{\overline{\mathbf{B}}}^{-1}\right) = \frac{1}{2}\left[\left(\frac{\partial^1\mathbf{u}}{\partial^1\mathbf{x}}\right) + \left(\frac{\partial^1\mathbf{u}}{\partial^1\mathbf{x}}\right)^T - \left(\frac{\partial^1\mathbf{u}}{\partial^1\mathbf{x}}\right)^T \cdot \left(\frac{\partial^1\mathbf{u}}{\partial^1\mathbf{x}}\right)\right] \tag{2.2.6}$$

Eq.s (2.2.4) - (2.2.6) indicates that the same deformation can be measured by different strain tensors with respect to the initial configuration, or the current state, which corresponse to different description methods (Figure 2.4). In small deformation case, the third term of eq.(2.2.5) and eq.(2.2.6) is negligible, and ${}^1\mathbf{x} \simeq {}^0\mathbf{X}$. Then both strain measures are the same.

The three invariants of Cauchy-Green deformation tensor $\overline{\overline{\mathbf{C}}}$ are

$$\begin{cases} I_1 = \overline{\overline{\mathbf{C}}} : \overline{\overline{\mathbf{I}}} = \lambda_1^2 + \lambda_2^2 + \lambda_3^2 \\ I_2 = \frac{1}{2!}\, \overline{\overline{\mathbf{C}}} \underset{\times}{\times} \overline{\overline{\mathbf{C}}} : \overline{\overline{\mathbf{I}}} = \lambda_1^2\, \lambda_2^2 + \lambda_3^2\, (\lambda_1^2 + \lambda_2^2) \\ I_3 = \frac{1}{3!}\, \overline{\overline{\mathbf{C}}} \underset{\times}{\times} \overline{\overline{\mathbf{C}}} : \overline{\overline{\mathbf{C}}} = \lambda_1^2\, \lambda_2^2\, \lambda_3^2 \end{cases} \tag{2.2.7}$$

where λ_1, λ_2, λ_3 are three principal stretch ratios. Symbols " : " and " $\underset{\times}{\times}$ " represent double dot (scalar) product and double cross product of tensors, respectively (Bird et al. 1987). The incompressibility condition is

$$I_3 = 1 \tag{2.2.8}$$

The above symbolic operations are easy to understand. To implement

calculation, however, certain coordinate systems have to be used. Generally, curvilinear coordinate system is established. The covariant and contravariant base vectors of configuration C_0 are

$$\mathbf{g}_i = \frac{\partial^0 \mathbf{X}}{\partial^0 X^i}, \qquad \mathbf{g}^i = \frac{\partial^0 X^i}{\partial^0 \mathbf{X}} \qquad i=1,\ 2,\ 3 \tag{2.2.9}$$

The identity tensor

$$\bar{\mathbf{I}} = \mathbf{g}^r\, \mathbf{g}_r = \mathbf{g}_s \mathbf{g}^s = g_{ij}\mathbf{g}^i\mathbf{g}^j = g^{ij}\mathbf{g}_i\mathbf{g}_j \tag{2.2.10}$$

is the metric tensor of configuration C_0. $g_{ij} = \mathbf{g}_i \cdot \mathbf{g}_j$. In C_1, the covariant and contravariant base vectors are

$$\mathbf{G}_i = \frac{\partial^1 \mathbf{x}}{\partial^0 X^i}, \qquad \mathbf{G}^i = \frac{\partial^0 X^i}{\partial^1 \mathbf{x}} \qquad i=1,\ 2,\ 3 \tag{2.2.11}$$

then

$${}^1\bar{\mathbf{F}} = \mathbf{G}_j\, \mathbf{g}^j \tag{2.2.12}$$

$${}^1\bar{\mathbf{C}} = G_{ij}\, \mathbf{g}^i\, \mathbf{g}^j \tag{2.2.13}$$

$${}^1\bar{\mathbf{B}} = g^{ij}\, \mathbf{G}_i\, \mathbf{G}_j \tag{2.2.14}$$

$${}^1\bar{\mathbf{E}} = \gamma_{ij}\, \mathbf{g}^i\, \mathbf{g}^j = \frac{1}{2}\,(G_{ij} - g_{ij})\, \mathbf{g}^i\, \mathbf{g}^j \tag{2.2.15}$$

while the inverse of ${}^1\bar{\mathbf{F}}$ is

$${}^1\bar{\mathbf{F}}^{-1} = \frac{\partial^0 \mathbf{X}}{\partial^1 \mathbf{x}} = \mathbf{g}_i\, \mathbf{G}^i \tag{2.2.16}$$

and

$${}^1\bar{\mathbf{B}}^{-1} = {}^1\bar{\mathbf{F}}^{-T} \cdot {}^1\bar{\mathbf{F}}^{-1} = g_{ij}\, \mathbf{G}^i\, \mathbf{G}^j \tag{2.2.17}$$

$${}^1\bar{\varepsilon} = \varepsilon_{ij}\, \mathbf{G}^i\, \mathbf{G}^j = \frac{1}{2}\,(G_{ij} - g_{ij})\, \mathbf{G}^i\, \mathbf{G}^j \tag{2.2.18}$$

In cartesian coordinate system,

$$F_{ij} = \frac{\partial x_i}{\partial X_j} = \delta_{ij} + \frac{\partial u_i}{\partial X_j} \tag{2.2.19}$$

$$\gamma_{ij} = \frac{1}{2}\left[\frac{\partial u_i}{\partial X_j} + \frac{\partial u_j}{\partial X_i} + \frac{\partial u_i}{\partial X_j}\cdot\frac{\partial u_j}{\partial X_i}\right] \tag{2.2.20}$$

When simple deformation is considered, such as uniaxial, or equibiaxial extension, simple relations between different strains and extension ratios can be obtained. In these cases, or in the principal directions of deformation, Lagrange and Euler strains are

$$\gamma_{ii} = \frac{1}{2}(\lambda_i^2 - 1),\ \varepsilon_{ii} = \frac{1}{2}\left(1 - \frac{1}{\lambda_i^2}\right) \quad (i=1,2,3,\text{ no summation}) \tag{2.2.21a}$$

and true strain (Hencky strain) is

$$e_i = \int_0^l dl/l = ln(\lambda_i) \tag{2.2.21b}$$

For axisymmetric problems, we label the location of an arbitrary material particle P in a fixed Cartesian reference system $(\mathbf{e}_1, \mathbf{e}_2, \mathbf{e}_3)$ by cylindrical coordinates

$$\begin{cases} {}^0\mathbf{X} = \{\ R,\ Z,\ \Theta\ \}^T = R\cos\Theta\ \mathbf{e}_1 + R\sin\Theta\ \mathbf{e}_2 + Z\ \mathbf{e}_3 \\ {}^1\mathbf{x} = \{\ r,\ z,\ \theta\ \}^T = r\cos\theta\ \mathbf{e}_1 + r\sin\theta\ \mathbf{e}_2 + z\ \mathbf{e}_3 \end{cases} \tag{2.2.22}$$

and

$$\begin{cases} r = r\ (R,Z) = R + u_r(R,Z) \\ z = z\ (R,Z) = Z + u_z(R,Z) \\ \theta = \Theta \end{cases} \tag{2.2.23}$$

where u_r, u_z are the displacement components along r and z directions.

The covariant and contravariant forms of the metric tensor $\overline{\overline{\mathbf{I}}}$ are,

$$g_{ij} = \mathbf{g}_i \cdot \mathbf{g}_j = \begin{bmatrix} 1 & 0 & 0 \\ 0 & 1 & 0 \\ 0 & 0 & R^2 \end{bmatrix} \tag{2.2.24}$$

$$g^{ij} = \mathbf{g}^i \cdot \mathbf{g}^j = \begin{bmatrix} 1 & 0 & 0 \\ 0 & 1 & 0 \\ 0 & 0 & 1/R^2 \end{bmatrix} \tag{2.2.25}$$

The covariant components of Lagrange strain are given by

$$\begin{cases} \gamma_{\alpha\beta} = \frac{1}{2}\left(u_{\alpha,\beta} + u_{\beta,\alpha} + u_{\lambda,\alpha}u_{\lambda,\beta} \right) \\ \gamma_{\alpha 3} = 0 \qquad \alpha,\ \beta,\ \lambda = 1,\ 2 \\ \gamma_{3\,3} = \frac{1}{2}\left(r^2 - R^2 \right) \end{cases} \tag{2.2.26}$$

where $u_{\alpha,\beta} = \partial^1 u_\alpha / \partial^0 X^\beta$, $u_1 = r - R$, and $u_2 = z - Z$. Here covariant base vectors $\mathbf{g}_1$ and $\mathbf{g}_2$ are identical to contravariant base vectors $\mathbf{g}^1$ and $\mathbf{g}^2$, and both are unit vectors. Whereas $\mathbf{g}_3$ and $\mathbf{g}^3$ are not unit vectors. We prefer to have strain components expressed in unit base vectors. We let

$$\mathbf{a}_i = \frac{\mathbf{g}_i}{\| \mathbf{g}_i \|}, \text{ and } \mathbf{a}^i = \frac{\mathbf{g}^i}{\| \mathbf{g}^i \|} \quad (\text{no summation}) \tag{2.2.27}$$

then $\mathbf{a}_\alpha = \mathbf{g}_\alpha = \mathbf{a}^\alpha = \mathbf{g}^\alpha$, $\alpha = 1, 2$. $\mathbf{a}_3 = \frac{1}{R}\mathbf{g}_3$, and $\mathbf{a}^3 = R\,\mathbf{g}^3$. Furthermore, $a_{ij} = \mathbf{a}_i \cdot \mathbf{a}_j = \delta_{ij}$ and $a^{ij} = \mathbf{a}^i \cdot \mathbf{a}^j = \delta^{ij}$.

This coordinate system is adopted, in which covariant components of Lagrange strain are given by

$$\begin{cases} \gamma_{\alpha\beta} = \frac{1}{2}\left(u_{\alpha,\beta} + u_{\beta,\alpha} + u_{\lambda,\alpha}u_{\lambda,\beta} \right) \\ \gamma_{\alpha 3} = 0 \qquad \alpha,\ \beta,\ \lambda = 1,\ 2 \\ \gamma_{3\,3} = \frac{1}{2}\left(r^2 / R^2 - 1 \right) \end{cases} \tag{2.2.28}$$

The three principal stretch ratios, in radial, meridional, and circumferential directions, are obtained by solving $d^1 s^2 = \lambda^2\, d^0 s^2$.

$$\begin{cases} \lambda_1^2 = \left(1 + \gamma_{11} + \gamma_{2\,2} \right) + \left[(\gamma_{11} + \gamma_{22})^2 - \phi \right]^{1/2} \\ \lambda_2^2 = \left(1 + \gamma_{11} + \gamma_{2\,2} \right) - \left[(\gamma_{11} + \gamma_{22})^2 - \phi \right]^{1/2} \\ \lambda_3^2 = 1 + 2\,\gamma_{33} = \frac{r^2}{R^2} \end{cases} \tag{2.2.29}$$

and the three invariants of $\overline{\overline{\mathbf{C}}}$ are,

$$\begin{cases} I_1 = 3 + 2\,(\,\gamma_{11} + \gamma_{22} + \gamma_{33}) \\ I_2 = 2\,(\,1 + 2\,\gamma_{33})\,(\,1 + \gamma_{11} + \gamma_{22}) + \psi \\ I_3 = (\,1 + 2\,\gamma_{33})\,\psi \end{cases} \tag{2.2.30}$$

where

$$\begin{cases} \phi = 4\,(\,\gamma_{11}\gamma_{22} - \gamma_{12}\,\gamma_{21}) \\ \psi = 1 + 2\,(\,\gamma_{11} + \gamma_{22}) + \phi \end{cases} \tag{2.2.31}$$

$$\overline{\overline{C}} = G_{ij}\,\mathbf{g}^i\mathbf{g}^j = G_{ij}\,\|\,\mathbf{g}^i\|\,\|\,\mathbf{g}^j\|\,\mathbf{a}^i\mathbf{a}^j = A_{ij}\,\mathbf{a}^i\mathbf{a}^j \tag{2.2.32}$$

$$\overline{\overline{C}}^{-1} = G^{ij}\,\mathbf{g}_i\mathbf{g}_j = G^{ij}\,\|\,\mathbf{g}_i\|\,\|\,\mathbf{g}_j\|\,\mathbf{a}_i\mathbf{a}_j = A^{ij}\,\mathbf{a}_i\mathbf{a}_j \tag{2.2.33}$$

$$A_{ij} = \begin{bmatrix} 1+2\gamma_{11} & 2\gamma_{12} & 0 \\ 2\gamma_{21} & 1+2\gamma_{22} & 0 \\ 0 & 0 & 1+2\gamma_{33} \end{bmatrix} \tag{2.2.34}$$

$$A^{ij} = \frac{1}{\psi}\begin{bmatrix} 1+2\gamma_{22} & -2\gamma_{12} & 0 \\ -2\gamma_{21} & 1+2\gamma_{11} & 0 \\ 0 & 0 & \psi/(1+2\gamma_{33}) \end{bmatrix} \tag{2.2.35}$$

2.3 Stress Tensors

If $\mathbf{f}$ is the force per unit area acting on any surface point ${}^1\mathbf{x}$ in the current configuration C_1 with normal vector $\mathbf{n}$, then $\mathbf{f}$ is given by dot-product between surface normal $\mathbf{n}$ and stress tensor $\overline{\overline{\sigma}}$, evaluated at the point ${}^1\mathbf{x}$

$$\mathbf{f} = \mathbf{n} \cdot \overline{\overline{\sigma}} \tag{2.3.1}$$

This is called the Cauchy stress tensor principle and $\overline{\overline{\sigma}}$ is called Cauchy stress tensor. According to this principle the stress tensor $\overline{\overline{\sigma}}$ specifies completely the state of stress at any place ${}^1\mathbf{x}$ in the continuum, i.e. it determines completely all stress vectors as linear functions of $\overline{\overline{\sigma}}$.

The balance of linear momentum principle states at the current state

C_1 there is

$$\frac{d}{dt}\int_{{}^1V} {}^1\rho\ \mathbf{v}\ d{}^1V = \int_{{}^1A} \mathbf{f}\ d{}^1A + \int_{{}^1V} {}^1\mathbf{b}\ d{}^1V \tag{2.3.2}$$

where $\mathbf{v}$, ${}^1\mathbf{b}$ are velocity and body force vectors, ${}^1V$ and ${}^1A$ are the volume and surface area of the continuum.

Utilizing eq.(2.3.1) and through simple calculation, we have that eq.(2.3.2) is satisfied for any volume ${}^1V$ if and only if

$${}^1\rho\ \frac{d\mathbf{v}}{dt} = \frac{\partial\cdot\bar{\bar{\sigma}}}{\partial\,{}^1\mathbf{x}} + {}^1\mathbf{b} \quad \text{in } {}^1V \tag{2.3.3}$$

The balance of angular momentum principle for isotropic materials results in

$$\bar{\bar{\sigma}} \times \bar{\bar{I}} = \mathbf{0}, \text{ or } \bar{\bar{\sigma}}^T = \bar{\bar{\sigma}}\ (\sigma_{ij} = \sigma_{ji}) \tag{2.3.4}$$

$\bar{\bar{\sigma}}$ can be written as

$$\bar{\bar{\sigma}} = \sigma_M \bar{\bar{I}} + \bar{\bar{\tau}} \tag{2.3.5}$$

where $\sigma_M \bar{\bar{I}}$ is an isotropic tensor, $\sigma_M = \frac{1}{3}\ \bar{\bar{\sigma}} : \bar{\bar{I}} = \frac{1}{3}\ \sigma_{kk}$ represents mean stress, and $\bar{\bar{\tau}}$ is called the extra-stress tensor, or deviatoric stress tensor, $\bar{\bar{\tau}} = \bar{\bar{\sigma}} - \sigma_M \bar{\bar{I}}$.

If the balance eq.(2.3.2) is written with respect to reference configuration C_0, the pertinent quantities appearing in this equation (body force, stress vector, etc.) have to be referred to the reference state.

The Cauchy stress is transferred to the first Piola-Kirchhoff stress tensor $\bar{\bar{T}}$ (unsymmetrical), or the second Piola-Kirchhoff stress tensor $\bar{\bar{S}}$ (symmetrical):

$${}^1_0\bar{\bar{T}} = \frac{{}^1\rho}{{}^0\rho}\ \bar{\bar{F}}^{-1} \cdot {}^1\bar{\bar{\sigma}} \tag{2.3.6}$$

$$\overset{1=}{{}_0\mathbf{S}} = \frac{{}^1\rho}{{}^0\rho}\,\overset{=-1}{\mathbf{F}}\cdot{}^1\overset{=}{\sigma}\cdot\overset{=-T}{\mathbf{F}} \tag{2.3.7}$$

$\overset{1=}{{}_0\mathbf{T}}$ and $\overset{1=}{{}_0\mathbf{S}}$ are measured in C_1, but referred to C_0. The physical significance of these stress tensors are illustrated by a simple example.

Considering a uniaxial extension test of a bar, as shown in Figure 2.5. f is external force. A_0, A, L_0 and L are original (undeformed) cross-section area, deformed area, original length, and the deformed length, respectively. $\lambda = \lambda_1 = L/L_0$ represents extension ratio. The non-zero components of deformation gradient $\overset{=}{\mathbf{F}}$ are $F_{11} = \lambda$, $F_{22} = F_{33} = 1/\sqrt{\lambda}$. Incompressibility is assumed for the material, i.e., ${}^0\rho\ A_0\ L_0 = {}^1\rho\ A\ L$, ${}^0\rho = {}^1\rho$. Therefore,

$$\sigma_{11} = \frac{f}{A} = \frac{f}{A_0}\,\lambda, \tag{2.3.8}$$

$$T^{11} = \frac{{}^0\rho}{{}^1\rho}\,F_{11}^{-1}\,\sigma_{11} = \frac{f}{A_0}, \text{ and} \tag{2.3.9}$$

$$S^{11} = T^{11}\cdot F_{11}^{-1} = \frac{f}{A_0}\cdot\frac{1}{\lambda}. \tag{2.3.10}$$

that is the Cauchy stress σ_{11} is true stress, while the 1st Piola-Kirchhoff stress T^{11} represents engineering stress, the 2nd Piola- Kirchhoff stress S^{11}, the engineering stress divided by extension ratio.

2.4 Material Rates of Stress Tensors under Large Deformation

When viscoelastic behaviors of polymeric material are examined, changes of deformation and stresses with time must be considered.

Time-rate of deformation gradient $\overset{=}{\mathbf{F}}({}^0\mathbf{X}, t)$ is

$$\frac{d\overset{=}{\mathbf{F}}}{dt} = \overset{=}{\mathbf{L}}\cdot\overset{=}{\mathbf{F}} \tag{2.4.1}$$

where velocity gradient $\overset{=}{\mathbf{L}}$ is

$$\overset{=}{\mathbf{L}} = \frac{\partial^1\mathbf{v}}{\partial^1\mathbf{x}} = \overset{=}{\mathbf{D}} + \overset{=}{\mathbf{W}} \tag{2.4.2}$$

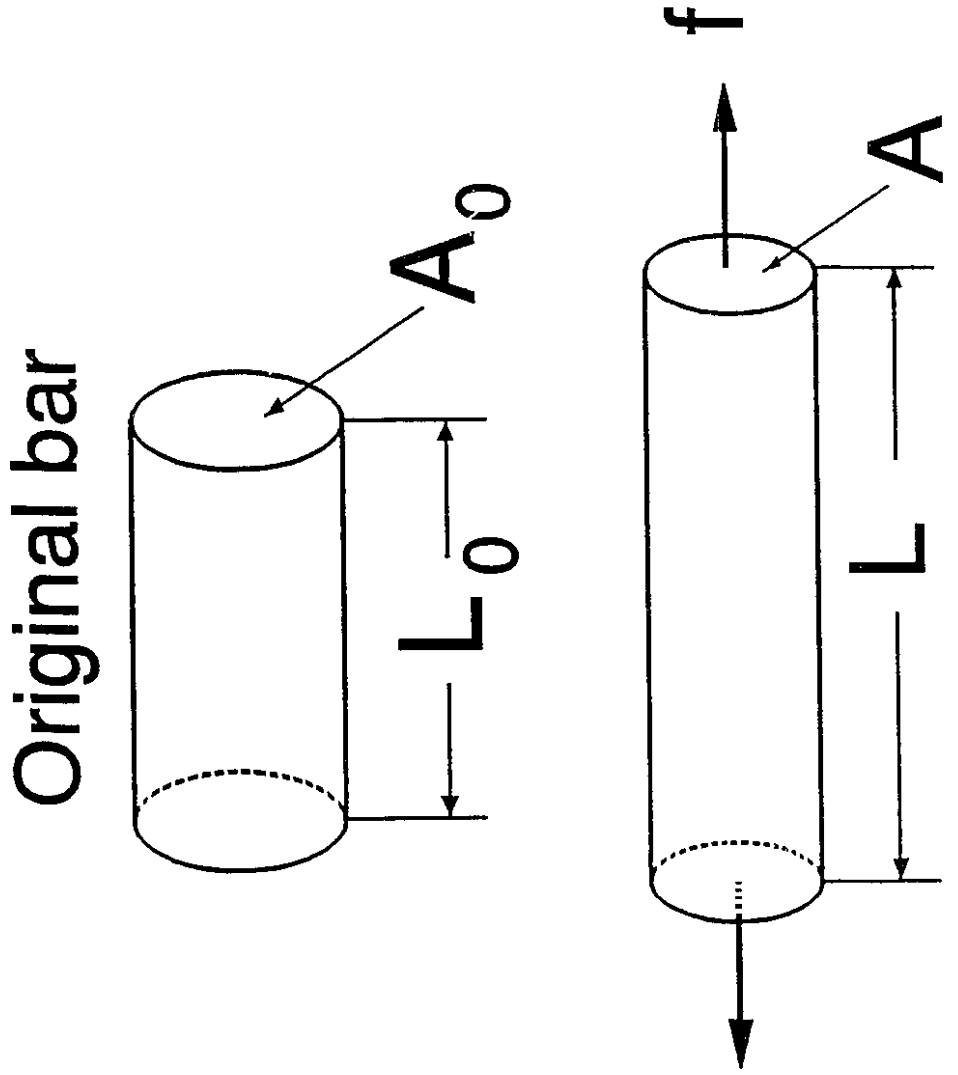

Figure 2.5 Geometry of a simple tensile test.

and

$$\overline{\overline{\mathbf{D}}} = \frac{1}{2}\left(\overline{\overline{\mathbf{L}}} + \overline{\overline{\mathbf{L}}}^{T}\right) \tag{2.4.3}$$

$$\overline{\overline{\mathbf{W}}} = \frac{1}{2}\left(\overline{\overline{\mathbf{L}}} - \overline{\overline{\mathbf{L}}}^{T}\right) \tag{2.4.4}$$

denote the rate of deformation tensor, and spin (vorticity) tensor.

The material rates of Lagrange strain and Euler strain tensors are

$$\frac{d\overline{\overline{\mathbf{E}}}}{dt} = \overline{\overline{\mathbf{F}}}\cdot\overline{\overline{\mathbf{D}}}\cdot\overline{\overline{\mathbf{F}}}^{T} = \frac{1}{2}\left[\overline{\overline{\mathbf{L}}}^{T}\cdot\overline{\overline{\mathbf{C}}} + \overline{\overline{\mathbf{C}}}\cdot\overline{\overline{\mathbf{L}}}\right] \tag{2.4.5}$$

and

$$\frac{d\overline{\overline{\varepsilon}}}{dt} = \overline{\overline{\mathbf{D}}} - \left(\overline{\overline{\mathbf{L}}}\cdot\overline{\overline{\varepsilon}} + \overline{\overline{\varepsilon}}\cdot\overline{\overline{\mathbf{L}}}^{T}\right) \tag{2.4.6}$$

Any mechanical event, which consists of a pair (x, t), can be observed from two different frames of reference (O^*, $\mathbf{x}^*$) and (O, x) with different timing devices t^* and t. The objectivity of physical laws, or the principle of material frame-indifference, states that any physical laws should be the same no matter where the event is observed. If (O^*, $\mathbf{x}^*$, t^*) $\longmapsto$ (O, x, t) denotes a mapping between the two frames, then

$$\begin{cases} \mathbf{x}^*(t^*) = \mathbf{c}(t) + \mathbf{x}\cdot\overline{\overline{\mathbf{Q}}}(t) \\ t^* = t + a \end{cases} \tag{2.4.7}$$

where $\mathbf{c}(t)$, $\overline{\overline{\mathbf{Q}}}(t)$, and a represent a time-dependent translation, time-dependent orthogonal transformation and a time shift. $\overline{\overline{\mathbf{Q}}}(t)\cdot\overline{\overline{\mathbf{Q}}}^{T}(t) = \overline{\overline{\mathbf{I}}}$.

Quantities that are invariant to different observers in different frames of reference are called frame-indifferent, or frame-independent. If tensor $\overline{\overline{\mathbf{H}}}$ is such a quantity, then

$$\overline{\overline{\mathbf{H}}}^{*} = \overline{\overline{\mathbf{Q}}}\cdot\overline{\overline{\mathbf{H}}}\cdot\overline{\overline{\mathbf{Q}}}^{T} \tag{2.4.8}$$

The Cauchy stress tensor $\overline{\overline{\sigma}}$ and the 2nd Piola-Kirchhoff stress tensor $\overline{\overline{\mathbf{S}}}$ are frame-indifferent. Their usual rates $\frac{d\overline{\overline{\sigma}}}{dt}$ and $\frac{d\overline{\overline{\mathbf{S}}}}{dt}$ are, however, frame-

dependent. In a differential type of viscoelastic constitutive model of polymer, frame-independent material rate of stress tensor must be involved according to the objectivity of physical laws. Various frame-independent material rates of stress can be constructed. In Lagrangian description, $\frac{d\overline{\overline{\sigma}}}{dt}$ need not be written as $\frac{D\overline{\overline{\sigma}}}{Dt}$, as done in fluid mechanics with Eulerian description.

The corotational, or Jaumann material rate refers to a frame which moves and rotates with the material, but does not deform with the material. It is a material rate and given by

$$\overset{0}{\overline{\overline{\sigma}}} = \frac{d\overline{\overline{\sigma}}}{dt} + \overline{\overline{W}}\cdot\overline{\overline{\sigma}} - \overline{\overline{\sigma}}\cdot\overline{\overline{W}} \tag{2.4.9}$$

If material rate is taken in a frame which moves, rotates and deforms with the material, it is called convected material rate. The contravariant convected rate (upper-convected rate, or Oldroyd rate) is

$$\overset{\nabla}{\overline{\overline{\sigma}}} = \frac{d\overline{\overline{\sigma}}}{dt} - \overline{\overline{L}}^{T}\cdot\overline{\overline{\sigma}} - \overline{\overline{\sigma}}\cdot\overline{\overline{L}} \tag{2.4.10}$$

while the covariant convected rate (lower-convected rate) is

$$\overset{\Delta}{\overline{\overline{\sigma}}} = \frac{d\overline{\overline{\sigma}}}{dt} + \overline{\overline{L}}\cdot\overline{\overline{\sigma}} + \overline{\overline{\sigma}}\cdot\overline{\overline{L}}^{T} \tag{2.4.11}$$

Superposition of two frame-independent quantities is another frame-independent quantity, such as Gordon-Schowalter material rate, which is

$$\overset{\square}{\overline{\overline{\sigma}}} = \frac{d\overline{\overline{\sigma}}}{dt} + \overline{\overline{W}}\cdot\overline{\overline{\sigma}} - \overline{\overline{\sigma}}\cdot\overline{\overline{W}} - a(\overline{\overline{D}}\cdot\overline{\overline{\sigma}} + \overline{\overline{\sigma}}\cdot\overline{\overline{D}}) \tag{2.4.12}$$

where a =1, a =0, and a = -1 give the rates in (2.4.9)-(2.4.11), respectively. There are other frame-independent material rates available (Larson, 1988).

It is now ready to construct nonlinear constitutive equations of polymers in large deformation.

2.5 Constitutive Material Equations of Polymer Solid and Fluid

Constitutive equations are often derived from constitutive models. A constitutive model is a set of assumptions and idealizations about molecular or structural forces and motions that produce stress. Different constitutive models might mathematically yield the same equation.

Any constitutive equation of continuum medium is an expression containing stress history $\overline{\overline{\sigma}}(X, t')$, $(-\infty < t' < t)$, strain history $\overline{\overline{\varepsilon}}(X, t')$, and temperature history $T(X, t')$, as well as some material constants, or even a material constant tensor. t' is previous time, and t, the current time.

There are various constitutive equations available for polymers (Bird et al. 1987, and Larson, 1988). A proper choice of constitutive equation for numerical simulation depends on what state of material to be described (in molten, or concentrated, or dilute solution, or solid states), on what kind of deformation (flow) to be described (shear, extension, steady, or transient flows), and on the numerical scheme. Only those related to the problems in this project are briefly discussed.

2.5.1 Hyperelastic Constitutive Equations of Polymer Solid

During processing, polymers usually behave viscoelastically. However, in thermoforming it has been found that hyperelastic models without involving natural time explicitly give reasonable approximations as pointed out by Treloar (1976), Schmidt and Carley (1975), and Song et al. (1991 (a)). The success of these models is due to the fact that the process is very rapid so that there is little time allowed for viscous dissipation.

In hyperelastic model, there exists a strain energy function $W(\gamma_{ij})$

with respect to unit volume of the undeformed body.

For an isotropic, compressible material,

$$W = W(\gamma_{ij}) = W(I_1, I_2, I_3) \tag{2.5.1}$$

The Cauchy stress tensor is given by

$$\begin{aligned} {}^1\bar{\bar{\sigma}} &= \frac{\partial}{\partial\, {}^1\bar{\bar{\varepsilon}}} \left(\frac{{}^1\rho}{{}^0\rho} W \right) \\ &= \frac{2}{\sqrt{I_3}} \frac{\partial W}{\partial I_1} \bar{\bar{B}} - \frac{2}{\sqrt{I_3}} \frac{\partial W}{\partial I_2} (I_3 \bar{\bar{B}}^{-1} - I_2 \bar{\bar{I}}) + 2\sqrt{I_3} \frac{\partial W}{\partial I_3} \bar{\bar{I}} \end{aligned} \tag{2.5.2}$$

where ${}^0\rho$ and ${}^1\rho$ are densities of the body at configuration C_0 and C_1.

In total Lagrangian description, the 2nd Piola-Kirchhoff stress $\bar{\bar{S}}$ is used, instead of Cauchy stress.

$$\begin{aligned} {}^1_0\bar{\bar{S}} &= \frac{\partial W}{\partial\, {}^1_0\bar{\bar{E}}} \\ &= 2 \frac{\partial W}{\partial I_1} \bar{\bar{I}} + 2 \frac{\partial W}{\partial I_2} (I_1 \bar{\bar{I}} - \bar{\bar{C}}) + h\, \bar{\bar{C}}^{-1} \end{aligned} \tag{2.5.3}$$

where

$$h = 2 I_3 \frac{\partial W}{\partial I_3} \tag{2.5.4}$$

The component form of $\bar{\bar{S}}$ is

$$\bar{\bar{S}} = S^{ij} g_i g_j = \frac{1}{2} \left(\frac{\partial W}{\partial \gamma_{ij}} + \frac{\partial W}{\partial \gamma_{ij}} \right) g_i g_j \tag{2.5.5}$$

For an incompressible material, $I_3 = 1$, $W(\gamma_{ij}) = W(I_1, I_2)$

$$\bar{\bar{\sigma}} = - p \bar{\bar{I}} + \bar{\bar{\tau}} \tag{2.5.6}$$

where the extra-stress tensor $\bar{\bar{\tau}}$ is

$$\bar{\bar{\tau}} = 2 \frac{\partial W}{\partial I_1} \bar{\bar{B}} - 2 \frac{\partial W}{\partial I_2} \bar{\bar{B}}^{-1} \tag{2.5.7}$$

and p is hydrostatic-pressure.

$$\begin{aligned} \bar{\bar{S}} &= 2\frac{\partial W}{\partial I_1}\bar{\bar{I}} + 2\frac{\partial W}{\partial I_2}(I_1\bar{\bar{I}} - \bar{\bar{C}}) - p\,\bar{\bar{C}}^{-1} \\ &= \frac{\partial W}{\partial \bar{\bar{E}}} - p\,\bar{\bar{C}}^{-1} \end{aligned} \tag{2.5.8}$$

i.e., $\bar{\bar{S}}$, or $\bar{\bar{\sigma}}$, is determined by strain energy, or deformation, only up to an additive isotropic term $p\,\bar{\bar{C}}^{-1}$.

The contravariant components of $\bar{\bar{S}}$ are

$$S^{ij} = \Phi\, g^{ij} + \Psi\, H^{ij} - p\, G^{ij} \tag{2.5.9}$$

where

$$\begin{cases} \Phi = 2\dfrac{\partial W}{\partial I_1}, \ \Psi = 2\dfrac{\partial W}{\partial I_2} \\ H^{ij} = I_1 g^{ij} - g^{ir}g^{js}G_{rs} \end{cases} \tag{2.5.10}$$

With the unit vector bases $\mathbf{a}_i$ and $\mathbf{a}^i$, eq.s (2.5.5), (2.5.9) and (2.5.10) still hold except that $\mathbf{g}_i$, g^{ij}, and G_{ij} should be replaced by $\mathbf{a}_i$, a^{ij} and A_{ij}. These unit vector bases are adopted in this project.

In simple deformation cases, or in principal directions of deformation, the different stress measures are

$$\sigma_{ii} = \lambda_i \frac{\partial W}{\partial \lambda_i} - p, \ S^{ii} = \frac{1}{\lambda_i^2}\sigma_{ii}, \text{ and } T^{ii} = \frac{1}{\lambda_i}\sigma_{ii} \tag{2.5.11}$$

The forms of these stresses in specific simple deformation can be derived easily.

2.5.2 Viscoelastic Constitutive Equations of Polymer Fluid

In thermoforming and blow molding, polymer deformation is extension-dominated. Processes are rapid (transient), and the major viscoelastic effect maybe concerned is stress relaxation. In compression forming, polymer is in a molten state. The process is not so rapid, and steady-state flow can be

reached. Viscoelastic behavior is inherent to the process. Both shear and extension are presented, and permanent deformation might exist.

Viscoelastic constitutive equations for polymer melts (fluid state polymer) are discussed in this chapter. Equations for polymer solids are addressed in a separate report (Song, 1992).

A fluid is called viscoelastic if capable of storing elastic energy, or stresses contained persist after deformation has ceased (stress relaxation). The elastic recovery of viscoelastic fluid is, however, imperfect, i.e. the material "remembers" more about its most recently previous shape than those at remote past. This is called "fading memory" (Coleman and Noll, 1961).

For example, Rivlin and Sawyers' equation

$$\bar{\bar{\tau}} = \int_{-\infty}^{t} [\ \phi_1(I_1, I_2, t-t')\ \bar{\bar{B}} - \phi_2(I_1, I_2, t-t')\ \bar{\bar{B}}^{-1}\ ]\ dt' \qquad (2.5.13)$$

is a general integral type constitutive equation to within an isotropic term. Here ϕ_1 and ϕ_2 are functions of I_1 and I_2, the invariants of $\bar{\bar{B}}$, and time $t-t'$. ϕ_1 and ϕ_2 represent the time effect (memory effect) and strain history effect. The left Cauchy-Green tensor $\bar{\bar{B}}$ here is written as $\bar{\bar{C}}^{-1}$ in Larson's book (1988).

If one requires an elastic limit at high strain rate, then it can be shown that

$$\phi_1 = 2\ \frac{\partial U}{\partial I_1},\ \text{and}\ \phi_2 = 2\ \frac{\partial U}{\partial I_2} \qquad (2.5.14)$$

where U is a potential function. Taking eq.(2.5.14) into eq.(2.5.13), we have

$$\bar{\bar{\tau}} = \int_{-\infty}^{t} [\ 2\ \frac{\partial U}{\partial I_1}\ \bar{\bar{B}} - 2\ \frac{\partial U}{\partial I_2}\ \bar{\bar{B}}^{-1}\ ]dt' \qquad (2.5.15)$$

which is the K-BKZ equation. The free energy for the viscoelastic fluid is

$$W = \int_{-\infty}^{t} U(I_1, I_2, t-t')\ dt' \qquad (2.5.16)$$

K-BKZ equation is derived from rubber elasticity (hyperelasticity) theory (comparing eq.(2.5.15) to eq.(2.5.7)), and is generally useful to study different kinds of flows of polymer fluids, because it permits a great variety of behavior depending on the choice of the kernel $U(I_1, I_2, t-t')$.

If ϕ_2 is set to zero and $\phi_1 = h(I_1, I_2)\ m(t-t')$, eq.(2.5.13) is the Wagner I equation

$$\bar{\bar{\tau}} = \int_{-\infty}^{t} h(I_1, I_2)\ m(t-t')\ \bar{\bar{B}}\ dt' \tag{2.5.17}$$

where h is a damping function, $m(t-t')$, a memory function, which might consist of a spectrum of relaxation processes. Wagner equation is widely accepted.

The following example shows how viscoelastic behavior and its two extreme cases (elastic and viscous behavior) are captured by these constitutive equations.

With Wagner equation, if $h(I_1, I_2) = 1$, the eq.(2.5.17) becomes Lodge equation

$$\bar{\bar{\tau}} = \int_{-\infty}^{t} m(t-t')\ \bar{\bar{B}}(t, t')\ dt' \tag{2.5.18}$$

Considering simple shear deformation, ${}^1x = {}^0X + \gamma\ {}^0X_2\ e_1$, and

$$\bar{\bar{B}} = \begin{bmatrix} 1+\gamma^2 & \gamma & 0 \\ \gamma & 1 & 0 \\ 0 & 0 & 1 \end{bmatrix} \tag{2.5.19}$$

where $B_{12} = \gamma(t, t')$ is the accumulated shear strain between times t and t',

$$\gamma(t, t') = \int_{t'}^{t} \dot{\gamma}(s)\ ds \tag{2.5.20}$$

Only a single relaxation process with λ as the relaxation time is considered. $m(t-t')$ is taken as $G\ \frac{1}{\lambda}\ e^{(t'-t)/\lambda}$ to take into account fading memory. If the deformation process is very rapid, all strain is imposed just before the present time t, then $\gamma(t, t') = \gamma(t)$. Take this $\gamma(t, t')$ and eq.(2.5.19) into

eq.(2.5.18), we obtain the elastic limit, with $\tau_{12}= G\gamma$. If deformation is very slow and steady state is reached, the accumulated strain is $\dot{\gamma}\cdot(t-t')$. Substitute it into eq.(2.5.18), we have Newtonian viscous fluid limit, i.e. $\tau_{12}= G\lambda\ \dot{\gamma}$. When a deformation process is not as fast and not as slow, the shear stress will depend on the present shear strain γ and the shear rate $\dot{\gamma}$. Deformation is viscoelastic.

Integral type constitutive equation has a drawback in the implementation of numerical analysis, that is, at each time step, all contributions to stress from previous time steps have to be accumulated, which is a time-consuming process. Two alternative ways to overcome this problem are firstly, utilizing differential, or rate type constitutive equations. Only strain and stress at each time step and their material rates are incorporated in simulation. But implementation of material rate in a finite element program can also be time-consuming. Another alternative is to apply a correspondence principle to take into account viscoelastic effect. In thermoforming, blow molding, and compression forming, application of the correspondence principle seems to be a simple way of obtaining a solution if stress relaxation is the only viscoelastic effect of concern. Correspondence principles are discussed in detail in Morman (1988).

In most commercially available numerical programs, simple differential, or rate type constitutive equations, are often used to simulate complex polymer flows. The simplest equation is generalized Newtonian fluid equation

$$\bar{\bar{\tau}} = 2\ \eta(II_d)\ \bar{\bar{D}} \qquad (2.5.21)$$

which can be used in the momentum balance equation to compute pressure drop and viscous dissipation. II_d is the second invariant of $\bar{\bar{D}}$. Popular forms for

$\eta(II_d)$ are power-law model,

$$\eta(II_d) = m\ II_d^{(n-1)/2} \tag{2.5.22}$$

and Carreau model

$$\frac{\eta - \eta_\infty}{\eta_0 - \eta_\infty} = [\ 1 + \lambda^2\ II_d]^{(n-1)/2} \tag{2.5.23}$$

Both models can predict shear viscosity well, but not extensional viscosity. A phenomenological viscosity model is proposed (Song, 1993 (a) and (b)), which depends on both the second and third invariants. It can not only predict shear viscosity well, but also extensional viscosity, and is successfully used in numerical analysis to predict vortex enhancement in entry flow of polymer melts.

A more complicated constitutive equation for numerical simulation is the Upper-Convected Maxwell equation,

$$\lambda \overset{\nabla}{\overline{\overline{\tau}}} + \overline{\overline{\tau}} = 2\ \eta\ \overline{\overline{D}} \tag{2.5.24}$$

where λ is relaxation time, $\overset{\nabla}{\overline{\overline{\tau}}}$ is the upper-convected rate of $\overline{\overline{\tau}}$ (2.4.10). If both λ and η are functions of II_d, it is known as White-Metzner equation. This constitutive equation can explain some viscoelastic behavior of polymer melts and solids as well.

Numerical modeling of complex flows with popular viscoelastic constitutive equations can predict the behavior of real fluids, depending on the value of the Weissenberg number, a measure of viscoelasticity (Debbaut et al. 1988).

CHAPTER 3
FINITE ELEMENT ANALYSIS OF POLYMER FORMING PROCESSES

3.1 Nonlinear Finite Element Formulation

In current configuration C_1, equilibrium equation and boundary conditions are

$$ {}^1\rho \frac{\partial {}^1\mathbf{v}}{\partial t} = \frac{\partial}{\partial {}^1\mathbf{x}} \cdot {}^1\overline{\overline{\sigma}} + {}^1\mathbf{b} \quad \text{in } {}^1V \tag{3.1.1} $$

$$ {}^1\mathbf{u} = \mathbf{u}^* = u^{*i}\,\mathbf{g}_i = u^*_i\,\mathbf{g}^i \quad \text{on } A_u \tag{3.1.2} $$

$$ {}^1\overline{\overline{\sigma}} \cdot {}^1\mathbf{n} = \mathbf{T}^* = T^{*i}\,\mathbf{g}_i = T^*_i\,\mathbf{g}^i \quad \text{on } A_\sigma \tag{3.1.3} $$

where ${}^1\mathbf{b}$, $\mathbf{u}^*$, and $\mathbf{T}^*$ are body force, specified displacement and surface traction, respectively.

The principle of virtual work is

$$ \int_{{}^1V} {}^1\rho \frac{d\,{}^1\mathbf{v}}{dt} \cdot \delta {}^1\mathbf{v}\; d\,{}^1V + \int_{{}^1V} {}^1\overline{\overline{\sigma}} : \delta {}^1\overline{\overline{D}}\; d\,{}^1V = \int_{{}^1A_\sigma} {}^1\mathbf{T}^* \cdot \delta {}^1\mathbf{v}\; d\,{}^1A + \int_{{}^1V} {}^1\mathbf{b} \cdot \delta {}^1\mathbf{v}\; d\,{}^1V \tag{3.1.4} $$

where $\delta {}^1\mathbf{v}$ $(=\delta {}^1\dot{\mathbf{u}})$ is virtual velocity satisfying the prescribed geometrical boundary conditions (3.1.2), virtual rate of deformation $\delta {}^1\overline{\overline{D}}$ is

$$ \delta {}^1\overline{\overline{D}} = \frac{1}{2}\,\delta\left[\frac{\partial {}^1\mathbf{v}}{\partial {}^1\mathbf{x}} + \left(\frac{\partial {}^1\mathbf{v}}{\partial {}^1\mathbf{x}} \right)^T \right] \tag{3.1.5} $$

When inertia and body force terms are ignored, the virtual work principle states

$$ \int_{{}^1V} {}^1\overline{\overline{\sigma}} : \delta {}^1\overline{\overline{D}}\; d\,{}^1V = \int_{{}^1A_\sigma} {}^1\mathbf{T}^* \cdot \delta {}^1\mathbf{v}\; d\,{}^1A \tag{3.1.6} $$

With the total Lagrangian description, the integration domain of the left-hand side of eq.(3.1.6) is converted from ${}^1V$ to ${}^0V$, and the equation becomes

$$\int_{{}^0V} {}^1_0\bar{\bar{S}} : \delta {}^1_0\dot{\bar{\bar{E}}}\, d^0V = \int_{{}^1A_\sigma} {}^1\mathbf{T}^* \cdot \delta {}^1\mathbf{v}\, d^1A \tag{3.1.7}$$

where continuity condition ${}^0\rho\ d^0V = {}^1\rho\ d^1V$ is used, and

$${}^1_0\bar{\bar{S}} : \delta {}^1_0\dot{\bar{\bar{E}}} = S^{ij}\ \delta\dot{\gamma}_{ij} \tag{3.1.8}$$

S^{ij} are the contravariant components of the 2nd order Piola-Kirchhoff stress tensor and $\dot{\gamma}_{ij}$ are Lagrange strain rates. Eq.(3.1.6) can be used to establish Eulerian type finite element formulation, while eq.(3.1.7) is used for Lagrangian type finite element formulation.

The rate of total virtual strain energy is

$$\delta\ \dot{U} = \int_{{}^0V} \delta\dot{W}\ d^0V = \int_{{}^0V} \frac{\partial\ W}{\partial\ \gamma_{ij}}\ \delta\dot{\gamma}_{ij}\ d^0V = \int_{{}^0V} S^{ij}\ \delta\dot{\gamma}_{ij} d^0V \tag{3.1.9}$$

Here, hyperelastic model is assumed, W is strain energy density, and

$$S^{ij} = \frac{\partial\ W}{\partial\ \gamma_{ij}} \tag{3.1.10}$$

Rate of virtual work of external forces is

$$\delta\ \dot{W}_{ext} = \int_{{}^1A_\sigma} {}^1\mathbf{T}^* \cdot\ \delta\dot{\mathbf{u}}\ d^1A \tag{3.1.11}$$

so another form of eq.(3.1.7) is $\delta\ \dot{U} = \delta\ \dot{W}_{ext}$. Physical interpretation of the principle of virtual work is that the rate of virtual work done by internal forces is equal to virtual work done by external forces in arbitrary virtual velocity satisfying the prescribed geometrical boundary conditions. Further discussions on virtual work principles are found in Washizu (1982).

In finite element analysis, the set of partial differential eq.(3.1.1), together with the boundary conditions (3.1.2) and (3.1.3) for a

continuum, is approximated by a discrete model. The body is represented as a collection of a finite number of elements connected together at prescribed nodes. Through virtual work principle, or Galerkin's method (Oden, 1972), eq.(3.1.1) is approximately satisfied in an averaging sense over each element. The unknowns are displacements (strains) and/or stresses at elemental nodes. Inside each element, displacement (strain) and/or stress are approximated by linear, quadratic, or other simple low-order functions, which are called shape functions. The continuum with infinite degrees of freedom is thus represented by a discrete model which has finite degrees of freedom. The partial differential equations are converted into a system of algebraic, or ordinary differential equations, which are generally nonlinear and can be solved numerically. If certain completeness conditions are satisfied, then as the number of finite elements is increased and their dimensions are decreased, behavior of the discrete system converges to that of the continuous system. The finite element method is applicable to analysis of finite deformation of materially nonlinear, anisotropic, nonhomogeneous body with arbitrary geometrical shape.

The deformed body is discretized into finite elements first. In this project, six-node isoparametric triangular elements are used. That is, for a single element, both coordinates and displacements of any point in the element are expressed in terms of the same shape functions,

$$\begin{cases} X_\nu = \Psi_M X_{\nu M} \\ u_\nu = \Psi_M u_{\nu M} \end{cases} \quad (M = 1, 2,...,N, \quad \nu = 1, 2) \tag{3.1.12}$$

where Ψ_Ms are the corresponding element shape functions, N is the node number of each element, $u_{\nu M}$ is nodal displacement component, and u_1 (u_r) and u_2(u_z) represent the displacement components in r and z directions. Problems dealt

with in this project are axisymmetric.

Based on eq.(3.1.7), equilibrium equations in finite element form can be written as

$$f_M^{\nu} = \int_{{}^0V} S^{ij} \frac{\partial \gamma_{ij}}{\partial u_{\nu M}} d^0V - p_M^{\nu} = 0 \quad (M = 1, 2,...,N, \quad \nu = 1, 2) \tag{3.1.13}$$

where

$$p_M^{\nu} = \int_{{}^1A_\sigma} {}^1T_{\nu}^{*} \Psi_M d^1A \tag{3.1.14}$$

is nodal loading vector, which is a function of unknown displacement vector, since ${}^1A_\sigma$ and ${}^1\mathbf{T}^*$ may change with displacement field.

In matrix form, eq.(3.1.13) changes into

$$\{\mathbf{f}\} = [\mathbf{K(u)}] \cdot \{\mathbf{u}\} - \{\mathbf{p(u)}\} = \{\mathbf{0}\} \tag{3.1.15}$$

where [**K**] is the stiffness matrix given by,

$$\mathbf{K}_{ij} u_j = \int_{{}^0V} S^{kl} \frac{\partial \gamma_{kl}}{\partial u_i} d^0V \tag{3.1.16}$$

Integration is taken over the initial volume ${}^0V$. The nonlinear equation (3.1.15) can not be solved directly. Instead, an incremental form is used to obtain an increment of the displacement field, then Newton-Raphson iteration method is employed to achieve equilibrium.

3.2 Incremental Loading Method with Newton-Raphson Iteration

Suppose the motion (displacement field and loading) at time t in configuration C_1 is known, then at time $t+\Delta t$, configuration C_2, the body moves from C_1 to C_2, eq.s (3.1.13) and (3.1.14) hold, but superscript 1 is replaced by 2. If there is a loading parameter, q, such as the external uniform pressure loading in a thermoforming process, then

$$^{2}\mathbf{u} = {}^{1}\mathbf{u} + \Delta^{1}\mathbf{u}, \text{ and } {}^{2}q = {}^{1}q + \Delta^{1}q \tag{3.2.1}$$

Expanding eq.(3.1.15) of C_2 as a power series of $\Delta^1\mathbf{u}$ and $\Delta^1 q$, and keeping linear terms, we obtain a linearized incremental form of the equilibrium equations:

$$\Delta f_M^V = \frac{\partial f_M^V}{\partial u_{\lambda_N}} \Delta u_{\lambda_N} + \frac{\partial f_M^V}{\partial q} \Delta q = 0 \tag{3.2.2}$$

where it is assumed that all the derivatives are taken at C_1, i.e. they are functions of known $^{1}\mathbf{u}$ and ^{1}q. Therefore, the increments $\Delta^1\mathbf{u}$ can be solved for a given Δq from the linear eq.(3.2.2) and thus an approximation of state C_2 is obtained.

In matrix form, we have

$$[\mathbf{K}_{INC}]\cdot\{\Delta\mathbf{u}\} = \{\Delta\mathbf{p}\} \tag{3.2.3}$$

$$(\mathrm{K}_{INC})_{ij} = \mathrm{K}_{ij} + \left[\frac{\partial\ \mathrm{K}_{ik}}{\partial\ u_j}\right]\cdot u_k - \frac{\partial\ p_i}{\partial\ u_j} \tag{3.2.4}$$

and

$$\Delta p_i = \Delta q \frac{\partial p_M^V}{\partial q} \tag{3.2.5}$$

where $[\mathbf{K}_{INC}]$ is the incremental stiffness.

After each incremental loading step, Newton-Raphson iterations may be performed to correct predicted displacement vector until some tolerance criterion is satisfied

$$^{2}\mathbf{u}^{(i+1)} = {}^{2}\mathbf{u}^{(i)} + \Delta^{2}\mathbf{u}^{(i+1)} \qquad i = 1, 2,... \tag{3.2.6}$$

where the first guess of $^{2}\mathbf{u}$ is given by eq.(3.2.3).

For the $(i+1)$ th iteration, we have

$$\frac{\partial f_M^{\nu}}{\partial u_{\lambda_N}} \Delta u_{\lambda_N} = -f_M^{\nu} \tag{3.2.7}$$

or

$$[\mathbf{K}_{N\text{-}R}] \cdot \{\Delta \mathbf{u}\} = -\{\mathbf{f}\} \tag{3.2.8}$$

where the f_M^{ν} or $\{\mathbf{f}\}$ is the residual vector given by (3.1.15), and all the derivatives and residuals are taken at the (i) th iteration at C_2.

3.3 Deformation-dependent Loading Vector and "Load-Correction" Stiffness

In thermoforming, it is the applied pressure that drives the polymer sheet to deform. This uniformly distributed pressure loading is normal to the sheet, that is, the direction of pressure on any point of the sheet changes with deformation.

Suppose there is no other loading except the pressure. Then, we have

$${}^1\mathbf{T}^* = -\, q\, {}^1\mathbf{n} \tag{3.3.1}$$

where q is the magnitude of uniformly distributed pressure, and ${}^1\mathbf{n}$ is the outer normal direction of element surface which is subjected to pressure, as shown in Figure 3.1.

In the current deformed state, an infinitesimal area of a ring element of axisymmetric problem is

$$d^1A = 2\pi(R + {}^1u_r)\, d\xi \tag{3.3.2}$$

where R is the convected material coordinate of point B, u_r is its radial displacement, and ξ is an embedded coordinate along the meridional direction. The positive direction of ξ is where the deformed body is always on its left-hand side.

Components of loading vector p are

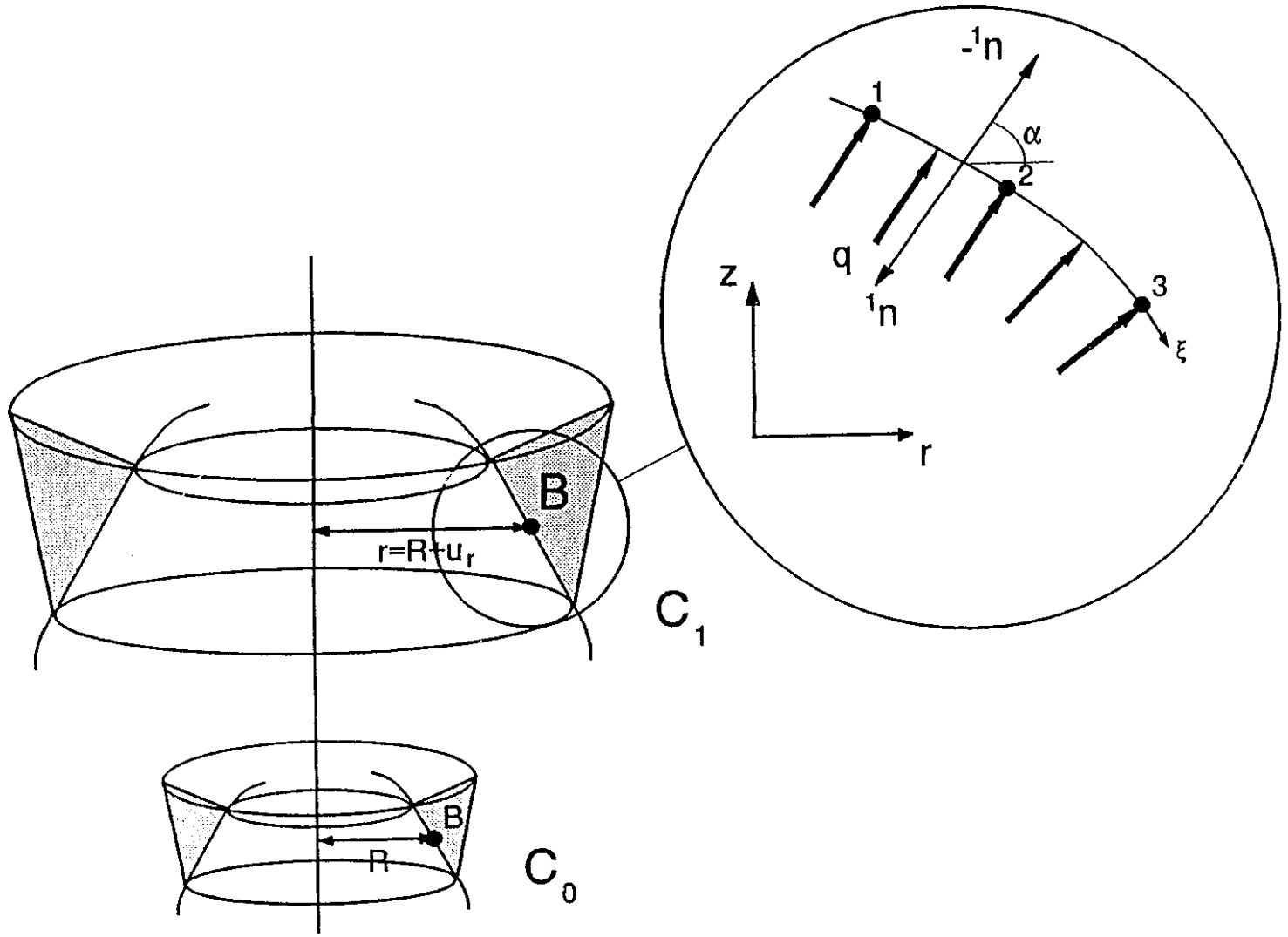

Figure 3.1 Deformation-dependent loading.

$$p_M^{\nu} = \int_{{}^1A_\sigma} -q\, n_\nu\, \Psi_M \mathrm{d}^1A = -2\pi \int_{\xi} q\,(R + u_r)\, n_\nu\, \Psi_M\, \mathrm{d}\xi \tag{3.3.3}$$

The second integration in eq. (3.3.3) is a material integration.

From Figure 3.1, we have

$$-{}^1\mathbf{n} = \begin{Bmatrix} \cos\alpha \\ \sin\alpha \end{Bmatrix} = \begin{Bmatrix} -\mathrm{d}z/\mathrm{d}\xi \\ \mathrm{d}r/\mathrm{d}\xi \end{Bmatrix} \tag{3.3.4}$$

Since elements used are isoparametric, there are

$$\begin{cases} R = \Psi_M(\xi) R_M \\ Z = \Psi_M(\xi) Z_M \end{cases}, \quad \begin{cases} u_r = \Psi_M u_{rM} \\ u_Z = \Psi_M Z_{ZM} \end{cases}, \text{ and } \begin{cases} r = \Psi_M(R_M + u_{rM}) \\ z = \Psi_M(Z_M + u_{ZM}) \end{cases} \tag{3.3.5}$$

Substitute eq.s (3.3.4) and (3.3.5) into (3.3.3), we have

$$\begin{cases} p_M^1 = -2\pi q \int_0^1 (R + u_r)\, \Psi_M\, \Psi_{K,\xi} (Z_K + u_{ZK})\, \mathrm{d}\xi \\ p_M^2 = 2\pi q \int_0^1 (R + u_r)\, \Psi_M\, \Psi_{K,\xi} (R_K + u_{rK})\, \mathrm{d}\xi \end{cases} \tag{3.3.6}$$

which indicates this loading vector is displacement-dependent. Therefore, in the incremental loading process, we have

$$\begin{cases} p^1_{M,u_{rN}} = -2\pi q \int_0^1 \Psi_M\, \Psi_N\, \Psi_{K,\xi} (Z_K + u_{ZK})\, \mathrm{d}\xi \\ p^1_{M,u_{ZN}} = -2\pi q \int_0^1 (R + u_r)\, \Psi_M\, \Psi_{N,\xi}\, \mathrm{d}\xi \\ p^2_{M,u_{rN}} = 2\pi q \int_0^1 [\Psi_M\, \Psi_N\, \Psi_{K,\xi} (R_K + u_{rK}) + (R + u_r) \Psi_M\, \Psi_{N,\xi}]\, \mathrm{d}\xi \\ p^2_{M,u_{ZN}} = 0 \end{cases} \tag{3.3.7}$$

Eq.(3.3.7) gives stiffness matrix contributed from loading, which is the third term on the right-hand side of eq.(3.2.4) and called "load-correction" stiffness matrix. It is unsymmetrical and gives rise to additional numerical difficulty. But including the load stiffness can greatly reduce the number of iterations required for convergence (Argyris, 1981). Inclusion of the load

stiffness is sometimes essential in obtaining the solution to a problem.

Since six-node isoparametric elements are used in the finite element program, shape functions on the edge of an element are

$$\begin{cases} \Psi_1 = 1 - 3\xi + 2\xi^2 \\ \Psi_2 = 4\xi - 4\xi^2 \qquad \xi: 0 \to 1 \\ \Psi_3 = 2\xi^2 - \xi \end{cases} \tag{3.3.8}$$

With these shape functions, parabolically distributed pressure loading over the element can be exactly modeled.

3.4 The Penalty Method and Selective Reduced Integration

In our finite element analysis, we confine our attention to the isothermal process of homogeneous, incompressible, hyperelastic materials. The incompressibility equation (2.2.8) could be either satisfied approximately by introducing a very large penalty number $1/\varepsilon$, $(0 < \varepsilon \ll 1)$ (Zienkiewicz, 1974), or relaxed by a Lagrange multiplier h (Oden, 1972). Lagrange multiplier results in a mixed u-v-p formulation with more unknowns, even though it is equivalent to the penalty method (Zienkiewicz and Taylor, 1989). Both Lagrange multiplier and penalty methods are used in our analysis. Their equivalence has been confirmed numerically. Therefore, only the formulations with penalty method are given here.

A modified strain energy function is used in the penalty method,

$$\tilde{W} = W(I_1, I_2) + \frac{1}{\varepsilon}(I_3 - 1)^2 \tag{3.4.1}$$

$\bar{\bar{S}}$ still has the form of (2.5.3), but h in (2.5.4) should be replaced by

$$h = 2 I_3 \frac{\partial \tilde{W}}{\partial I_3} = \frac{4 I_3}{\varepsilon}(I_3 - 1) \tag{3.4.2}$$

If we denote stresses contributed from $W(I_1, I_2)$ as $\bar{S}^{ij}$, then

$$\bar{S}^{ij} = 2\frac{\partial W}{\partial I_1} g^{ij} + 2\frac{\partial W}{\partial I_2}(I_1 g^{ij} - g^{ir} g^{js} G_{rs}) \tag{3.4.3}$$

Stresses contributed from the penalty term in eq.(3.4.1) are

$$\begin{cases} \tilde{S}^{11} = \chi\ (\ 1 + 2\ \gamma_{22})\ (\ 1 + 2\ \gamma_{33}) \\ \tilde{S}^{22} = \chi\ (\ 1 + 2\ \gamma_{11})\ (\ 1 + 2\ \gamma_{33}) \\ \tilde{S}^{12} = -2\chi\ (\ 1 + 2\ \gamma_{33})\ \gamma_{12} \\ \tilde{S}^{33} = \chi\ \Psi \end{cases} \tag{3.4.4}$$

where

$$\chi = \frac{4}{\varepsilon}\ (\ I_3 - 1\ ) \tag{3.4.5}$$

Therefore,

$$S^{ij} = \bar{S}^{ij} + \tilde{S}^{ij} \tag{3.4.6}$$

The specific form of $\bar{S}^{ij}$ depends on the specific hyperelastic model chosen, which is discussed in Chapter 4. The S^{ij} given in (3.4.6) should be used in (3.1.13) and (3.2.4) to evaluate stiffness matrices.

The incremental equilibrium equation (3.2.3), or the iteration equation (3.2.8) have to be evaluated numerically before they can be solved, since the integrals involved in (3.1.13), (3.2.4), (3.3.6) and (3.3.7) can not be integrated analytically.

Following a suggestion by Engelman et al. (1982) to achieve numerical convergence, a selective reduced numerical integration technique is used in the finite element program, that is, the stiffness matrix contributed from the penalty term and that from general strain energy are integrated by using different quadrature. The penalty parameter ε used ranges from 0.02 to 10^{-7}.

Components of the incremental stiffness matrix excluded the load correction contribution are

$$\frac{\partial f_M^{\nu}}{\partial u_{\lambda N}} = \frac{\partial \bar{f}_M^{\nu}}{\partial u_{\lambda N}} + \frac{\partial \tilde{f}_M^{\nu}}{\partial u_{\lambda N}} \tag{3.4.7}$$

where

$$\frac{\partial \bar{f}_M^{\nu}}{\partial u_{\lambda N}} = 2\pi \int_e R \left(\frac{\partial \bar{S}^{ij}}{\partial u_{\lambda N}} \frac{\partial \gamma_{ij}}{\partial u_{\nu M}} + \bar{S}^{ij} \frac{\partial^2 \gamma_{ij}}{\partial u_{\nu M} \partial u_{\lambda N}} \right) dR\, dZ \qquad (3.4.8)$$

and

$$\frac{\partial \tilde{f}_M^{\nu}}{\partial u_{\lambda N}} = 2\pi \int_e R \left(\frac{\partial \tilde{S}^{ij}}{\partial u_{\lambda N}} \frac{\partial \gamma_{ij}}{\partial u_{\nu M}} + \tilde{S}^{ij} \frac{\partial^2 \gamma_{ij}}{\partial u_{\nu M} \partial u_{\lambda N}} \right) dR\, dZ \qquad (3.4.9)$$

In this project, the integrals of (3.4.8) are evaluated through the use of seven-point Gaussian quadrature. If the same quadrature rule is applied to (3.4.9), then the discretized problem would be "over constrained" or "locked". Locking is avoided if the penalty integrals are under-integrated through the use of four-point Gaussian quadrature (Carey and Oden, 1983). Surface integrals of (3.3.6) and (3.3.7) are evaluated by a three-point Gaussian quadrature. Location of integration points and their associated weights is found in Zienkiewicz and Taylor (1989).

After displacement field is obtained, stress distributions can be calculated by a proper stress calculation algorithm (Stein and Ahmad, 1977, and Babuska, 1984).

3.5 Solution Techniques and Convergence Criteria

In the incremental equilibrium equation (3.2.3) and iteration equation (3.2.8), stiffness matrix $[\mathbf{K}_{INC}]$ and $[\mathbf{K}_{N\text{-}R}]$ are unsymmetrical, a symmetrical Gaussian elimination solver, or a symmetrical frontal solver can not be used. We use an unsymmetrical frontal solver to solve these algebraic equations, which has advantages of requiring less computing time and computer RAM memory. This solution technique especially appeals to application of nonlinear finite element analysis on a personal computer.

To optimize a solving process, line search, conjugate gradient, or

other kinds of acceleration methods can be used (Oden, 1972, Wolfe, 1978, and Wong and Hafez, 1982). To pass the limit point, or bifurcation path, some special methods are used, such as the "current stiffness parameter" method (Bergan et al. 1978), arc-length method, or Riks' method (Riks, 1979, and Ramm, 1981), and the technique used by Crisfield (1981). In this project, a modified Riks' method is used, since limit point is met in the simulation of thermoforming. Numerical implementation of the modified Riks' method with unsymmetrical frontal solver is briefly discussed in the following chapter.

Various convergence criteria are used in the current finite element analysis. One of the mostly used criteria is relative error criteria:

$$\frac{\|\mathbf{u}^{(i)} - \mathbf{u}^{(i-1)}\|}{\|\mathbf{u}^{(i-1)}\|} < R \qquad (3.5.1)$$

$\mathbf{u}^{(i-1)}$, and $\mathbf{u}^{(i)}$ are the calculated unknown vectors at the (i-1) th and (i) th iterations, $\|\cdot\|$ represents certain norm of vector, and R, a prescribed tolerance. Here, Euclidean norm $\|\mathbf{x}\|_2 = (\mathbf{x}\cdot\mathbf{x})^{1/2}$, and $\|\mathbf{x}\|_\infty = \max_j (|x_j|)$, are used, and R is taken as 10^{-4}, or 10^{-8}. If the above criterion is satisfied, convergence is assumed to be reached and the next incremental step of the solving process is carried out. Another criterion used is

$$\frac{\mathbf{f}^{(i)}\cdot(\mathbf{u}^{(i)} - \mathbf{u}^{(i-1)})}{W_{ref}} < R \qquad (3.5.2)$$

where $\mathbf{f}^{(i)}$ is the current residual force given by (3.1.15), $\mathbf{f}^{(i)}\cdot(\mathbf{u}^{(i)}-\mathbf{u}^{(i-1)})$ represents residual work done by the unbalanced displacement vector, and W_{ref} is a reference work, such as work done in the previous step. Usually, criteria (3.5.1) is stricter than (3.5.2).

Through numerical analysis, it is known that Newtonian-Raphson iteration should be of quadratic convergence if the initial guess used is sufficiently close to the real solution. Here it is found that for forming

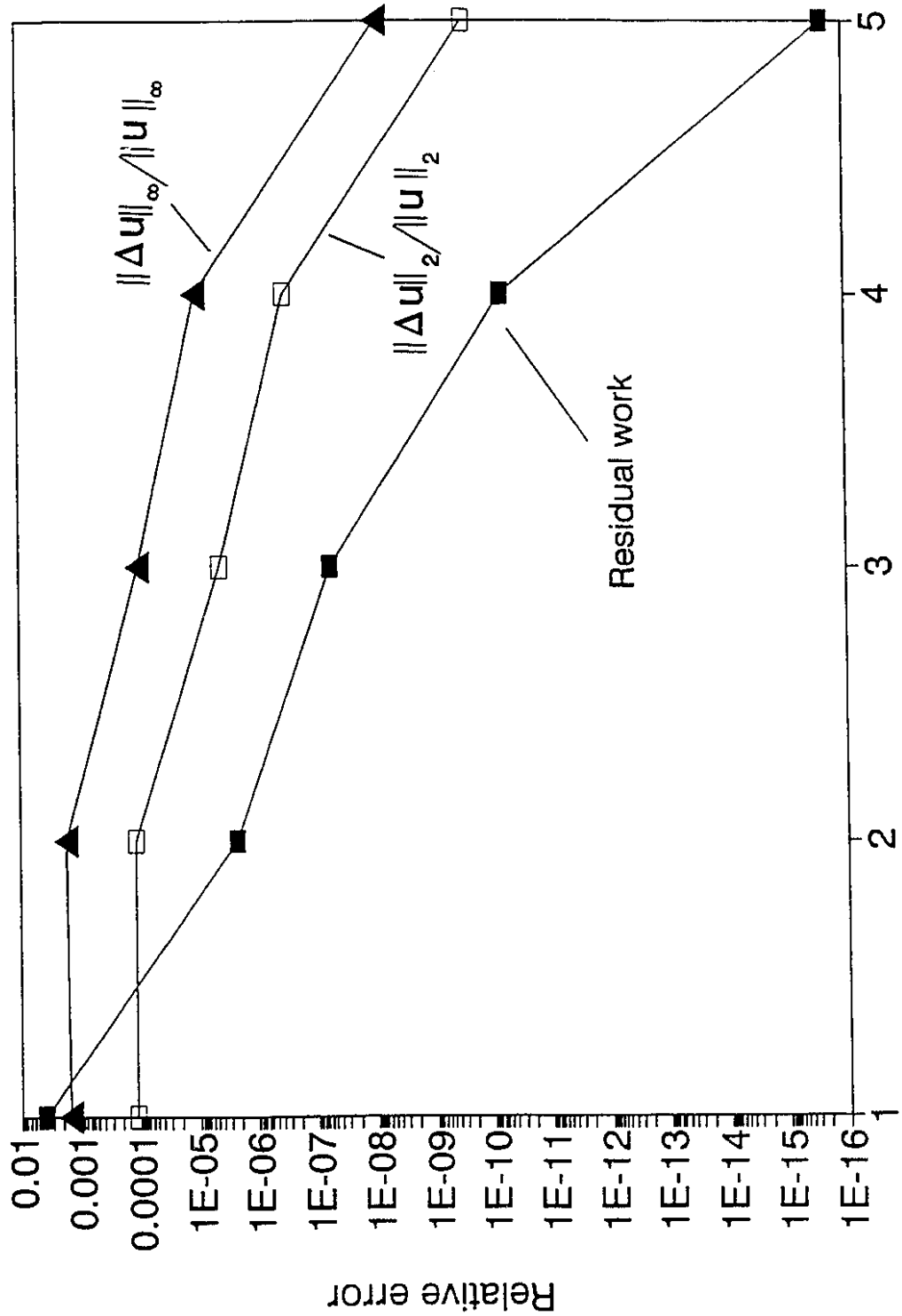

Figure 3.2 Converging results of various convergence criteria.

problems without limit point and contact, two to five iterations are enough to make eq.s (3.5.1) or (3.5.2) satisfied with R = 10^{-8}, and quadratic convergence is preserved, as shown in Figure 3.2. In order to have successful Newton-Raphson iteration the Jacobian stiffness matrices in eq.s (3.2.4) and (3.4.7) must be evaluated correctly. In this thesis, both the analytical formulation of Jacobian matrix and its numerical evaluation by finite difference method are obtained to guarantee correct evaluation of the matrix. The difference between analytical and numerical Jacobian is found to be within machine tolerance, i.e. 10^{-16}. Yet, the method to evaluate Jacobian stiffness matrix by finite difference can make a finite element program more flexible so that a user can incorporate his preferable constitutive material equation into the program without detailed knowledge about the whole finite element program.

3.6 Numerical Example

A simple problem involving the free inflation of a thick cylinder subjected to internal pressure loading is solved. Figure 3.3 shows geometry, elements used and displacement response to loading. Material parameters used are C_{01}= 60 psi (0.4137 MPa), and C_{10}= 10 psi (0.06895 MPa). Only 15 loading steps are used to reach an internal displacement of 50 cm, where internal pressure is about 1.26 MPa. Agreement with the analytical solution (Green, 1968) is excellent. Hydrostatic-pressure introduced from relaxation of incompressibility condition is also calculated according to (3.4.2) at loading of 1.26 MPa (Figure 3.4). It is noted that there is a difference between the prediction from six elements and the analytical solution, while the prediction from 12 elements compares well with the analytical solution.

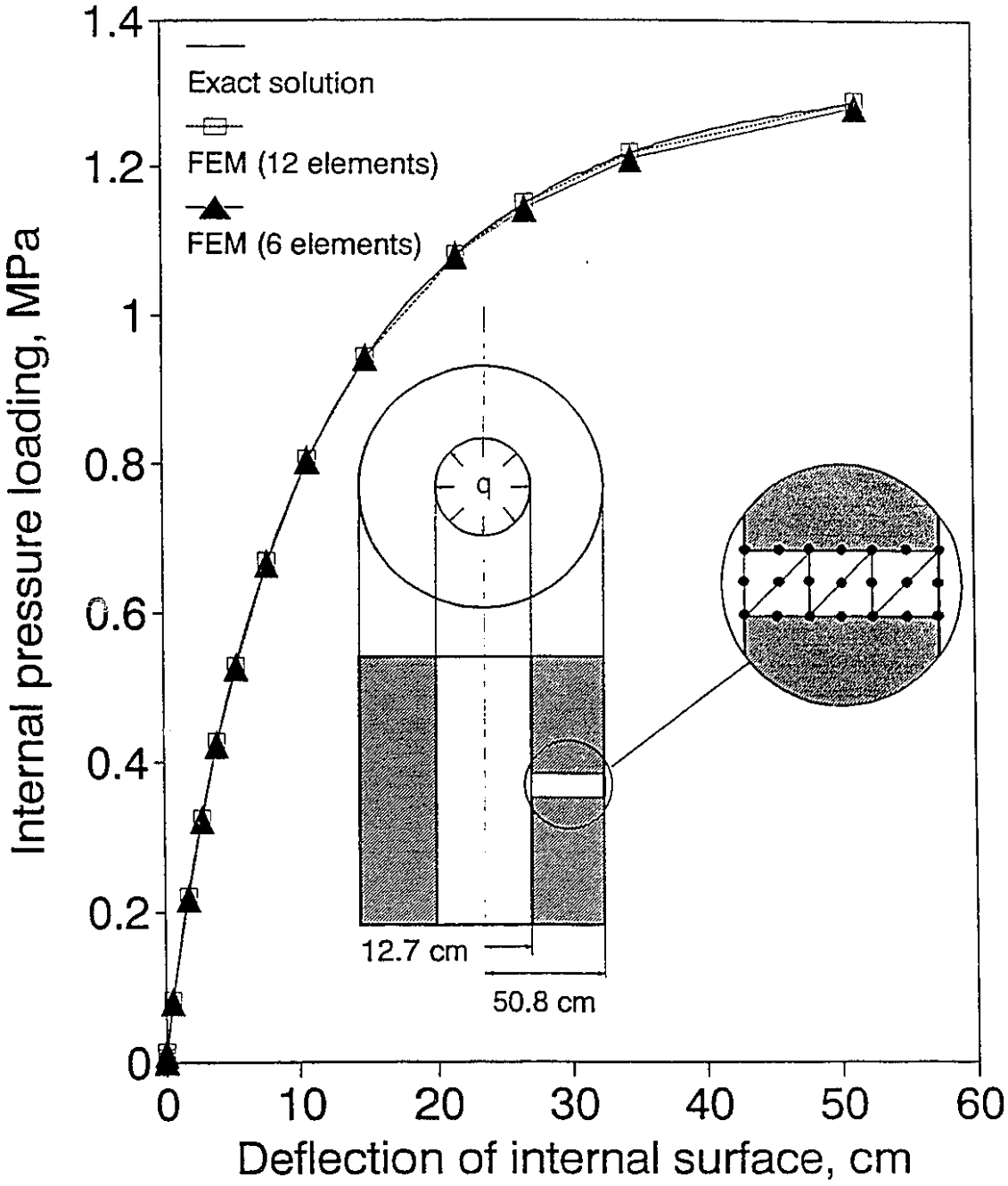

Figure 3.3 A comparison of finite element results with exact solution for inflation of a thick cylinder.

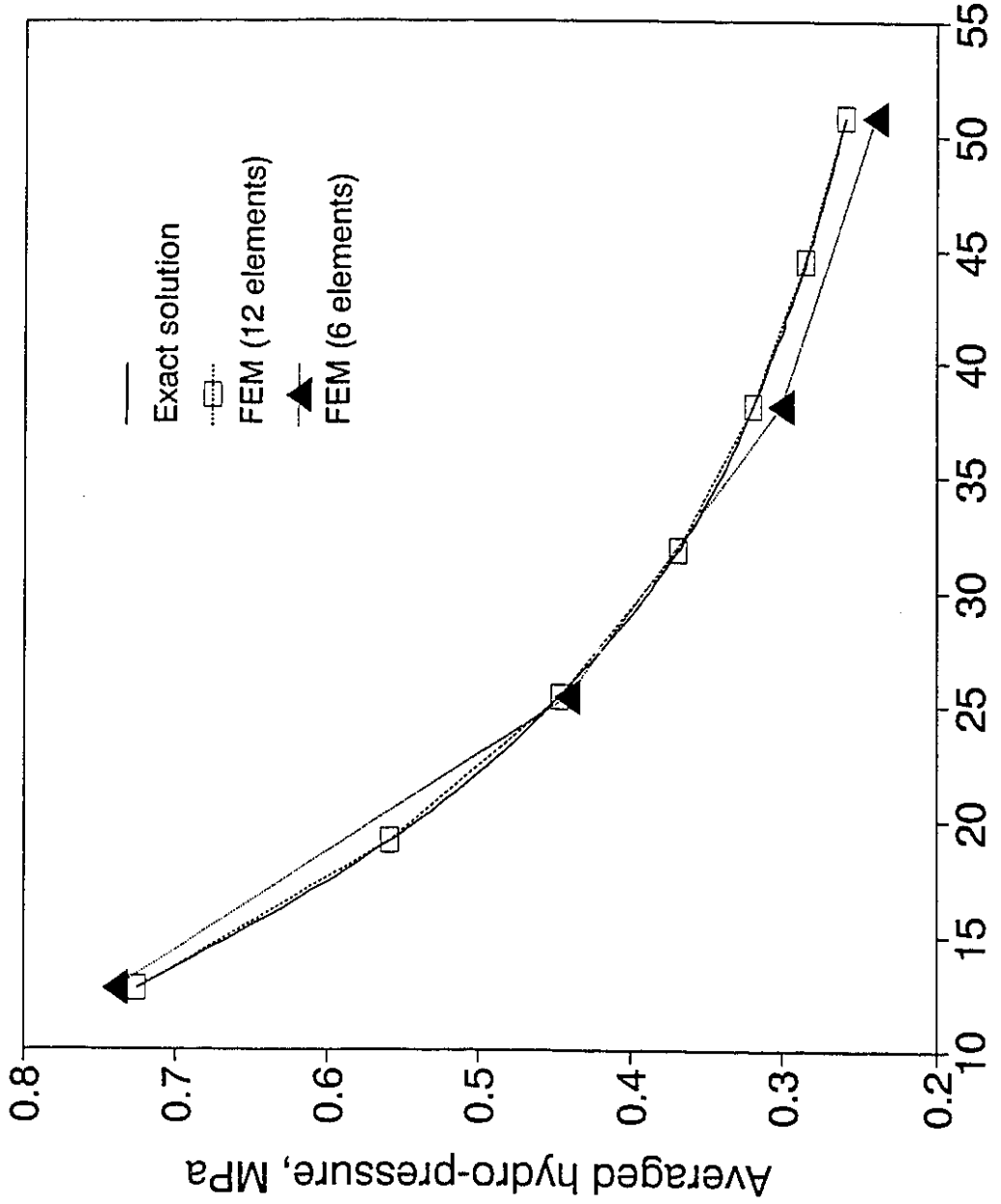

Figure 3.4 A comparison of calculated hydro-pressure with exact solution.

CHAPTER 4
SIMULATION OF PRACTICAL POLYMER THERMOFORMING

4.1 Introduction

In the process of thermoforming, a thermoplastic sheet, usually extruded from a sheet die, is heated until soft and formed by use of pressure (or vacuum) for the fabrication of numerous products, as described by Throne (1987), Florian (1987) and Whiteside (1990). Products range from small household containers, to large technical mouldings (boats, freezer liners, car bumpers, aircraft window reveals, garage doors, and honeycomb composites). Thermoplastics most widely used in thermoforming are acrylonitrile-butadiene-styrene (ABS), polymethyl methacrylate (PMMA), high impact polystyrene (HIPS), polyvinyl chloride (PVC), polystyrene (PS), polycarbonate (PC), polyproplene (PP), low density polyethylene (LDPE) and high density polyethylene (HDPE), composite materials, co-extruded sheets and multi-color laminated materials. Examples are listed in Table 4.1. Thermoforming takes on more engineering applications.

In its simplest (idealized) form, thermoforming involves inflation of a polymeric sheet originally of uniform (known) thickness. One of the most important problems in this process is the determination and optimization of sheet thickness variation, which is a function of processing conditions and rheological properties of the softened plastic sheet.

In vacuum forming, a common thermoforming technique (Figure 4.1), a

Table 4.1 Polymeric materials used in thermoforming

Material	*Application*	*Comments*
ABS/S-HIP	Refrigerator	Ease of Forming, oil/fat resistance
Matt ABS/high heat ABS	Motor trade Dashboard area	Non-reflective, Good heat distortion
PP/filled PP	Motor trade parcel Shelves	Cost effective, rigid
PP UV stable/ PP copolymer	Outdoor applications- garage forecourts	UV stabilizing, expensive-top layer only
Three layer, with scrap in centre	Various	Cost effective
PC, PEI, ABS, HIPS SURLYN	Construction Composites	High strength, UV stabilizing
Crystallisable PET	Oven tray	High temperature-resistance

sheet is shaped by reducing air pressure between it and a mold. Only air pressure is used to do the shaping, and strong molds are not required. Vacuum forming using a female mold gives better thickness at rims, but thinner corners and base. A male mold can produce the same basic shape with better thickness distribution. In pressure forming, another thermoforming technique, pressure is applied rather than vacuum. The advantage of this technique is that higher pressures can be used, especially for the forming of large area article. Plug-assist pre-stretching process can be used to promote uniformity of thickness distribution.

Recently, finite element modeling of thermoforming has been reviewed by DeLorenzi and Nied (1991) and Song et al. (1991 (a)). Investigations which are briefly summarized below are of considerable importance to the present method and objectives.

The pioneering work of Treloar (1944, 1976) involved the inflation of

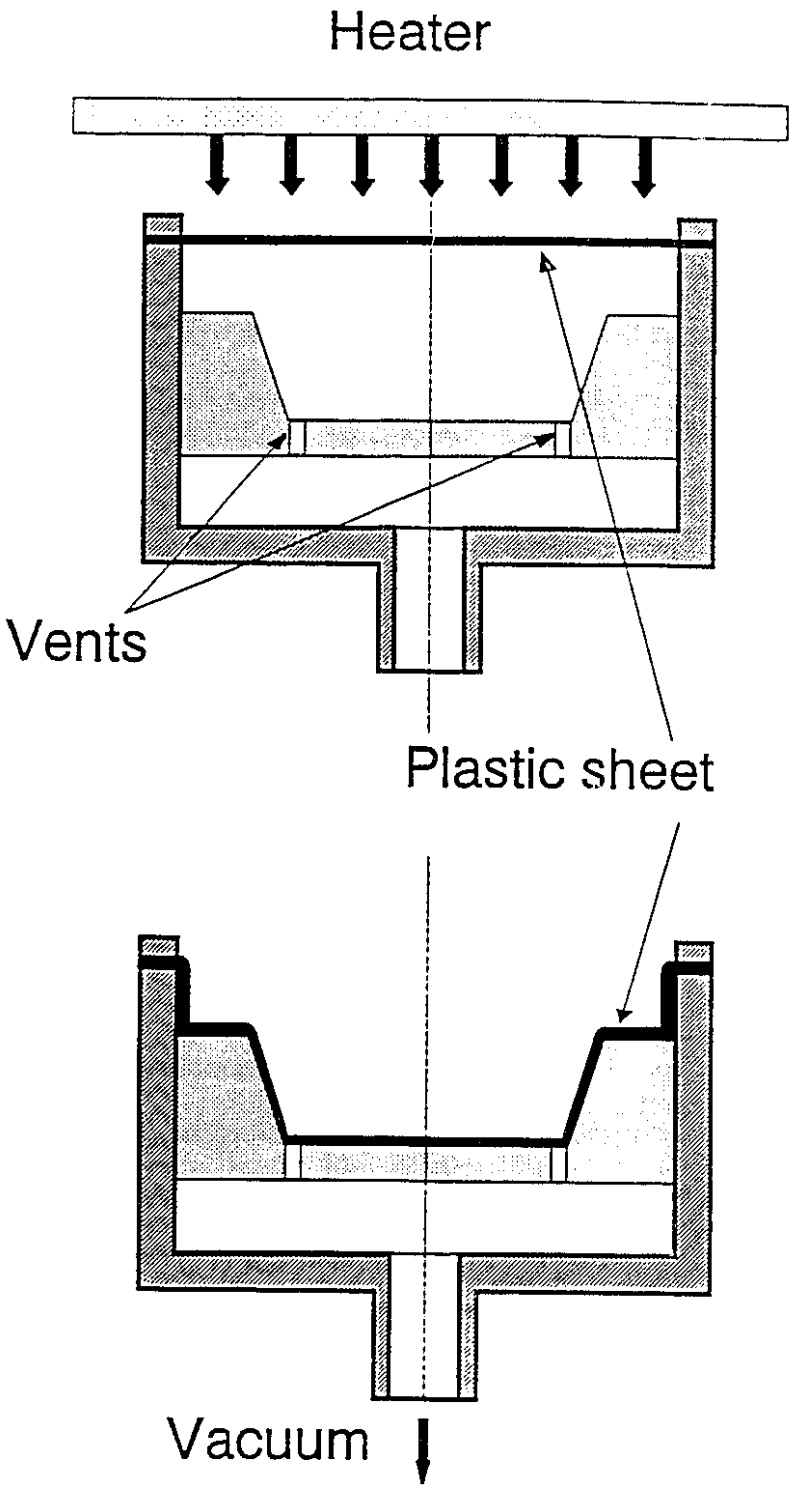

Figure 4.1. Vacuum forming process.

thick rubber sheets. Schmidt and Carley (1975 (a) and (b)) investigated the inflation of various thick thermoplastic sheets, as well as Lai and Holt (1975). Treloar and Schmidt and Carley offered convincing evidence that the thermoforming process can be well described by using a hyperelastic constitutive equation. However, Lai and Holt used a simple viscoelastic equation for stress relaxation and strain hardening to analyze their results for PMMA and HIPS.

Many analytical and numerical investigations of thermoforming, published thus far, involve thin membrane approximation, which may neither give good simulation of thicker gauge product and multi-layer composites, nor provide information of stress concentration at some critical locations as noted by Song et al. (1991 (a)). Membrane approximation is used by Allard et al. (1986), Delorenzi and Nied (1987, 1991), Warby and Whiteman (1988), Menges and Weinand (1988), Kueppers and Michaeli (1990) and Kouba et al. (1992). Oden (1971, 1972), however, developed a finite element model to describe the inflation process for a sheet of finite thickness. Song et al. (1991 (a) and (b)) also developed general finite element models with a penalty method to simulate practical thermoforming of plactics. Igl and Osswald (1992) used an one-dimensional shell finite element model to study the thermoformability of woodfiber filled polyolefin composites.

In the membrane approximation, all physical variables are assumed constant across thickness. Determination of thickness in different sections of thermoformed product is achieved by assuming incompressibility. If two extension ratios in membrane are known, the extension ratio in thickness direction can be obtained immediately from constant volume condition. Without membrane assumption, strains and stresses are allowed to vary along thickness

direction, as in the cases of thermoforming of thick sheet, or of composite sheet. Incompressibility must be considered from the start of analysis, instead of as a post-process condition, which increases accuracy dramatically, as well as difficulty.

4.2 Finite Element Simulation of Thermoforming

4.2.1 Hyperelastic Models used

A widely used hyperelastic model is the Mooney model, in which

$$W = C_{10}(I_1 - 3) + C_{01}(I_2 - 3) \tag{4.1}$$

In an axisymmetric case, the stresses contributed from W are

$$\begin{cases} \bar{S}^{11} = \dfrac{\partial W}{\partial \gamma_{11}} = 2\ [\ C_{10} + 2\ C_{01}(1 + \gamma_{22} + \gamma_{33})] \\ \bar{S}^{22} = \dfrac{\partial W}{\partial \gamma_{22}} = 2\ [\ C_{10} + 2\ C_{01}(1 + \gamma_{33} + \gamma_{11})] \\ \bar{S}^{12} = \dfrac{\partial W}{\partial \gamma_{12}} = -\ 4\ C_{01}\ \gamma_{21} \\ \bar{S}^{33} = \dfrac{\partial W}{\partial \gamma_{33}} = 2\ [\ C_{10} + 2\ C_{01}(1 + \gamma_{11} + \gamma_{22})] \end{cases} \tag{4.2}$$

and $\bar{S}^{21} = \bar{S}^{12} = -\ 4\ C_{01}\gamma_{12}$.

Even though $\gamma_{12} = \gamma_{21}$ from the balance of angular momentum, in the derivation of (4.2), independence of all strain components γ_{ij} must be retained. Otherwise, the derived $\bar{S}^{12}$ will be two times the real one. Consequently, the corresponding Jacobian stiffness matrix (3.4.8) can not be correctly evaluated and the numerical simulation will be unsuccessful, especially when shear deformation is not negligible, such as in compression forming. Other hyperelastic models have a similar problem.

Another popular model is Ogden model (Ogden, 1972, 1984), in which the

strain energy is written as an expansion in principal stretch ratios, λ_1, λ_2, and λ_3:

$$W = \sum_k \frac{\mu_k}{\alpha_k} \left[\lambda_1^{\alpha_k} + \lambda_2^{\alpha_k} + \lambda_3^{\alpha_k} - 3 \right] \tag{4.3}$$

where α_k and μ_k are experimentally determined parameters. Usually, three terms, i.e. $k = 3$, with six constants are sufficient for an excellent description of various thermoplastic materials. This model has one restraint that W in eq.(4.3) must be a positive strain energy function. Mooney model could be regarded as a special case of Ogden model when $k = 2$, $\alpha_1 = 2$, and $\alpha_2 = -2$. The axisymmetric components of the 2nd Poila-Kirchhoff stress corresponding to (4.3) are:

$$\begin{cases} \bar{S}^{11} = \sum_k \frac{\mu_k}{2} \left[\lambda_1^{\alpha_k - 2} (1 + \phi_2) + \lambda_2^{\alpha_k - 2} (1 - \phi_2) \right] \\ \bar{S}^{22} = \sum_k \frac{\mu_k}{2} \left[\lambda_1^{\alpha_k - 2} (1 - \phi_2) + \lambda_2^{\alpha_k - 2} (1 + \phi_2) \right] \\ \bar{S}^{12} = - \sum_k \frac{\mu_k}{\phi_1} \left[\lambda_1^{\alpha_k - 2} - \lambda_2^{\alpha_k - 2} \right] \cdot 2\gamma_{21} = \bar{S}^{21} \\ \bar{S}^{33} = \sum_k \mu_k \lambda_3^{\alpha_k - 2} \end{cases} \tag{4.4}$$

where

$$\begin{cases} \phi_2 = (\gamma_{11} - \gamma_{22})/\phi_1 \\ \phi_1 = [(\gamma_{11} + \gamma_{22})^2 - \phi]^{1/2} \\ \phi = 4(\gamma_{11}\gamma_{22} - \gamma_{12}\gamma_{21}) \end{cases} \tag{4.5}$$

ϕ has been previously given in eq. (2.2.31).

Eq.(4.4) is also used in the finite element formulation of this project.

4.2.2 General Process Simulation without Limit Point

The total Lagrangian description of motion (Argyris et al. 1979) and isothermal hyperelastic constitutive equations are used in the finite element formulation. Incompressibility assumption is satisfied approximately by using a penalty method. A standard incremental loading method and Newton-Raphson iteration are employed for the regular loading procedure. Since the pressure loading changes its direction with deformation, the contribution of this loading to the stiffness matrix can not be neglected as Delorenzi and Nied did in their membrane analysis. All contributions to stiffness are included in the present formulation, i.e. small deflection stiffness, tangential stiffness, initial displacement, and load (or initial stress) stiffness. Due to the unsymmetrical property of the load stiffness contribution an unsymmetrical frontal solver is used.

While the analysis presented in this project is important in thermoforming it is also significant to mention that membrane stretching is used in rheological instruments (Denson and Hylton, 1980 and Rhi-Sausi and Dealy, 1981). Possibly, some end effects encountered with these instruments may be due to thickness variations observed in this work.

Subsequent numerical examples have geometrical characteristics shown in Figure 4.2 with simplified boundary conditions, i.e., either clamped ends where the plate can not freely rotate, or simple supported ones where free rotation is allowed. The bottom surface of the sheet is subjected to uniformly distributed pressure loading q. Due to symmetry, only half of the problem domain is discretized.

Figure 4.3 (a) shows both an undeformed finite element grid of twenty elements and a deformed one, at which the loading is about 40.1 psi. It can be

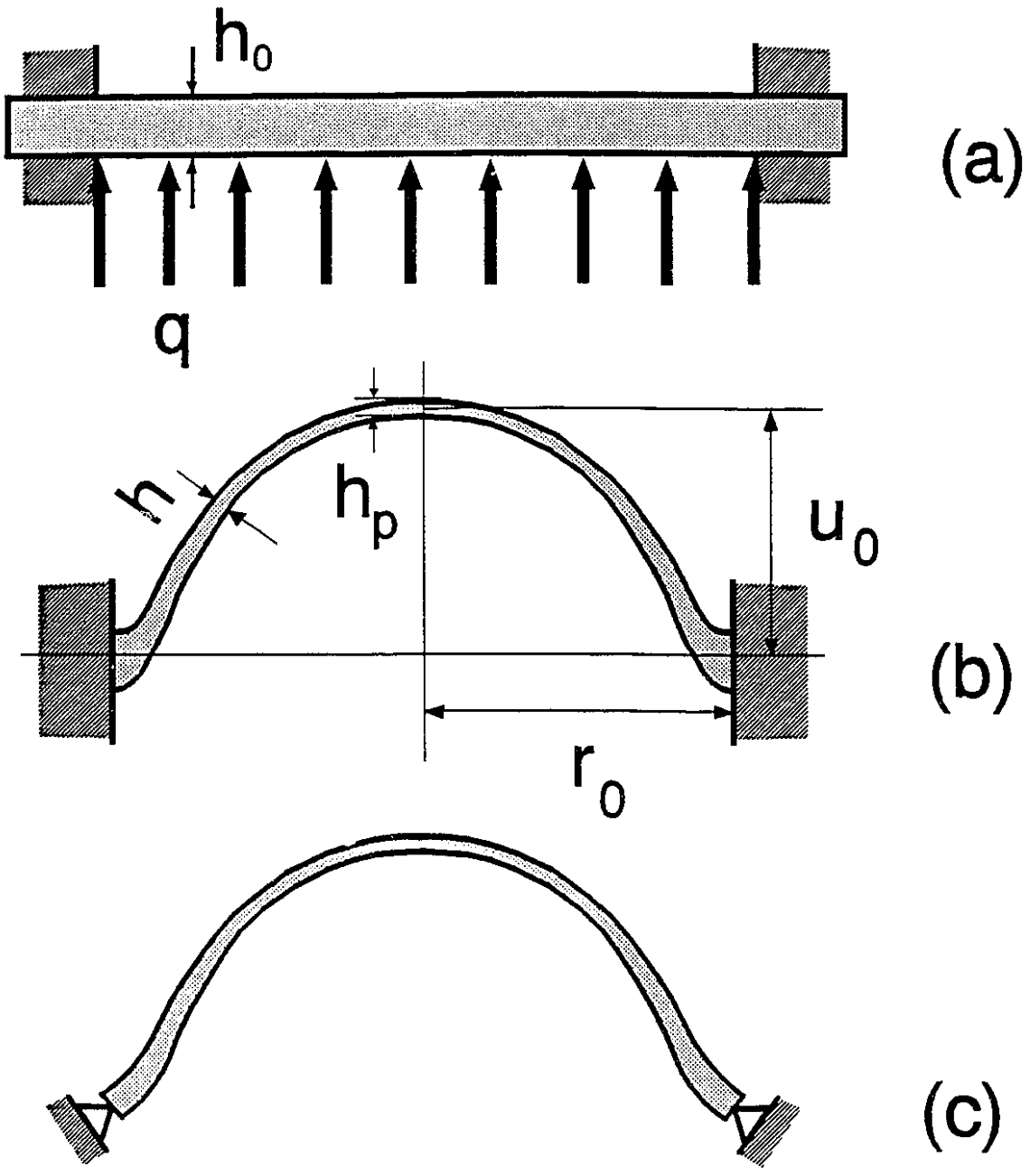

Figure 4.2. Geometry and boundary conditions for inflation of a thick plate. (a) Initial profile, (b) Simple supported ends, and (c) Clamped ends.

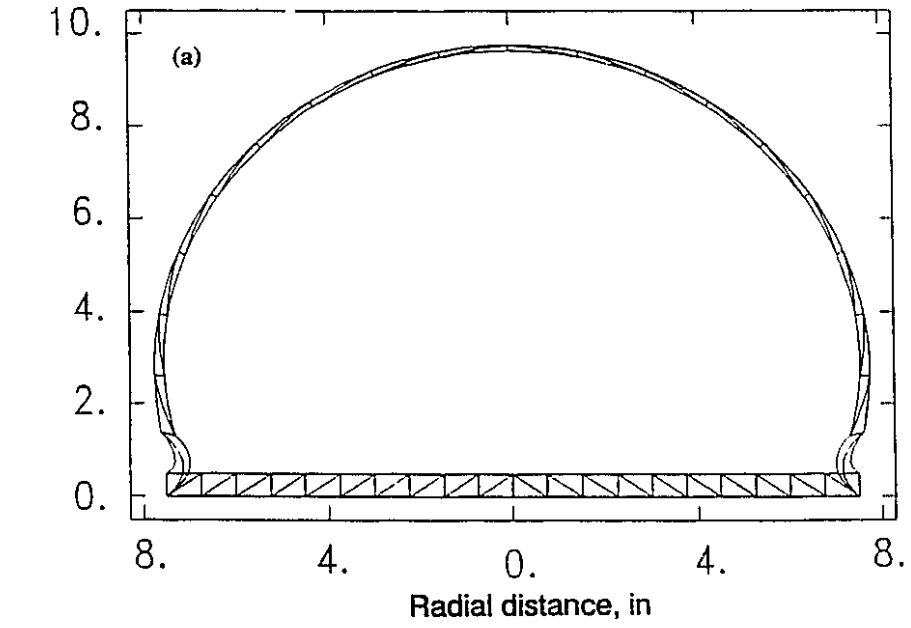

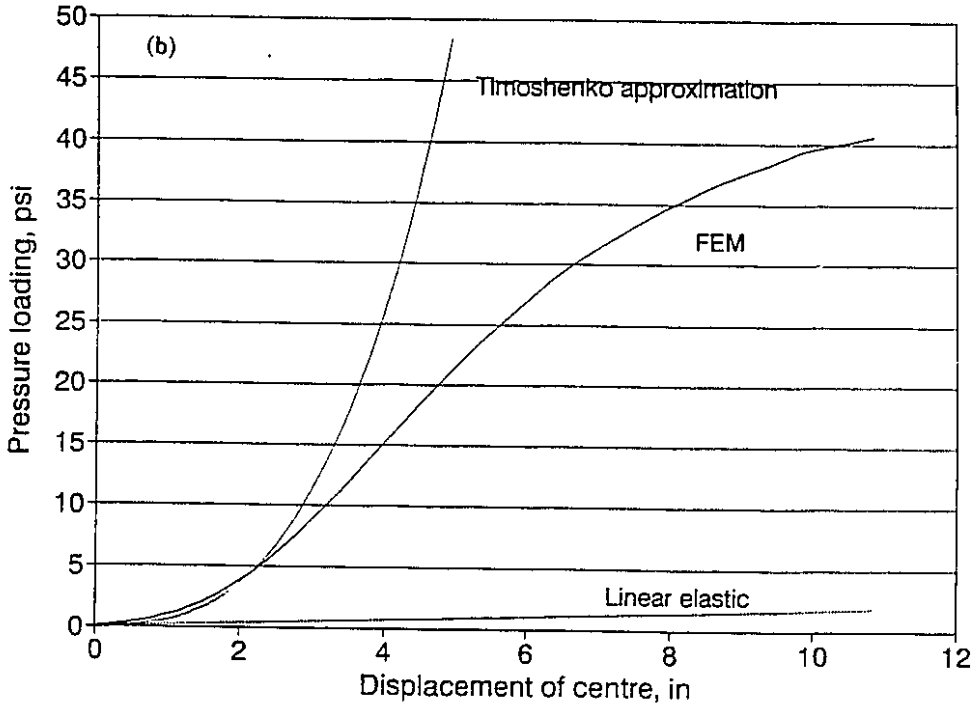

Figure 4.3 Inflation of a thick plate.
(a) Finite element grids, and (b) A comparison of theoretical solutions with finite element simulation.

seen that large deformation and large strain occur. The relation between displacement of the centre and applied pressure loading is shown in Figure 4.3 (b). Finite element results are compared with those of linear elastic theory and an approximately nonlinear analytical solution (Timoshenko et al. 1968). The nonlinear analytical solution is derived from an energy method with assumptions that the deformed profile is of spherical shape and without shear deformation. Timoshenko's simple formula, for clamped edge, is

$$u_0 = \frac{q r_0^4}{D} \frac{1}{64 + \frac{28.2828}{(1-\nu^2)h_0^2} u_0^2} \tag{4.6}$$

where u_0 is displacement of centre, $D = \frac{E h_0^3}{12(1-\nu^2)}$, bending modulus, ν, poisson's ratio. In the current study, materials are assumed to be incompressible, i.e., poisson's ratio $\nu = 0.5$. Young's modulus E has a relationship with the material parameters in Mooney hyperelastic model, from a theoretical analysis of small deformation (Alexander, 1968)

$$E = 6 (C_{01} + C_{10}) \tag{4.7}$$

The dashed line in Figure 4.3 (b) corresponds to the prediction of linear elastic theory, while the dotted line, that of Timoshenko's solution. We see nonlinear solutions apart from the linear one at very small displacement, and both nonlinear solutions match until u_0 = 2 cm. After that, the solution of Timoshenko becomes much stiffer than the finite element solution. The involved parameters are the same as those of case 6 given in Table 4.2.

4.3 Simulation of Thermoforming with Limit Point

4.3.1 Modified Riks' Method* to pass the Limit Point

In his experiments of rubber sheet inflation Treloar (1944) observed that the applied inflation pressure started to decrease after reaching a maximum, while deformation keeps increasing. Accurate pressure measurements have confirmed that such a pressure drop also occurs during thermoforming of plastics (deLorenzi and Nied, 1991). The maximum pressure point is a typical limit point, where the loading parameter q will change from increasing with time to decreasing with time, or vice versa, as shown at points D and E in Figure 4.4. In finite element simulation, the stiffness matrix in a standard incremental loading/Newton-Raphson iteration algorithm becomes singular at limit points and the solution process requires modification. A general finite element program should be capable to locate and continue beyond limit points. It should be pointed out that the limit point met in thermoforming is not a physical unstable point. The importance of passing the limit point for the numerical simulation of thermoforming has been realized by previous researchers (Allard et al. 1986, and deLorenzi and Nied, 1991). However, none of the previous finite element analyses solved this numerical instability problem. Riks' method is modified and used in this thesis (Ramm, 1981) to pass the limit point. The numerical algorithm is rather simple.

Suppose equilibrium equations in the finite element form are

$$F_\alpha(\mathbf{u}, q) = W_\alpha^{in}(\mathbf{u}) - q\, W_\alpha^{ex}(\mathbf{u}) = 0;\ \alpha = 1, 2, \ldots, n \tag{4.8}$$

where $\mathbf{u}$ is the unknown displacement vector of length n and q is a loading parameter. In Riks' method, arc-length s along equilibrium curve is chosen as the incremental parameter so that

---

* Riks' method is a special case of continuation method (Mittelmann, H.D., "A pseudo arc length continuation method for nonlinear eigenvalue problems", *SIAM J. Numerical Analysis*, 23, 1007-1016 1986.)

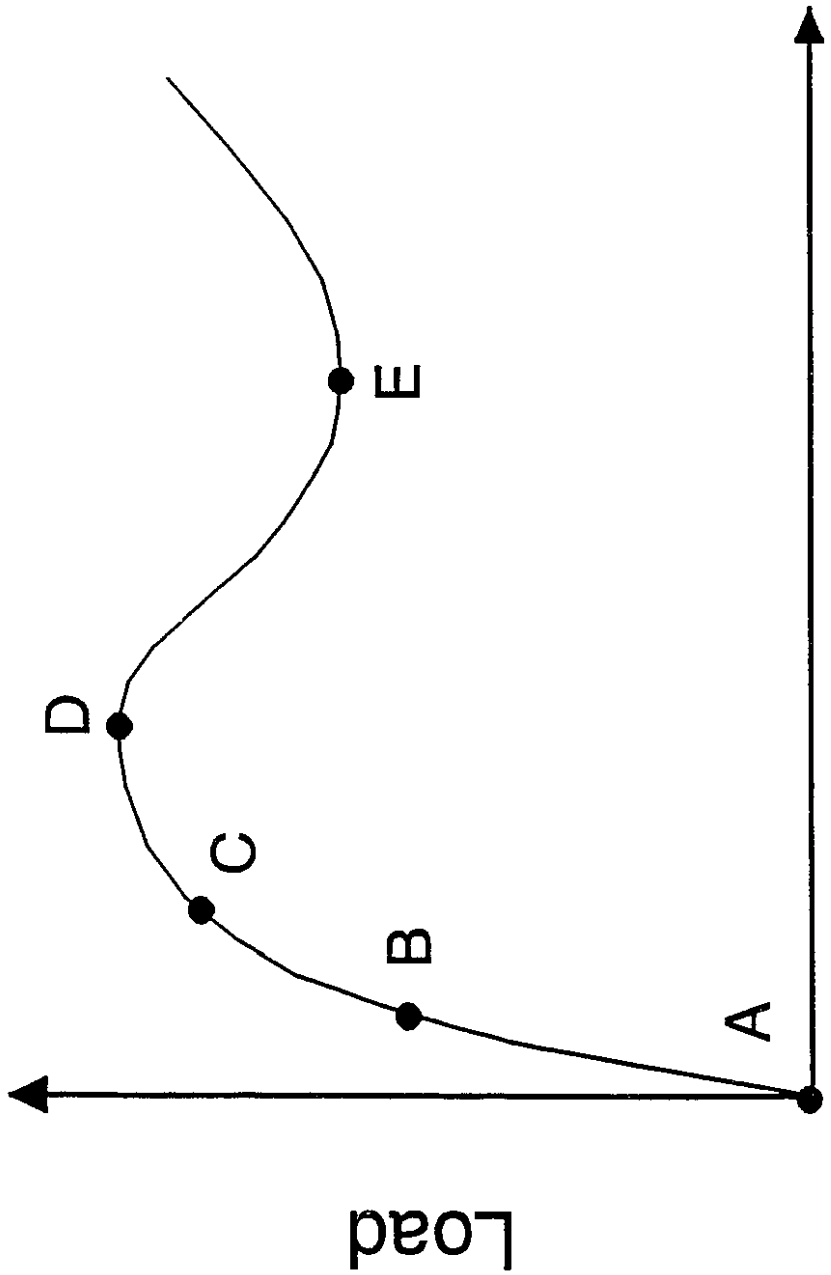

Figure 4.4 Typical loading curve with limit points.

$$\mathbf{u} = \mathbf{u}(s), \quad q = q\ (s) \tag{4.9}$$

Generally, the arc-length is defined by

$$(\mathrm{d}s)^2 = (\mathrm{d}q)^2 + \mathrm{d}\mathbf{u}\cdot\mathrm{d}\mathbf{u} \tag{4.10}$$

The incremental procedure is to find the increments of $\mathbf{u}$ and q for a given value of s and Δs. Δq becomes an extra unknown besides $\Delta\mathbf{u}$ vector. Since Δs always increases as the loading process proceeds, it can be proven that the solution of arc-length method always exists if small steps are taken (Riks, 1979). It is convenient to define a new solution vector $\mathbf{x} = \mathbf{x}(s)$ where

$$\begin{aligned} x_\alpha(s) &= u_\alpha(s); \quad \alpha = 1,\ 2,\ \ldots,\ n \\ x_\alpha(s) &= q(s); \quad \alpha = n+1 \end{aligned} \tag{4.11}$$

Then, in addition to the equations of equilibrium (4.8), a constraint equation must be satisfied

$$1 = \left[\frac{\mathrm{d}q}{\mathrm{d}s}\right]^2 + \left[\frac{\mathrm{d}\mathbf{u}}{\mathrm{d}s}\right]\cdot\left[\frac{\mathrm{d}\mathbf{u}}{\mathrm{d}s}\right] \tag{4.12}$$

or

$$1 = \dot{\mathbf{x}} \cdot \dot{\mathbf{x}} \tag{4.13}$$

where $\dot{\mathbf{x}} = \dfrac{\mathrm{d}\mathbf{x}}{\mathrm{d}s}$.

Suppose that a solution vector $\mathbf{x}^*$ and its tangent vector $\dot{\mathbf{x}}^*$ are known at some point s^* on the equilibrium curve, as shown in Figure 4.5. Let Δs represent an approximation to an increment in arc length. Then an estimate of the solution vector for the next step is

$$\mathbf{x}^0 = \mathbf{x}^* + \Delta s\, \dot{\mathbf{x}}^* \tag{4.14}$$

Now, define a plane in $n + 1$ space which has $\dot{\mathbf{x}}^*$ as its normal and passes through the point $\mathbf{x}^0$. This plane is approximated by

$$F_0(\mathbf{x}) = \dot{\mathbf{x}}^* \cdot (\mathbf{x} - \mathbf{x}^*) - (s - s^*) = 0 \tag{4.15}$$

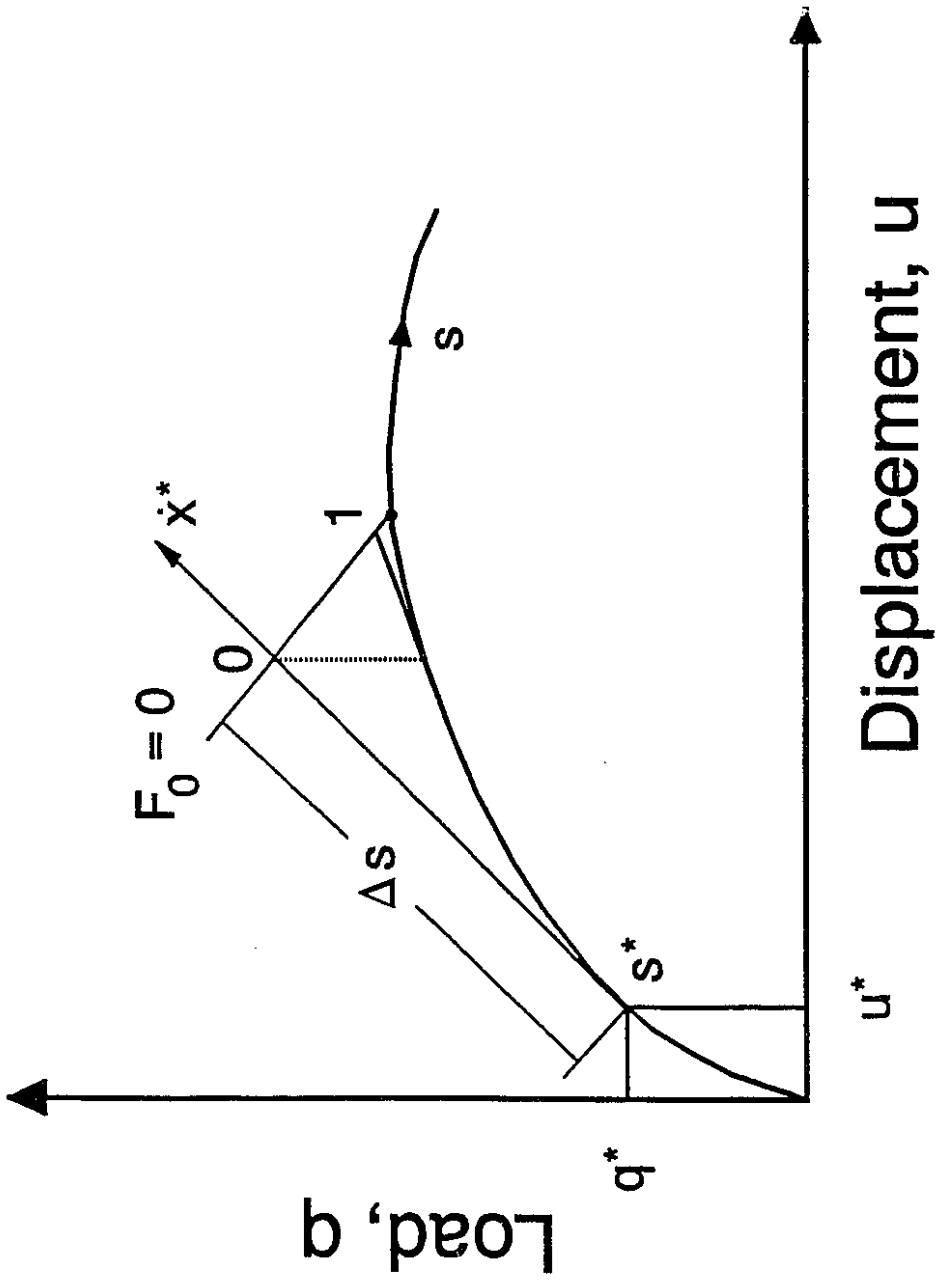

Figure 4.5 Sketch of a modified Riks' method.

Together with eq.(4.3), there are

$$\begin{cases} F_\alpha(x) = \dot{x}^* \cdot (x - x^*) - (s - s^*) = 0; \ \alpha = 0 \\ F_\alpha(x) = W_\alpha^{in}(x) - q(s)\, W_\alpha^{ex}(x) = 0; \ \alpha = 1, 2, \ldots, n \end{cases} \tag{4.16}$$

The introduction of plane $F_0 = 0$ produces a system of $n + 1$ equations with $n + 1$ variables (**u** plus q). The solution of eq.(4.16) is the intersection of plane $F_0 = 0$ and the equilibrium curve, and is located by using Newton iteration technique, shown in Figure 4.5.

Let $x^{(j)}$ represent the approximation to eq.(4.16) after the jth iteration, then the $n+1$ equations can be expanded in a series about $x^{(j)}$

$$F_\alpha(x^{(j)} + \Delta x^{(j+1)}) = F_\alpha(x^{(j)}) + F_{\alpha,\beta}(x^{(j)})\, \Delta x_\beta^{(j+1)} = 0 \tag{4.17}$$

where only the linear term in the series is retained, and

$$F_{\alpha,\beta}(x^{(j)}) = \frac{\partial F_\alpha(x)}{\partial x_\beta}\Big|_{x=x^{(j)}} \tag{4.18}$$

As long as matrix $F_{\alpha,\beta}$ is non-singular, eq.(4.17) can be solved for the correction $\Delta x^{(j+1)}$ and a new estimate of the solution is obtained

$$x^{(j+1)} = x^{(j)} + \Delta x^{(j+1)} \tag{4.19}$$

The iteration procedure is repeated until $\Delta x^{(j+1)}$ is sufficiently small. In this investigation, the iteration is terminated if

$$\frac{\|\Delta \mathbf{u}\|}{\|\mathbf{u}\|} \le R; \text{ and } \frac{|\Delta q|}{q} \le R \tag{4.20}$$

where R is a pre-determined tolerance.

In this work, the size of step Δs is automatically changed by

$$\Delta s^{k+1} = \frac{MIT}{KIT}\, \Delta s^k \tag{4.21}$$

where MIT is the maximum number of iterations and KIT is the actual number of iteration required for the convergence of step k. The original Riks' method

leads to modification of stiffness matrix, which greatly increases computing efforts. The modified Riks' method outlined below keeps all the merits of Riks' method without changing stiffness matrix and the extra computing effort is very small.

The numerical implementation of the modified Riks' methods with unsymmetrical frontal solver is summarized as follows:

1. Choose the zero solution vector corresponding to the undeformed configuration of body (${}^0q = 0$) as the initial solution, select a basic load increment as reference load Δq, and solve the standard incremental loading/Newton-Raphson iteration procedure to obtain equilibrium, thus the Δs in the first step is determined

$$ {}^1q = {}^0q + \Delta q, \ {}^1\mathbf{u} = {}^0\mathbf{u} + \Delta\mathbf{u}, \text{ and } (\Delta s)^2 = (\Delta q)^2 + \Delta\mathbf{u}\cdot\Delta\mathbf{u} \tag{4.22} $$

2. In any step

a) for $\Delta q' = 1$, solve the incremental equilibrium equations to obtain $\Delta\mathbf{u}'$;

b) Adjust the step size $\Delta s^{k+1} = \frac{\text{MIT}}{\text{KIT}} \Delta s^k$, or $\Delta s^{k+1} = \sqrt{\frac{\text{MIT}}{\text{KIT}}}\ \Delta s^k$. The latter is introduced to avoid oscillating.

c) Suppose the unknown loading increment is Δq, then

$$ (\Delta s^{k+1})^2 = (\Delta q)^2 + (\Delta q\ \Delta\mathbf{u}')\cdot(\Delta q\ \Delta\mathbf{u}') \tag{4.23} $$

Check for unloading. Therefore,

$$ \Delta q = \pm\Delta s^{k+1} \left[1 + \Delta\mathbf{u}'\cdot\ \Delta\mathbf{u}' \right]^{-1/2} \tag{4.24} $$

Apply negative sign when unloading. Usually, diagonal terms in the triangularized stiffness matrix during Gaussian elimination should be monitored. If some of the diagonal terms show sign changing, then loading should change to unloading, or unloading should change to loading. Through numerical experiments, we find that if the sign of Δq is kept unchanged near a

limit point, the calculated loading (after iterations) will oscillate about the loading at that point. If the sign of Δq is changed when oscillating starts, then the limit point can be successfully passed.

3. Update the solution

$$\Delta \mathbf{u} = \Delta q\, \Delta \mathbf{u}',\ \mathbf{u}^{k+1} = \mathbf{u}^{k} + \Delta \mathbf{u},\ q^{k+1} = q^{k} + \Delta q,\ s^{k+1} = s^{k} + \Delta s^{k+1} \tag{4.25}$$

4 a) determine the out-of-balance forces

$$F_{\alpha}^{k+1} = W_{\alpha}^{in}(\mathbf{u}^{k+1}) - q^{k+1} W_{\alpha}^{ex}(\mathbf{u}^{k+1}) \ (\neq 0) \tag{4.26}$$

b) Iterations

in the jth iteration, simultaneously solve

$$\begin{cases} F_{\alpha,\beta}\, \Delta^{I} u_{\beta} = \Delta q'\ W_{\alpha}^{ex}\big|_{\Delta q'=1} \\ F_{\alpha,\beta}\, \Delta^{II} u_{\beta} = -F_{\alpha}\,. \end{cases} \tag{4.27}$$

$$\Delta u_{\beta}^{(j)} = \Delta^{II} u_{\beta} + \Delta^{I} u_{\beta} \cdot \Delta q^{(j)} \tag{4.28}$$

is the solution of the original iteration equation

$$F_{\alpha}^{(j)} = F_{\alpha}^{(j-1)} + F_{\alpha,\beta}\, \Delta u_{\beta} + \frac{\partial F_{\alpha}}{\partial q}\, \Delta q^{(j)} = 0. \tag{4.29}$$

The iteration path follows a plane normal to the tangent $\left\{\frac{\Delta \mathbf{u}^{k}}{\Delta s},\ \frac{\Delta q^{k}}{\Delta s}\right\}^{T}$, that is

$$\frac{\Delta \mathbf{u}^{k}}{\Delta s} \cdot \Delta \mathbf{u}^{(j)} + \frac{\Delta q^{k}}{\Delta s} \cdot \Delta q^{(j)} = 0 \tag{4.30}$$

5. Use the above constraint equation to determine the load increment $\Delta q^{(j)}$,

$$\Delta q^{(j)} = -\frac{\Delta \mathbf{u}^{k} \cdot \Delta^{II} \mathbf{u}}{\Delta q^{k} + \Delta \mathbf{u}^{k} \cdot \Delta^{I} \mathbf{u}} \tag{4.31}$$

6. Update the load level and the displacement field;

7. Repeat steps 4-6 until the desired tolerance is achieved for both load and displacement;

8. Reformulate the stiffness matrix and start a new step by returning to 2.

4.3.2 Simulation of Large Inflation of Rubber Sheet

The problem involves large free inflation of a thick flat sheet of 8% sulphur rubber, investigated by Treloar (1944). Equibiaxial extension is achieved at the pole of the inflated sheet. Treloar's measurements of this equibiaxial extension are widely used as benchmark data to check performance of different constitutive relations (Alexander, 1968) and there is no numerical simulation compared with the measurements.

In this work, the same geometrical and material parameters as those of Treloar are used. Initial radius r_0 is equal to 1.25 cm, initial thickness h_0, 0.082 cm, and a neo-Hookean constitutive model with C_{10} being 2.0 kg/cm^2, C_{01} zero, are used. A good simulation is obtained with a rough finite element grid of only 20 elements. Little change in the results is noted by doubling the number of elements. It is worth to mention that the aspect ratio r_0/h_0 =15.24 is not very large, i.e. the sheet is not very thin. None of finite element analyses based on membrane approximation have shown any comparisons with Treloar's data for the whole inflation process.

Figure 4.6 shows that simulation is successfully carried over a limit point and matches Treloar's (1944) experimental data very well. At the pole, the membrane stresses increase with increasing extension ratio λ_2, although the applied pressure experiences decrease during the inflation. At the pole, the sheet undergoes equibiaxial extension. If the thin membrane theory is applied, there is $2kT=q$, or $T=q/2k$ at the pole. k is the curvature, T ($=T_1=T_2$) is the stress resultant along the thickness direction. In this case, the curvature k decreases at a faster speed than pressure loading q does

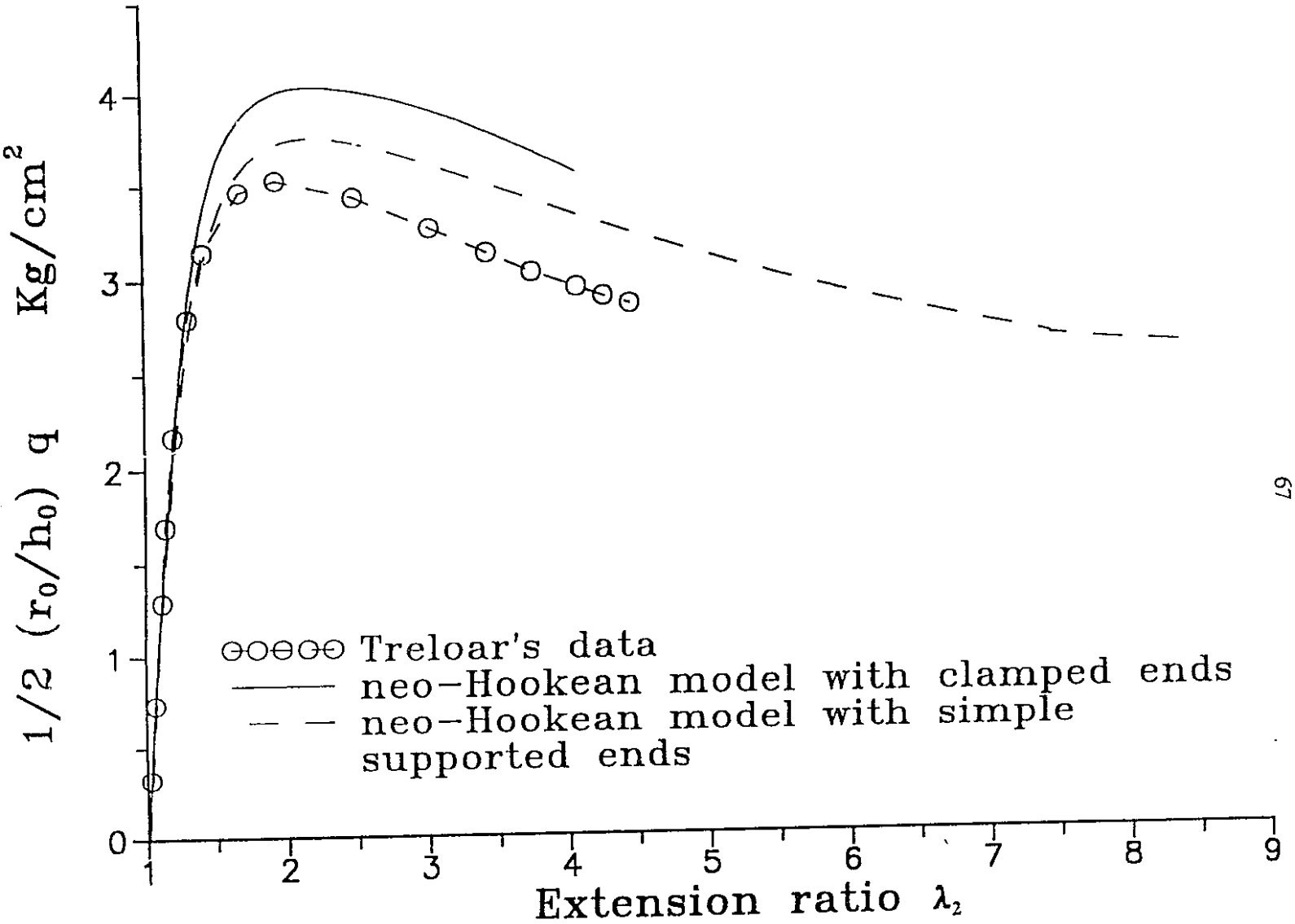

Figure 4.6 Predicted loading curve with a limit point, compared with Treloar's experimental data.

(Figure 4.7). Therefore, T keeps increasing.

Figure 4.6 indicates that the forms of boundary conditions have little effect on the loading vs. extension ratio curve until the limit point. Then, the curve corresponding to simple supported boundary conditions seems closer to Treloar's data, while that corresponding to fixed boundary conditions is stiffer. Departure of finite element calculations from experimental data may have resulted from an initial distension performed by Treloar before inflating, which is ignored in our simulation, or from limitations of neo-Hookean constitutive model. Qualitatively, we know that pre-stretching softens the sheet. Therefore, the use of simple supported boundary conditions, i.e. softer boundary conditions than the clamped ones, gives better results. Mooney model with C_{10}= 1.95, and C_{01} = 0.05 kg/cm^2 has also been tried without much improvement.

Figure 4.7 shows calculated profiles for simple supported boundary conditions, corresponding to loading levels of (q) 0.0, 0.126, 0.440, 0.493, 0.436, and 0.349 kg/cm^2. 0.493 kg/cm^2 is the maximum pressure. For the largest inflated profile shown, the sheet is spherical in shape, up to approximately r/r_0= 0.7. At low loading levels, the sheet undergoes almost uniform thinning, strains are small, but rotations are large. As loading increases, non-uniform thinning becomes dominant. Calculation for simple supported boundary conditions can be continued until the pole extension ratio (λ_2= λ_3) reaches a value as large as 8.5, with pressure about 0.349 kg/cm^2. Thickness at the pole is about 0.0012cm, 1.4 % of original thickness, and it is about 50 % near the end. Thickness variations in Figure 4.8 show that the thickness gradient is much higher near the ends.

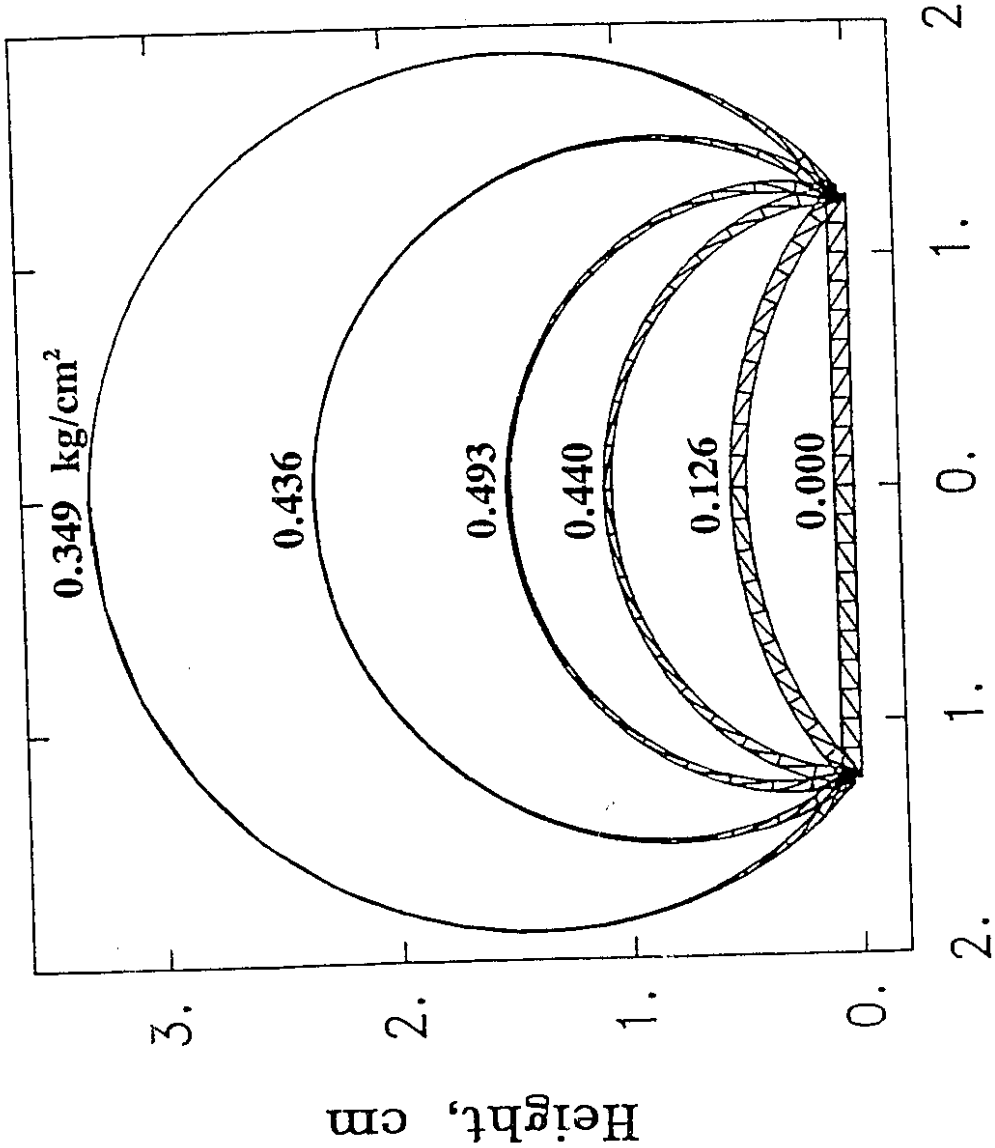

Figure 4.7 Inflated profiles with simple supported boundary.

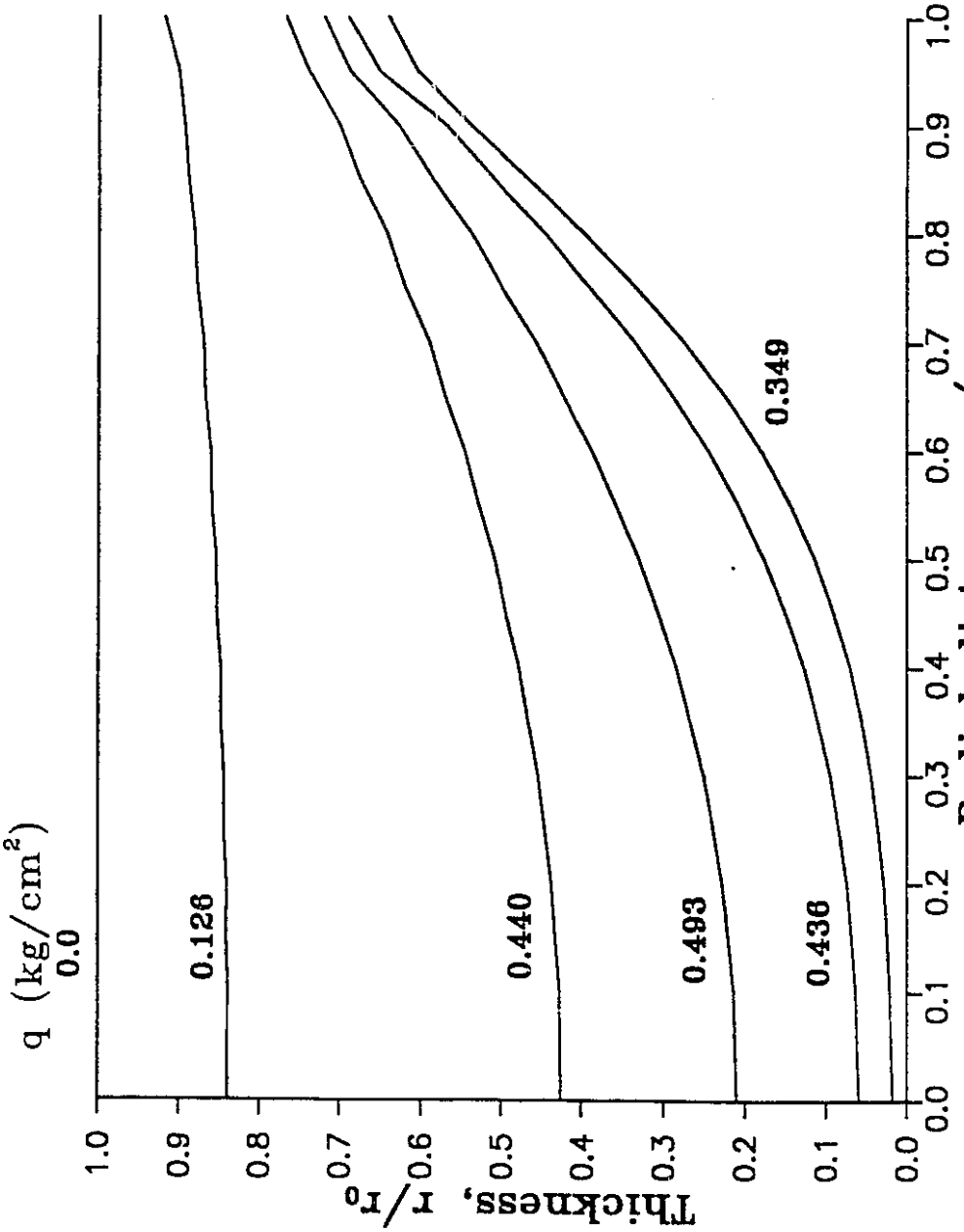

Figure 4.8 Thickness variations at various loading levels.

4.4 Effects of Material Parameters on Thermoformed Product

The second set of simulations focuses on effects of material parameters and aspect ratio. Geometrical and material parameters used are presented in Table 4.2. Case 2 corresponds to experimental measurements performed by Lai and Holt (1975) for comparison.

We use only the simple supported boundary condition for the following calculations, since the clamped boundary condition requires considerable refinement of end elements at high pressure loading, and both boundary conditions result in similar finite element results before the limit point.

Figure 4.9 shows the effect of material parameter C_{01} on pole thickness variation with pole height. C_{10} values are given in Table 4.2. For cases 4 and 6 (not shown) the curves are between those of cases 1 and 5. It appears that the greatest sensitivity is due to C_{01}.

Figure 4.10 gives dimensionless loading as a function of dimensionless

Table 4.2. Geometrical and material parameters in the case study of thermoforming

	Case					
	1	2[a]	3	4	5	6
Initial radius r_0 (in)	3.5				3.5	7.5
Initial thickness h_0 (in)	0.25				0.125	0.5
Aspect ratio r_0/h_0	14.0				28.0	15.0
C_{10} (psi)	56.0	40.0	40.0	80.0	80.0	80.0
C_{01} (psi)	20.0	0.0	36.0	20.0	20.0	20.0

[a] Lai and Holt.

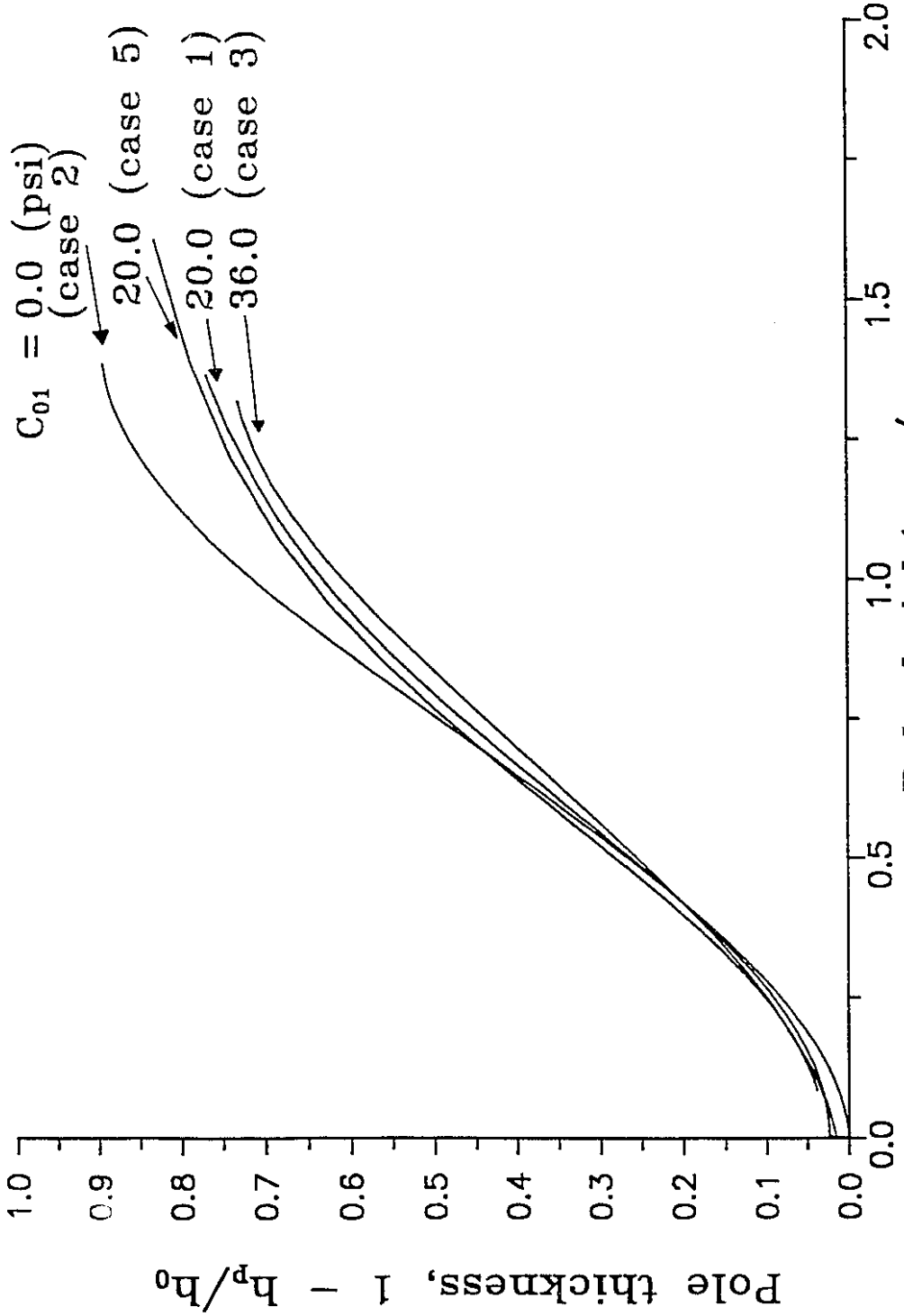

Figure 4.9 Pole thickness versus pole height for different material constants.

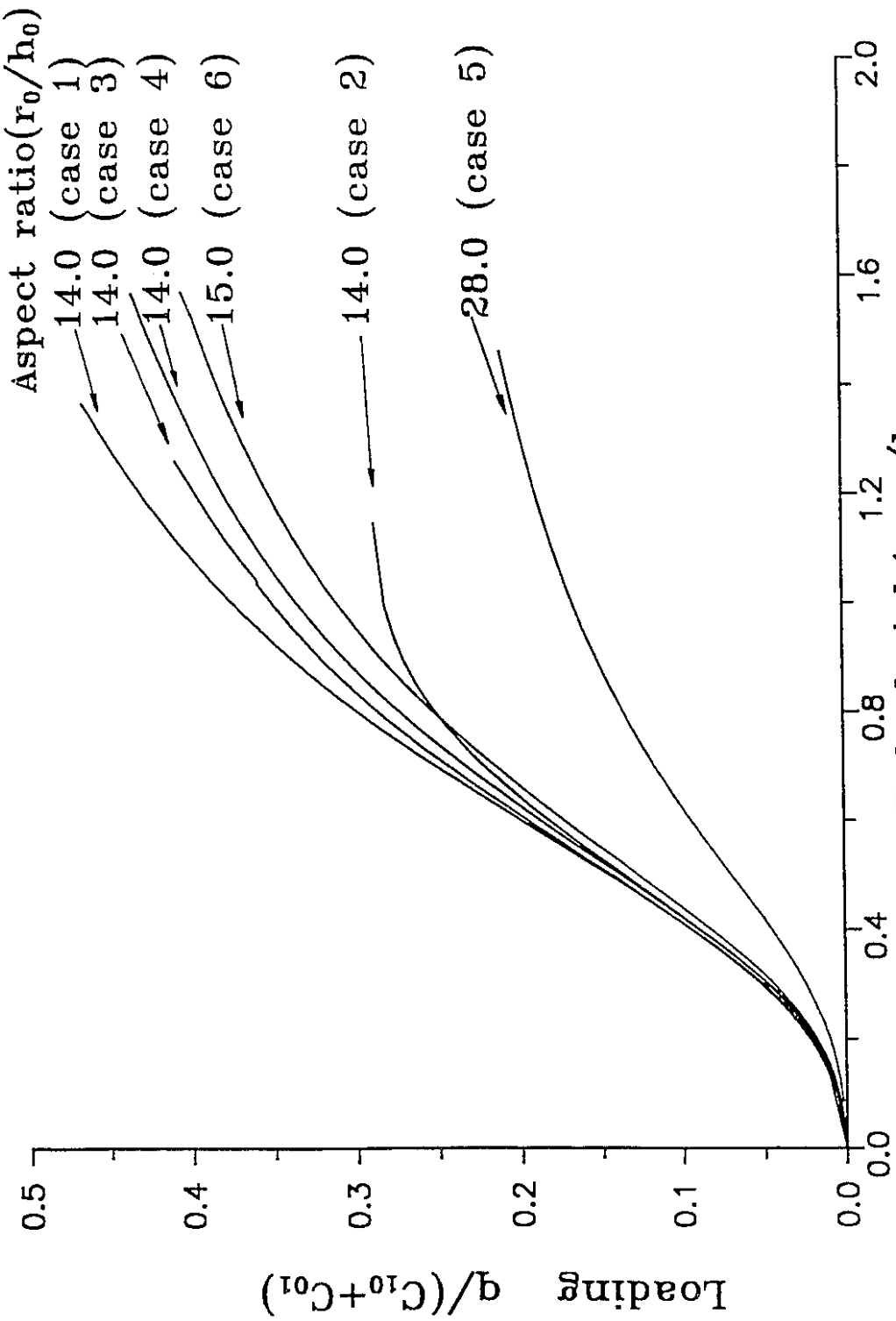

Figure 4.10 Loading versus pole height for different aspect ratios.

pole height. For the parameters studied when aspect ratio r_0/h_0= 14.0, curves are grouped together for a large portion of pole height range. The sheet with aspect ratio r_0/h_0 = 28 has a larger pole height for the same dimensionless loading, which implies more non-uniform thinning. Therefore, with the same loading and radius, the thinner the initial plate, the more the non-uniform thinning.

In Lai and Holt's experiments (1975), a viscoelastic constitutive relation is used. $\sigma = K\, t^{m'} \varepsilon^{n}$, where σ, ε and t are true stress, true strain, and time,respectively. For PMMA at 163 $^{\circ}$C, the stress relaxation index m' is equal to -0.05, and the strain hardening index n is 1.0. In this analysis stress relaxation is ignored and material is considered as nonlinear elastic (neo-Hookean model). The material constant K [$K = 6\,(C_{10} + C_{01})$] is estimated from Lai and Holt's experimental data. K is about 240.0 psi, C_{10} is taken as 40.0 psi, and C_{01} zero. A comparison of our simulation with Lai and Holt's data shows good agreement (Figure 4.11). This also suggests that use of neo-Hookean model can yield good results even for a viscoelastic material, like PMMA. However, this is not surprising, because thermoforming is a very rapid process with little time allowed for viscous dissipation. Actual forming operation averaged 6 seconds in Lai and Holt's (1975) experiments.

In determination of material parameters, it should be noted that tests of small, or medium deformation are not sufficient. The following example indicates that materials with the same value of K, but different C_{01} and C_{10}, could differ in large deformation with similar linear responses.

Free inflation of two thick thermoplastic sheets are simulated. Simple supported boundary is assumed. The values of K, original radius, and thickness for both sheets are 600 psi, 7.5 in, and 0.5 in, respectively. C_{01}= 100 psi,

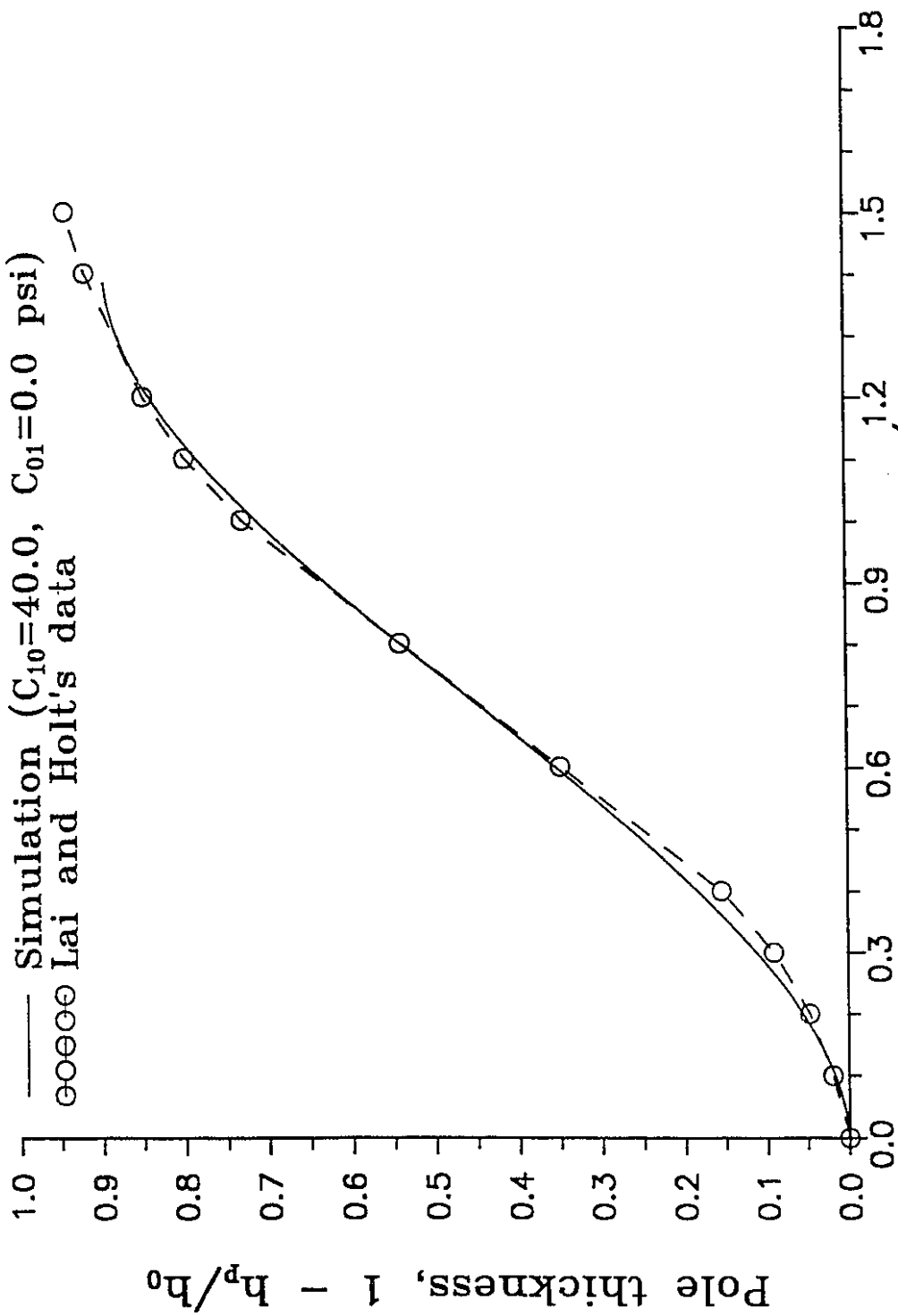

Figure 4.11 A Comparison with Lai and Holt's experiment of PMMA (r_0 = 3.5 in, h_0 = 0.25 in, C_{10} = 40.0 psi, and C_{01} = 0.0 psi).

and C_{10}= 0.0 for sheet A, while C_{01}= 80, and C_{10}= 20.0 for sheet B. When external loading is less than 15 psi, deformation responses are almost the same, see Figure 4.12. However, the responses quickly depart from each other. For example, at a pressure loading of 26 psi, the central displacement for plate B of Mooney material is about 6 in, but that of plate A reaches 9 in, as illustrated in Figure 4.13. Therefore, the determination of material parameters should include the consideration of large deformation and nonlinear properties of polymer must be taken into account in processing design.

4.5 Thermoforming of Multilayer Composite

Thermoforming of a two-layer sheet with different materials is the last problem studied. Both a "stiffer" composite and a "softer" one are studied. If a sheet is made up of a reference material with a stiffer one, then its overall load-bearing capacity is greater than that of the reference material. The composite is called "stiffer". If a less-stiff material is incorporated into the composite, the overall stiffness of the composite is less than that of the reference material, and the composite is called "softer". Table 4.3 gives various combinations of the two layer sheet. Two layers of finite elements are used to represent the two material layers. Calculated profiles are shown in Figure 4.14. It is assumed that there is no

Table 4.3. Three material models and the corresponding material parameters

	Case				Material		
	1	2	3		1	2	3
	reference	softer	stiffer				
Top layer	mater. 1	mater. 2	mater. 3	C_{10}(MPa)	0.552	0.414	0.759
Bottom	mater. 1	mater. 1	mater. 1	C_{01}(MPa)	0.138	0.0	0.276

Each layer's initial radius and thickness are r_0= 19.1 cm, h_0= 0.635 cm

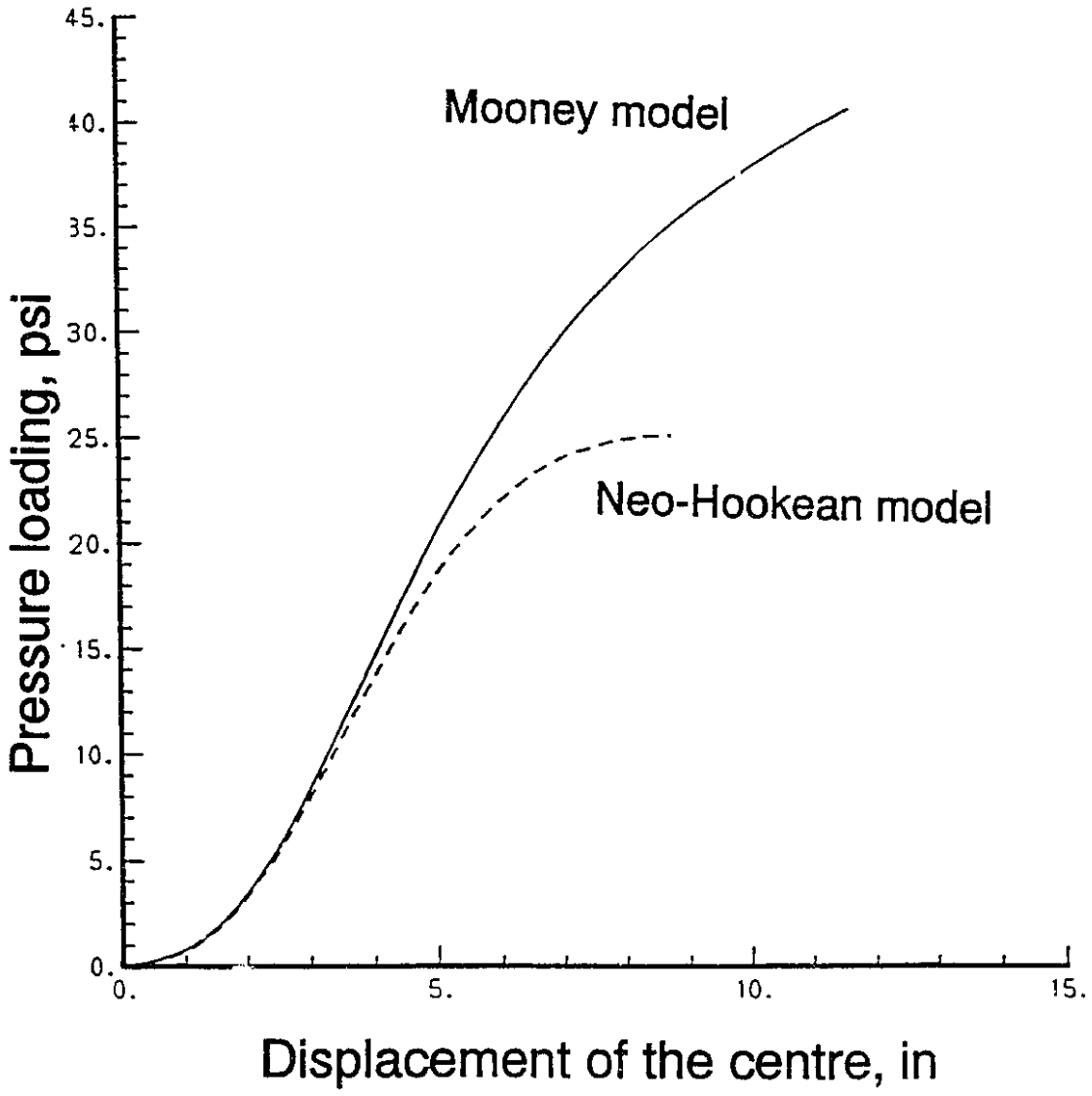

Figure 4.12 Different deformation responses of two plates with the same geometry and linear Young's modulus. (For plate A, C_{01}=100 psi, C_{10}=0.0; for B, C_{01}= 80 psi, C_{10}=20.0)

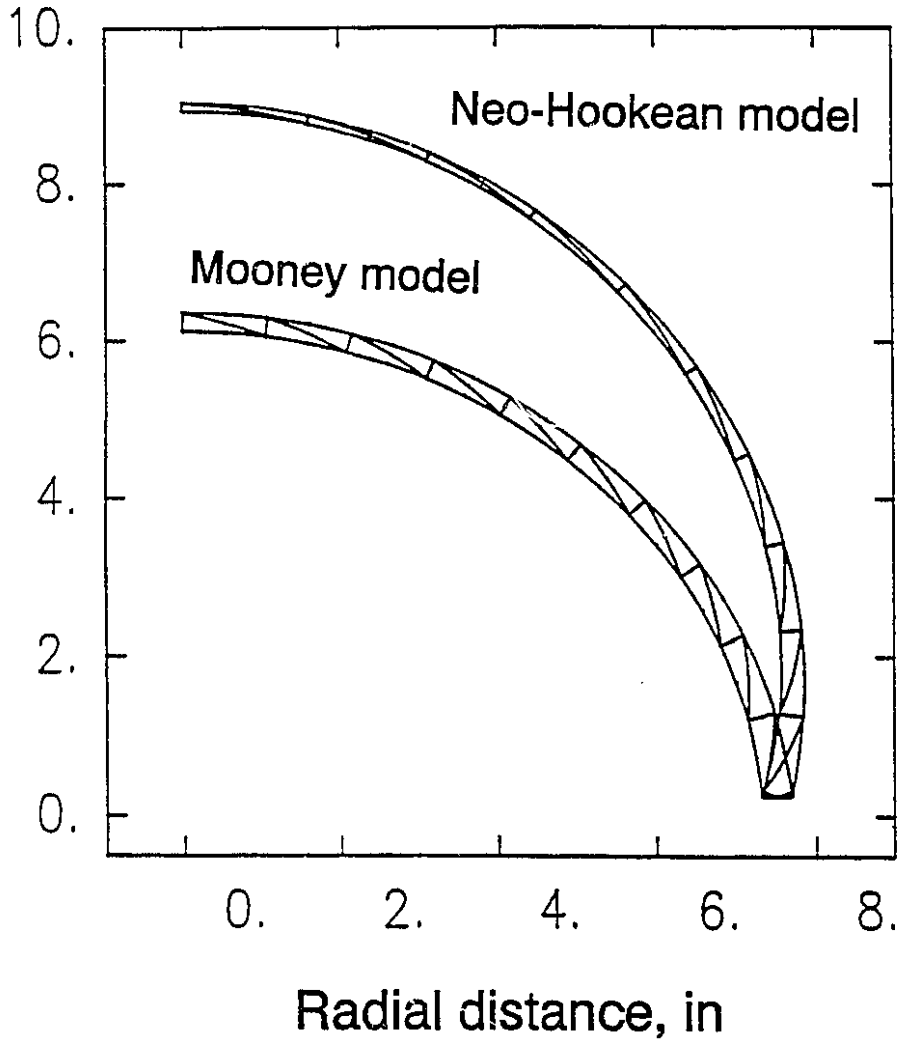

Figure 4.13 Different deformed profiles of the two plates at the same loading level of 26 psi.

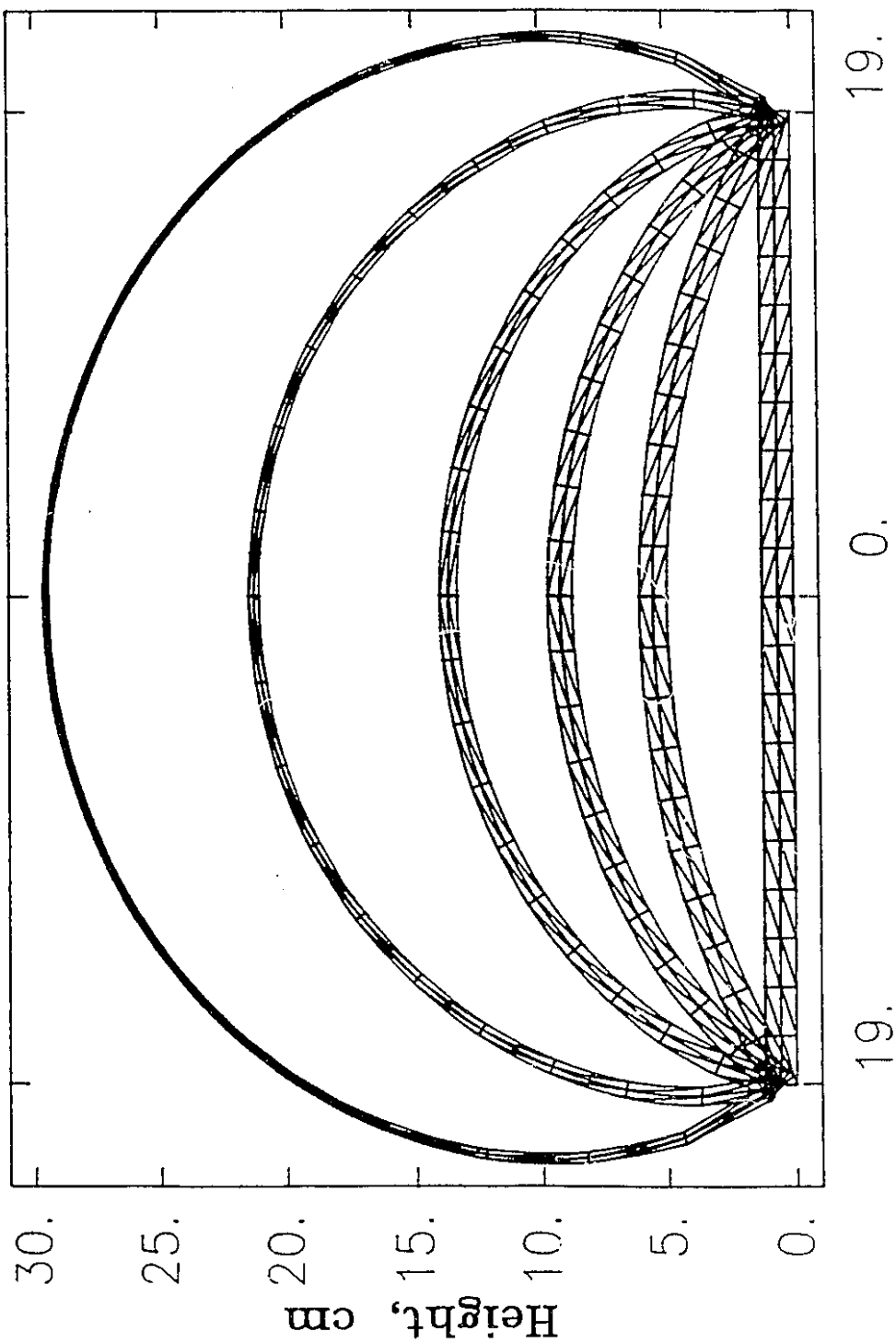

Figure 4.14 Calculated profiles of a two-layer composite sheet.

sliding between the two layers. Thickness variations for various cases studied are compared in Figures 4.15 and 4.16. It shows that for loading of 0.142 MPa the smallest thickness variation appears in the stiffer sheet.

The capability of the current finite element program to simulate thermoforming of multilayer composite is a unique advantage over thin membrane analysis.

4.6 Concluding Remarks

The finite element program developed can successfully simulate free inflation of an axisymmetric sheet of single layer, or multilayer-composite material. A hyperelastic constitutive model with properly determined material constants can be used to approximate inflation of polymer sheets which are known to be viscoelastic, primarily because thermoforming occurs in such a short time that the material behaves as an elastic solid. A comparison of present finite element calculations for inflation of thick, rubber, or PMMA, sheets with experimental data of Treloar and Lai and Holt provides good agreement. Material parameters, which influence the loading and thickness distribution of final formed product, should be determined from large deformation tests to have an accurate prediction. A modified Riks' method to deal with the limit point is introduced for the first time in the literature to simulate thermoforming.

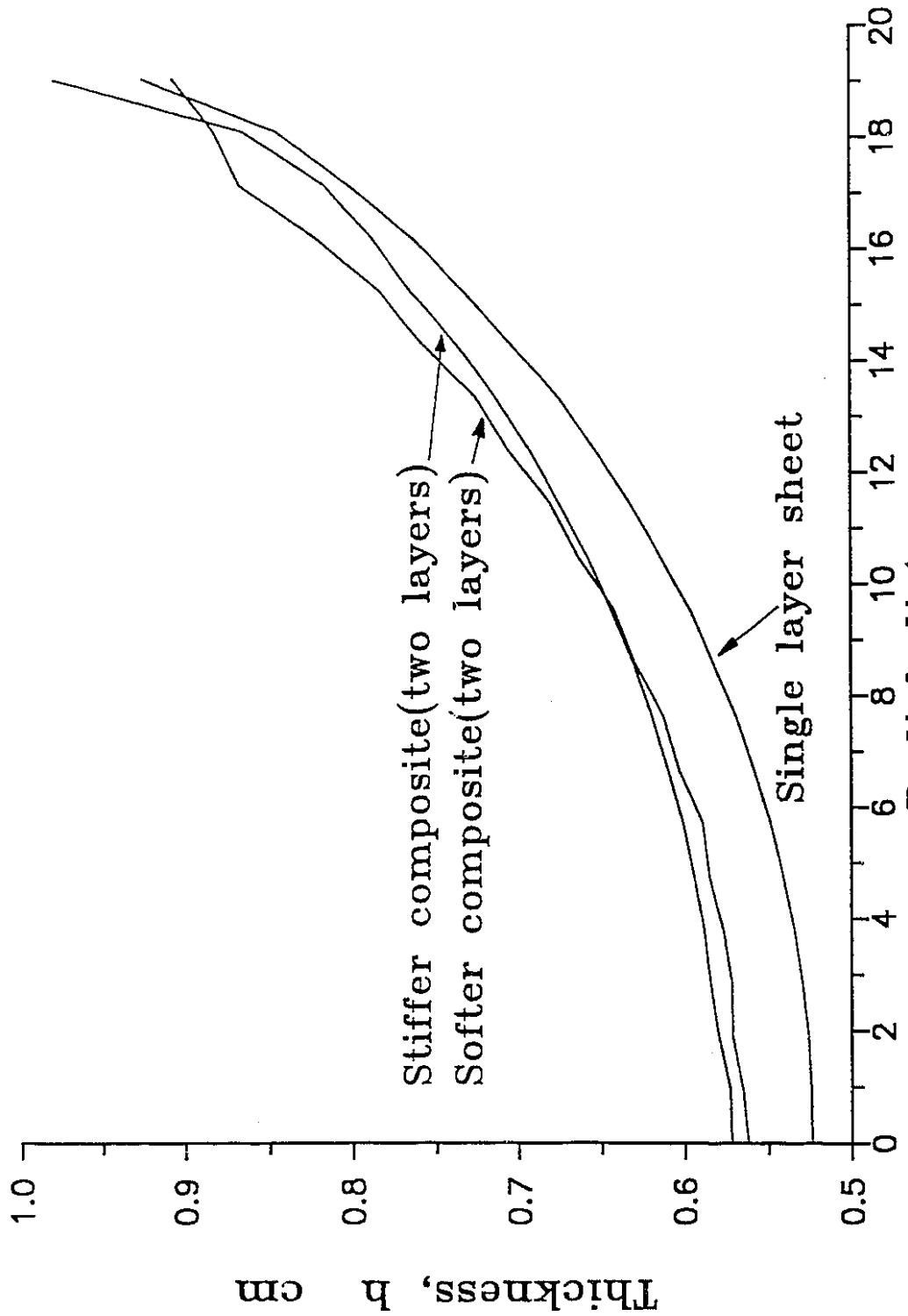

Figure 4.15 Thickness variation of different composites at the same loading level, q = 0.142 MPa. Curves shown are matched at pole position.

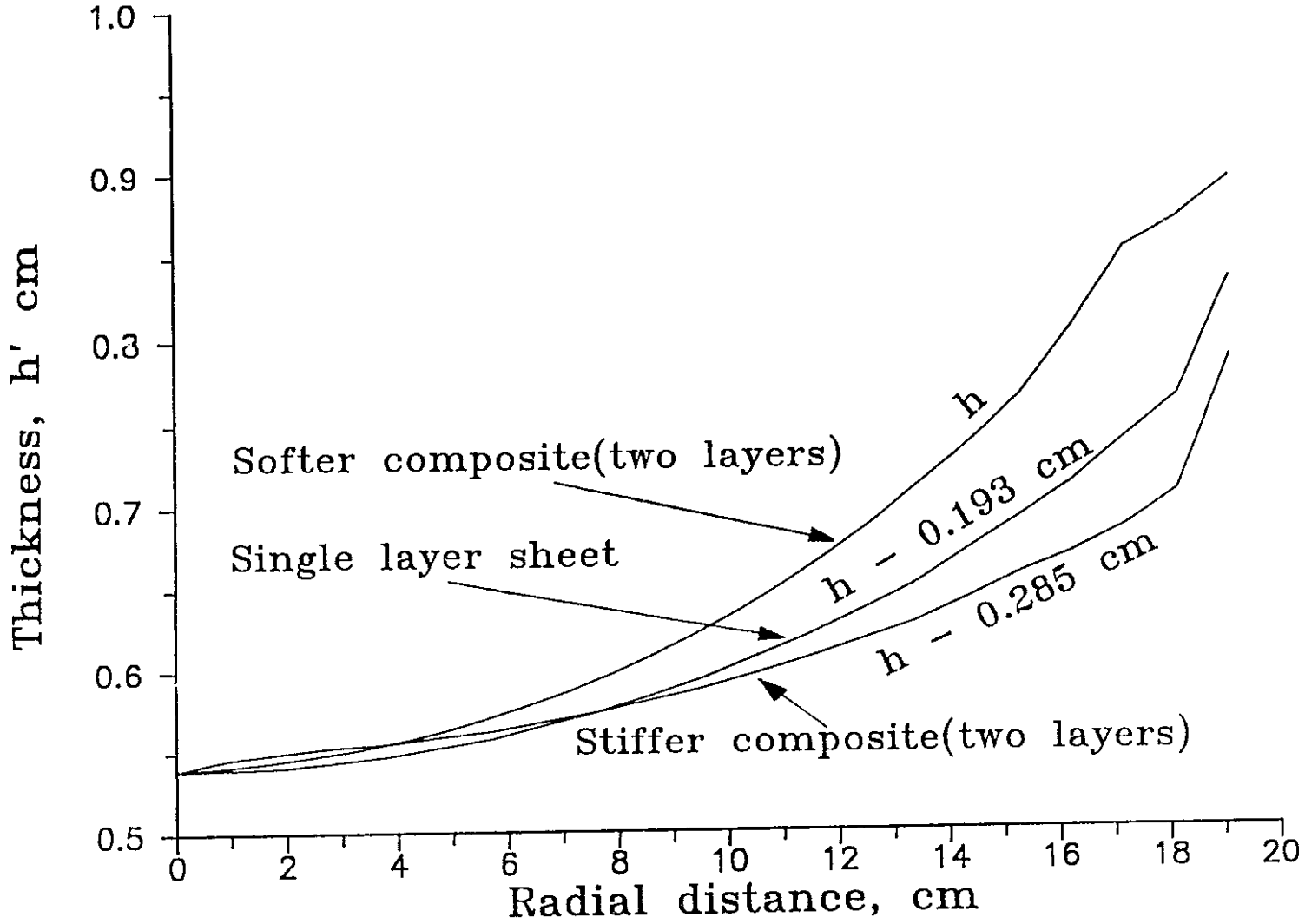

Figure 4.16 Thickness variation of different composites at the same pole height, u = 16.08 cm.

CHAPTER 5
SIMULATION OF FORMING WITH CONTACT

5.1 Introduction

An important characteristic in most forming processes is the existence of contact with friction. This problem has been dealt with numerically for more than two hundred years (e.g., by de Coulomb in 1779; by Hertz in 1881). But until the 1970s, contact problems which could be solved were limited to simple geometries and loading, such as pressing two ellipsoidal bodies together without friction, and indenting an elastic sphere onto a half space. Kalker reviewed theories of contact mechanics prior to 1974. Wilson and Parsons (1970), Chan and Tuba (1971), and Francavilla and Zienkiewicz (1975) used finite element methods to solve elastic contact problems. Kikuchi and Oden (1981), Yamada et al. (1979), Endo et al. (1984), Cheng and Kikuchi (1985), Rothert et al. (1985), Zhong (1989), and others applied the finite element method to solve finite deformation contact problems with elastic-plastic material laws and friction. A concise survey including both mathematical development and practical considerations was given in a treatise by Kikuchi and Oden (1988).

Contact condition, in the simplest way, can be expressed as no-penetration condition. As a result, displacement in the normal direction of contact surface is constrained by inequalities, as well as displacement and tractions in the tangential direction. Either the Lagrange multiplier method, or penalty method can be used in resolving constrained boundary conditions.

Finite element formulations for contact problems are usually based on variational inequalities. In calculation, violated boundary conditions are restored by constraining displacements in an iterative manner. At the end of each iteration, inequalities are checked and constraint equations are updated accordingly.

Friction between two sliding surfaces is a complicated phenomenon. Despite considerable work on this subject no sufficient answer on the physical nature of friction has been yet found (Suh and Sin, 1981). Oden and Martins (1985) provide an excellent survey of the theoretical and experimental study. The friction law presented by Coulomb in 1781 to solve engineering problems is still the major mathematical model used.

In thermoforming, blow molding, and compression forming, deformed polymer materials always contact with molds, from the beginning, or during the deformation process. In plug-assist forming, the plug makes contact with the material and is in motion through external force. Experimental observations reveal that in thermoforming and blow molding, polymer material usually sticks to mold upon contact, no slip occurs. Molds, which are usually made of metals, undergo no significant deformation as compared to deformed polymer materials. Therefore, it is reasonable to assume that the molds are rigid bodies.

Due to the above characteristics of polymer forming, only contact between a deformed body and a rigid body is considered, as shown in Figure 5.1. For simplicity, isothermal condition is also assumed.

Simple numerical algorithms designed to deal with frictional contact problem in polymer forming, as well as numerical examples, are presented in the following sections.

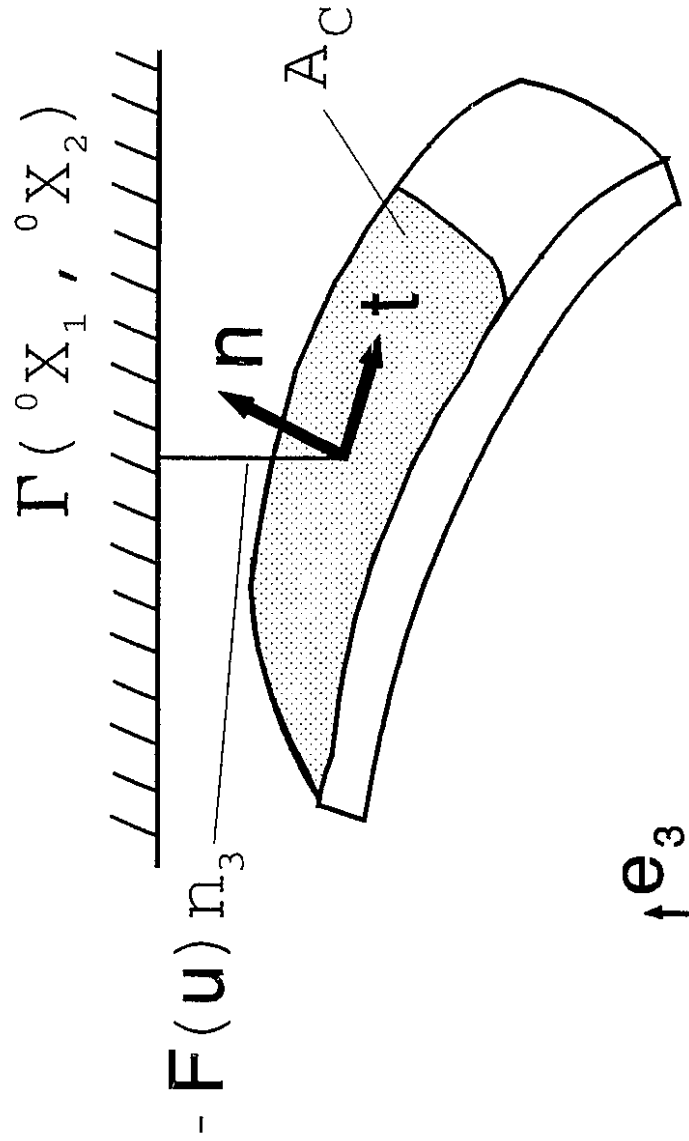

Figure 5.1 Contact geometry.

5.2 Numerical Implementation of Contact Boundary

5.2.1 Contact with Infinite Friction, or without Friction

These kinds of contact are idealized problems and can be treated easily as kinematic constraints in finite element formulation.

Suppose that the mold shape is described by a function,

$$ {}^0X_3 = \Gamma({}^0X_1, {}^0X_2) \tag{5.1} $$

and the mold is above the deformed polymer sheet. Contact condition is that the sheet can not penetrate the mold. The non-contact incremental finite element process should be continued on until an incremental step where some finite element nodes are detected over the mold Γ. If the overshoot of nodes is within a prescribed tolerance, for example, 10^{-4}, these overshot nodes are forcefully pulled back and will remain on the mold in the subsequent incremental steps. On the other hand, if the overshoot is too large, the step size is reduced and the process is repeated until the overshoot is within the tolerance. Otherwise, the subsequent steps may not converge to the equilibrium path due to a large change in stiffness properties of the system.

Suppose the equilibrium equation in finite element form is

$$ \mathbf{f}(\mathbf{x}, \mathbf{p}) = \mathbf{0} $$

where $\mathbf{x}$ is the unknown displacement vector. Assume some nodes have contacted with the mold at an instant, displacements of these nodes are $\mathbf{x}_2$ out of $\mathbf{x}$ and are equal to the coordinates of the mold at the contacted points minus the coordinates of these nodes in the reference state, i.e. $\mathbf{x}_2=\mathbf{a}$, $\mathbf{a}$ is a known vector upon contact. Therefore, $\mathbf{x} = \{\mathbf{x}_1, \mathbf{x}_2\}^T$, only $\mathbf{x}_1$ is unknown in the following steps. In both incremental loading and Newton-Raphson iteration processes, $\Delta\mathbf{x}_2 \equiv \mathbf{0}$, the nodal displacements corresponding to $\mathbf{x}_2$ are, therefore,

excluded from calculation, which reduces computing time.

In the case where frictionless slip is allowed, tangential displacements of contacted nodes are not held at all, only normal displacements are kept unchanged.

5.2.2 Contact with Finite Friction

In compression forming, finite slip is observed, as well as in squeezing flow, which is used to study the rheological behavior of polymers. Coulomb's law is used in the finite element formulation as there is no better physical model available to explain the friction phenomenon between material interfaces.

In Figure 5.1, the contact area is denoted by A_C in the current configuration, and is defined by a particle which has

$$ {}^0X_3 = \Phi({}^0X_1, {}^0X_2) \tag{5.2} $$

where Φ is assumed to be a smooth function. The mold is defined by eq.(5.1). Then, if $({}^0X_1, {}^0X_2, {}^0X_3)$ is a particle on A_C, its displacement must satisfy

$$ u_i({}^0X_1, {}^0X_2, {}^0X_3) = {}^1x_i({}^0X_1, {}^0X_2, \Phi({}^0X_1, {}^0X_2)) - {}^0X_i, \; i=1, 2, 3 \tag{5.3} $$

and the non-penetration condition is

$$ \Phi({}^0X_1, {}^0X_2) + u_3({}^0X_1, {}^0X_2, \Phi({}^0X_1, {}^0X_2)) \le \Gamma({}^0X_1, {}^0X_2), \tag{5.4} $$

or

$$ F(\mathbf{u}) = \Phi({}^0X_1, {}^0X_2) + u_3({}^0X_1, {}^0X_2, \Phi({}^0X_1, {}^0X_2)) - \Gamma({}^0X_1, {}^0X_2) \le 0 \tag{5.5} $$

We refer to the inequality (5.5) as the kinematical contact condition for finite displacements of a body constrained by a fixed rigid mold.

Upon contact, the body will be subjected to compressive stress $\sigma_N \le 0$.

Another form of contact condition is

$$F(\mathbf{u})\ \sigma_N = 0 \qquad \text{on } A_C \tag{5.6}$$

when no contact occurs, $F(\mathbf{u}) < 0$ and $\sigma_N = 0$, while contacting, $F(\mathbf{u}) = 0$, and $\sigma_N < 0$. Assume that normal and tangential directions of the mold at point $({}^0X_1, {}^0X_2, \Gamma)$ are $\mathbf{n}$ and $\mathbf{t}$, then the distance of a material point $({}^0X_1, {}^0X_2, \Phi)$ of the body to the mold is approximately equal to $F_N = F(\mathbf{u})\ n_3$ when the point is very close to the mold. When the mold is horizontal, $n_3 = 1$, $F_N = F$.

The rigid mold can be approximated by continuously distributed normal compressive springs. Stiffness of these springs is very large and given by $1/\varepsilon$, for sufficiently small $\varepsilon > 0$. If $\varepsilon \to 0$, the elastic mold becomes rigid. The normal stress σ_N can thus be approximated by

$$\sigma_N = -\frac{1}{\varepsilon}\,[F_N]^+ \tag{5.7}$$

where $[F_N]^+$ is

$$[F_N]^+ = \max\ \{F_N, 0\} \tag{5.8}$$

This approximation is the penalty method.

According to Coulomb's law, friction stress along the tangential direction $\mathbf{t}$ is proportional to normal stress, i.e.

$$\sigma_T = -\mu\ \sigma_N \tag{5.9}$$

where μ is the coefficient of friction and the negative sign indicates that friction is opposite to the relative tangential motion, or motion trend. With different μ, both sticking and slipping can be taken into account.

Decompose a virtual velocity vector δv of the body into normal and tangential components with respect to the mold, we have

$$\delta v_N = \delta v \cdot \mathbf{n} \text{ and } \delta v_T = \delta v \cdot \mathbf{t} \tag{5.10}$$

Then, the virtual work done by the contact forces are

$$\delta W_C = \int_{A_C} (\sigma_N \delta v_N + \sigma_T \delta v_T)\, dA \tag{5.11}$$

Substitute (5.7) and (5.9) into (5.11), we obtain

$$\delta W_C = \int_{A_C} \frac{1}{\varepsilon} (-[F_N]^+ \delta v_N + \mu [F_N]^+ \delta v_T)\, dA \tag{5.12}$$

By adding this contact contribution to the virtual work balance eq.(3.1.7), we construct a finite element formulation with contact and friction.

Yet, the stiffness matrix contributed from contact can not be evaluated from (5.12) directly with $[F_N]^+$ defined in (5.8), since function $[F_N]^+$ is not differentiable at $F_N = 0$.

To overcome this difficulty, we replace $[F_N]^+$ by a regularized constraint function F_N^θ that can be made arbitrarily close to $[F_N]^+$ by choosing the real parameter $\theta > 0$ sufficiently small. The F_N^θ chosen here is

$$F_N^\theta = \begin{cases} [F_N]^+ & \text{for } |F_N| \geq \theta \\ \dfrac{1}{4\theta} F_N^2 + \dfrac{1}{2} F_N + \dfrac{\theta}{4} & \text{for } |F_N| < \theta \end{cases} \tag{5.13}$$

Then an additional loading due to contact forces,

$$p_{CM}^\nu = \frac{1}{\varepsilon} \int_{A_C} F_N^\theta \Psi_M (-n_\nu + \mu\, t_\nu)\, dA \tag{5.14}$$

should be added to the right-hand side of eq.(3.1.13). A new stiffness matrix should also be added into the incremental stiffness matrix (3.1.20),

$$(K_{INC})_{ij}^C = - \frac{\partial p_{Ci}}{\partial u_j} \tag{5.15}$$

5.3 Numerical Examples

5.3.1 Forming of Circular Part

Pressure forming a sheet into a shallow mold is studied first, as shown in Figure 5.2. No slip between mold and sheet is assumed. Figure 5.3 shows the gradual change of thickness variation during the forming. We can see that before contact, thickness at the pole becomes smallest. The pole contacts the mold first, and its thickness does not change afterwards. As contact develops from pole to corner, the thinner corner gradually forms. Figure 5.4 shows a three-dimensional shape of a formed part. In the case of a deep mold, the gradually changing profiles are shown in Figure 5.5. Thinner bottom and corner are also formed, even though the development of contact is different from that of shallow mold, see Figure 5.6. Mooney model is used there with C_{01}=50 psi and C_{10}= 15 psi.

A convergence study is performed for the contact problem, see Figure 5.7. Before contact, three different relative errors reduce quadratically during Newton-Raphson iterations. When a node establishes contact, the boundary conditions of the whole system change. Relative errors increase in the first two iterations after contact. As iterations continue near quadratical convergence is achieved again. After four more iterations, the relative errors of $\|\Delta x\|_2/\|x\|_2$ are within the prescribed tolerance 10^{-7}.

5.3.2 Other Applications

With little modification, the finite element program can simulate forming of large rectangular parts in plane strain deformation state. We know that if one dimension of a sheet is much larger than the other two dimensions and pressure loading is mainly in a plane which is perpendicular to this

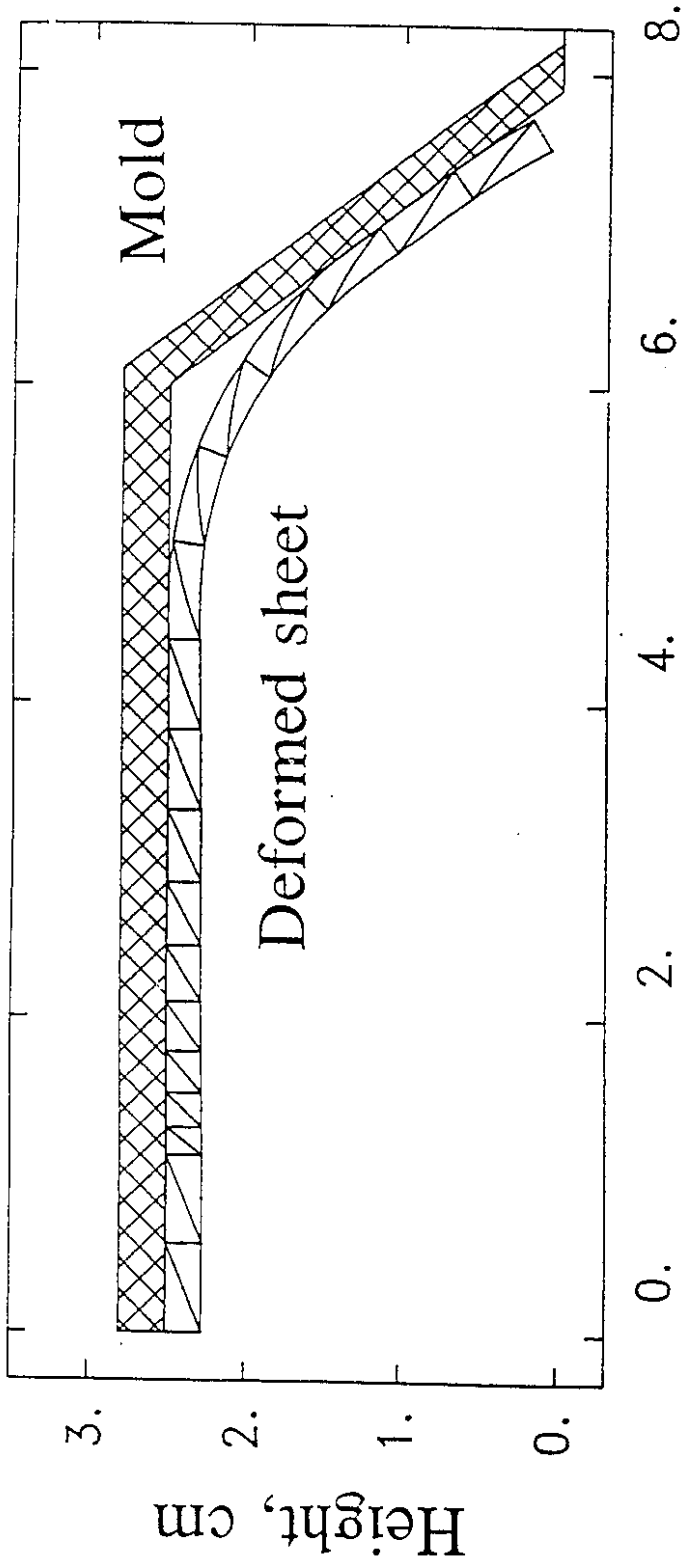

Figure 5.2 Deformed sheet in contact with a mold.

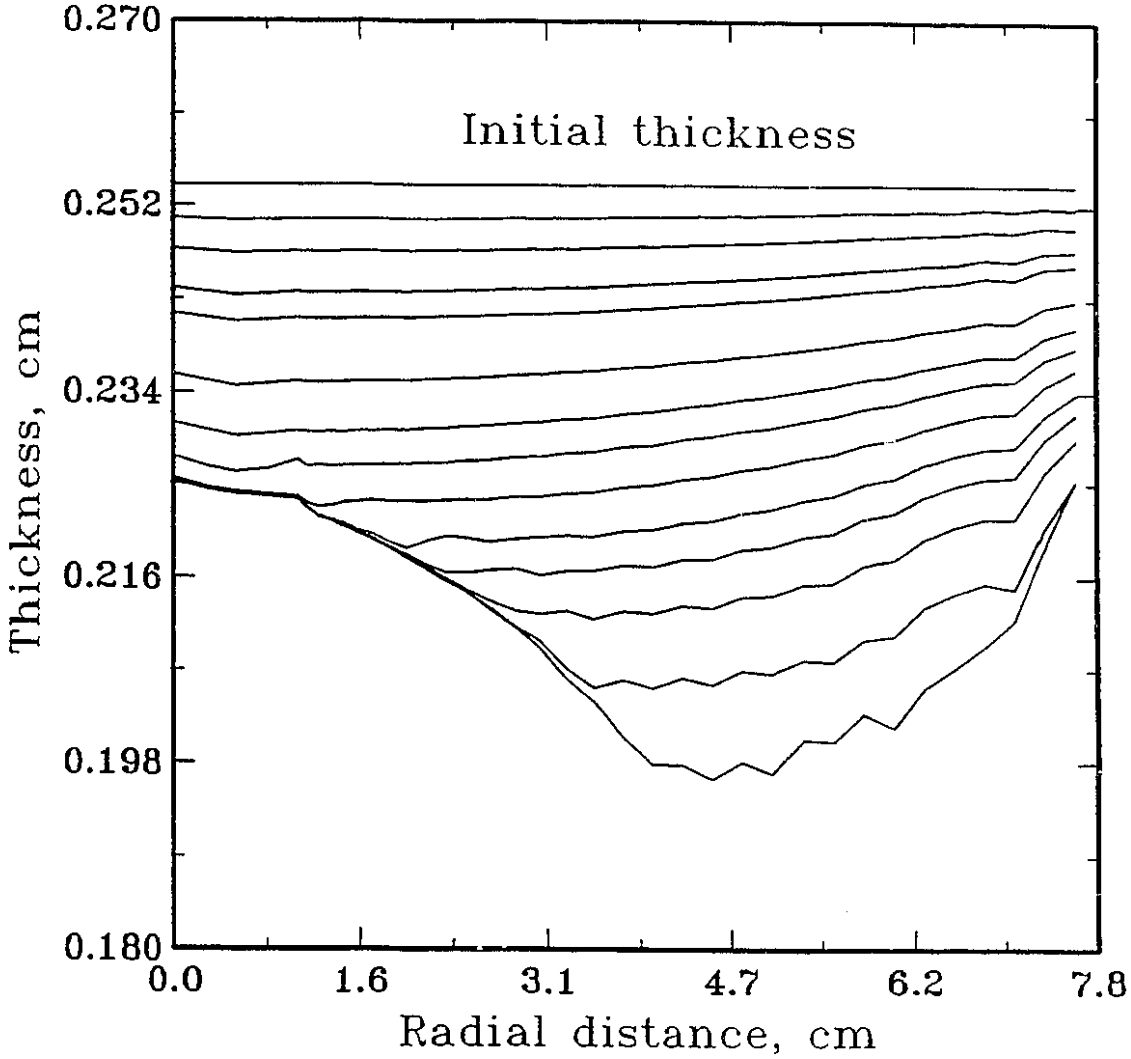

Figure 5.3 Thickness variations during forming (contact starts at centre).

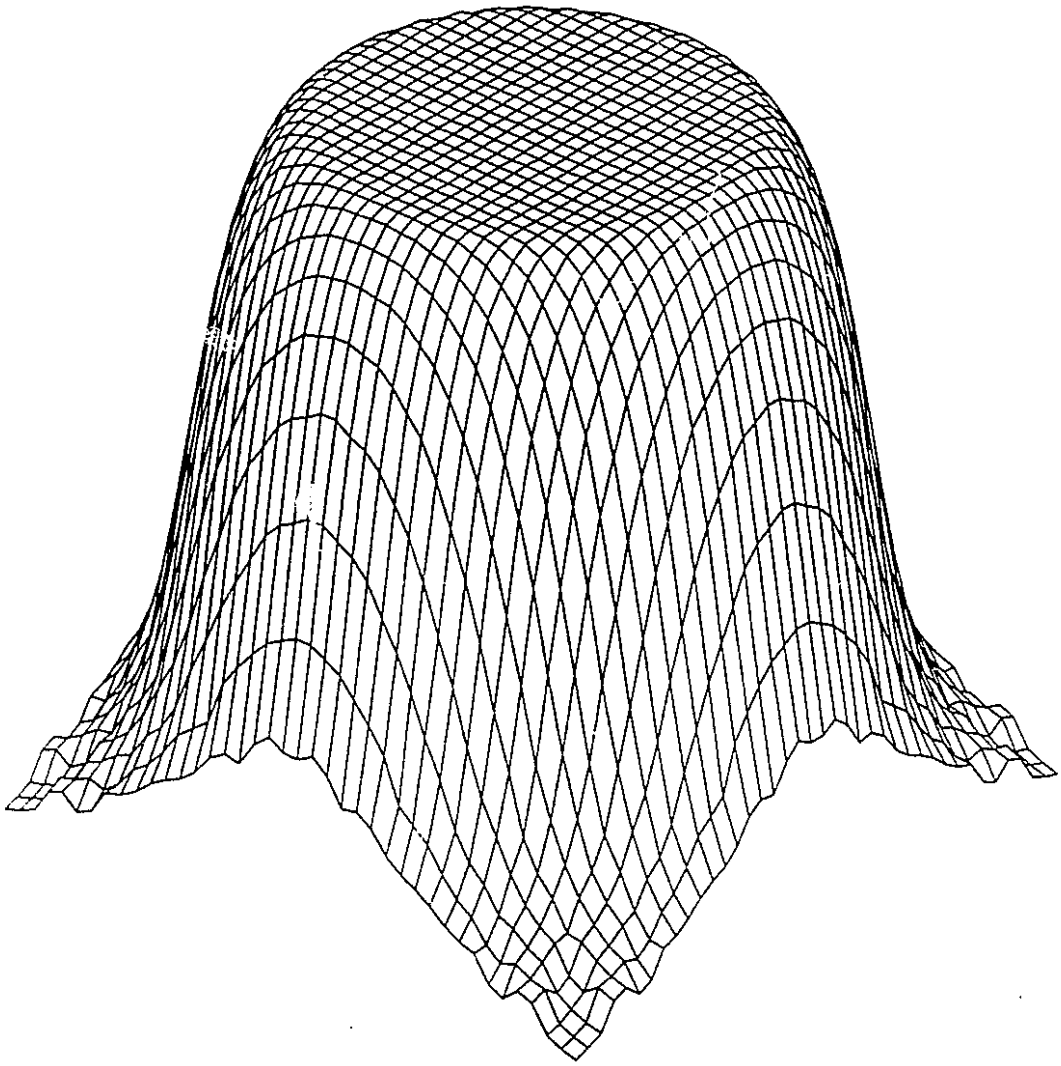

Figure 5.4 Three-dimensional view of a formed cup.

(Note: The wrinkling at boundary, or drawing-in from clamped end, is due to the three dimensional graphics software. The simulation is carried out with clamped end.)

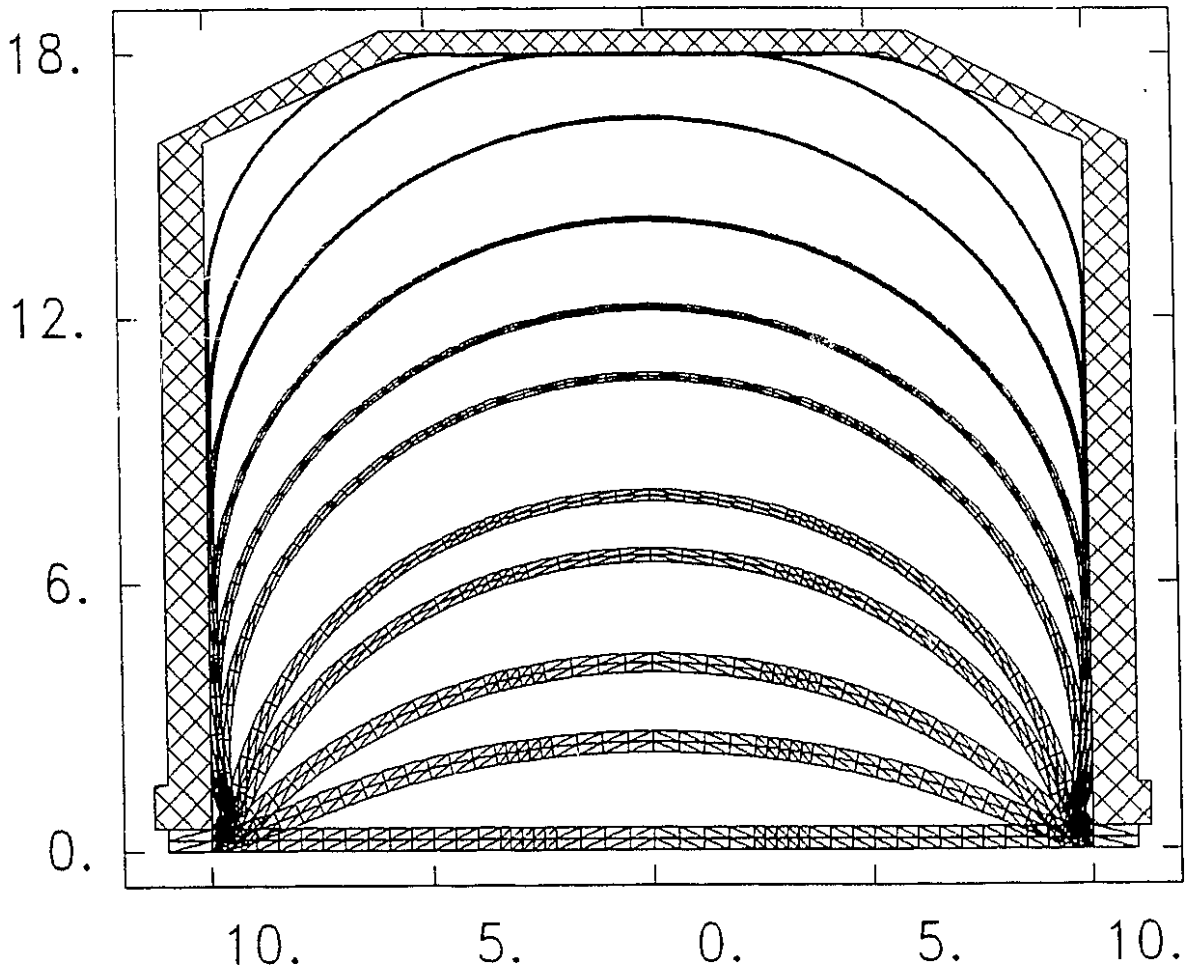

Figure 5.5 Vacuum forming a deep cup.

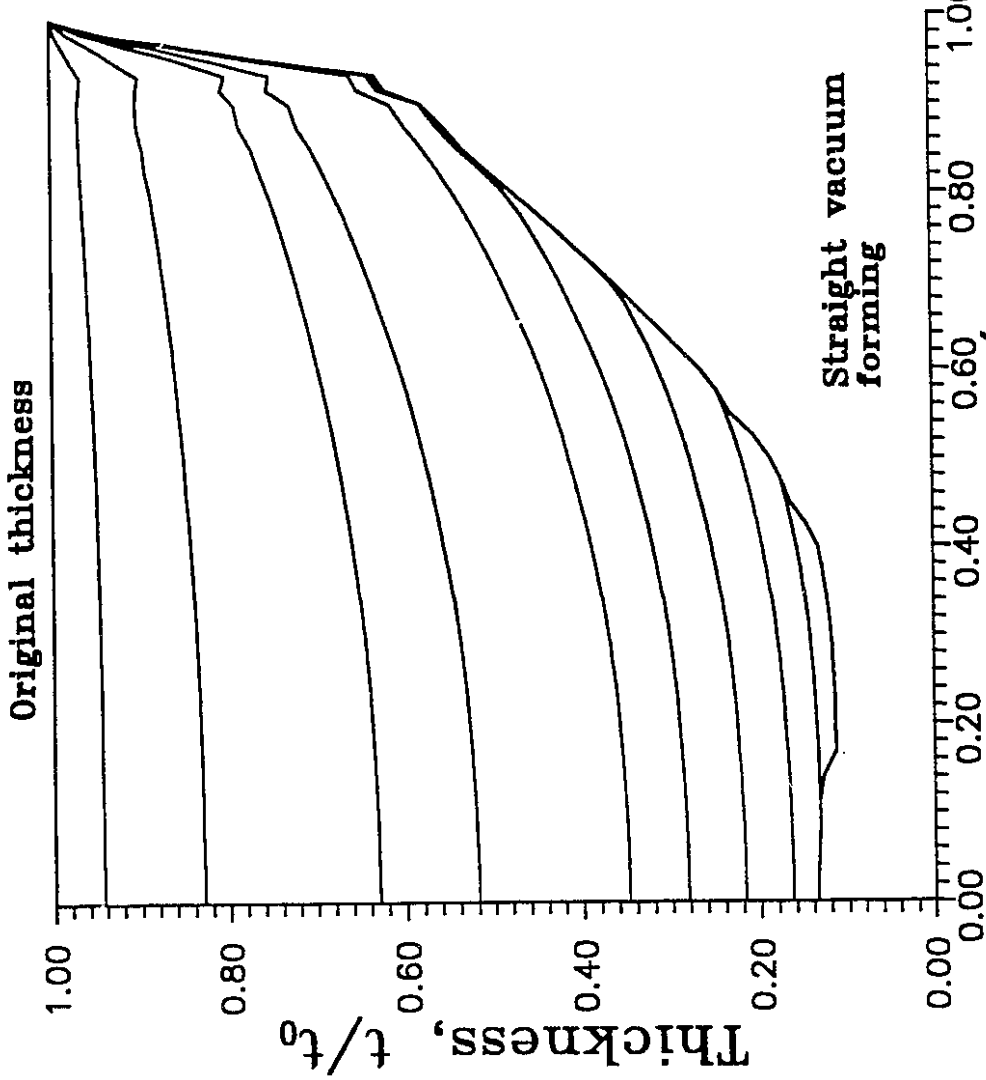

Figure 5.6 Thickness variations during forming (contact starts at rim).

dimension, then there is no strain along this dimension, and the deformation is called plane strain. Figure 5.8 shows the original dimensions of a sheet and the corresponding formed part, where $L \gg W$, and $L \gg h$. Along z direction, away from boundaries ($z = 0$, and $z = L$) the deformation is approximately plane strain. In the finite element program, it is only needed to assume that $r = \infty$, and $\lambda_{33} = 1 + \frac{u_r}{r} = 1$, then the program can be used to describe plane strain deformation. Figure 5.9 gives both a two-dimensional profile and a three-dimensional shape of a formed rectangular part. All the other calculations are similar to those of axisymmetrical sheet.

The current program can simulate blow molding as well, which is mathematically the same problem as thermoforming, even though the practical processing operations are different. Blow molding is to blow a parison into a mold by using internal pressure. This processing is used to fabricate soft drink bottles, and containers, such as automobile gas tanks. Mathematically, the differences between thermoforming and blow molding are geometrical ones. The initial part of the latter is a bottle-like parison, while the former is a flat sheet. The mold used in the latter case is also bottle-like, and the mold of thermoforming can be of any shape. Numerical siumlations of blow molding have been conducted with elastic-viscoplastic modeling (Chung, 1989), nonlinear elastic modeling (deLorenzi and Nied, 1991, and Kouba et al. 1993), and with Newtonian fluid modeling (Schmidt et al. 1992).

Above simulation are conducted with isothermal process assumption. Recently, effects of temperature on finished product have drawn considerable attension (deLorenzi and Nied, 1991, Poller and Michaeli, 1992, and Menezes and Watt, 1992). The current finite element program is extended to take into account non-isothermal effects (Song and Meguid, 1993).

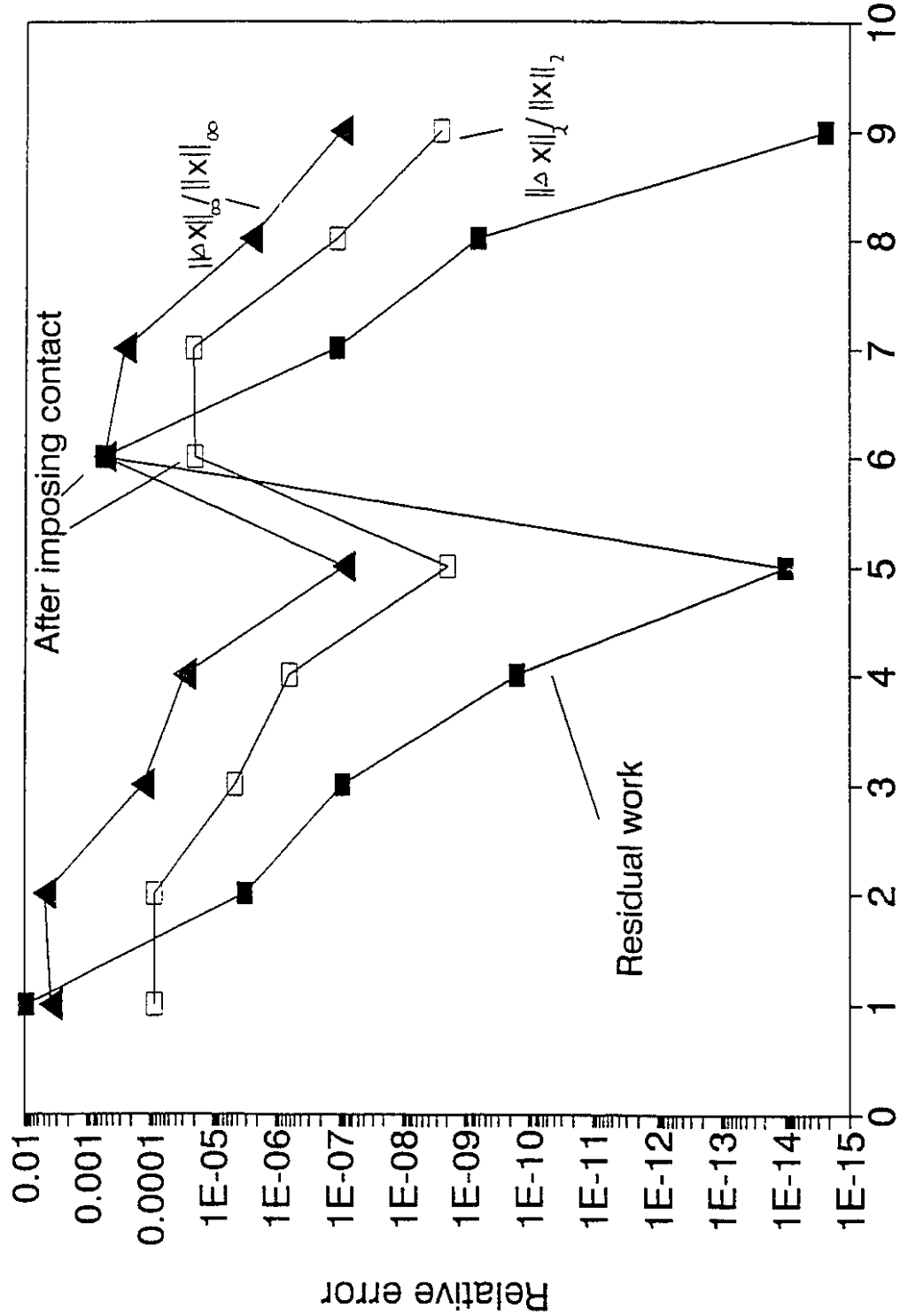

Figure 5.7 Convergence study when contact presented.

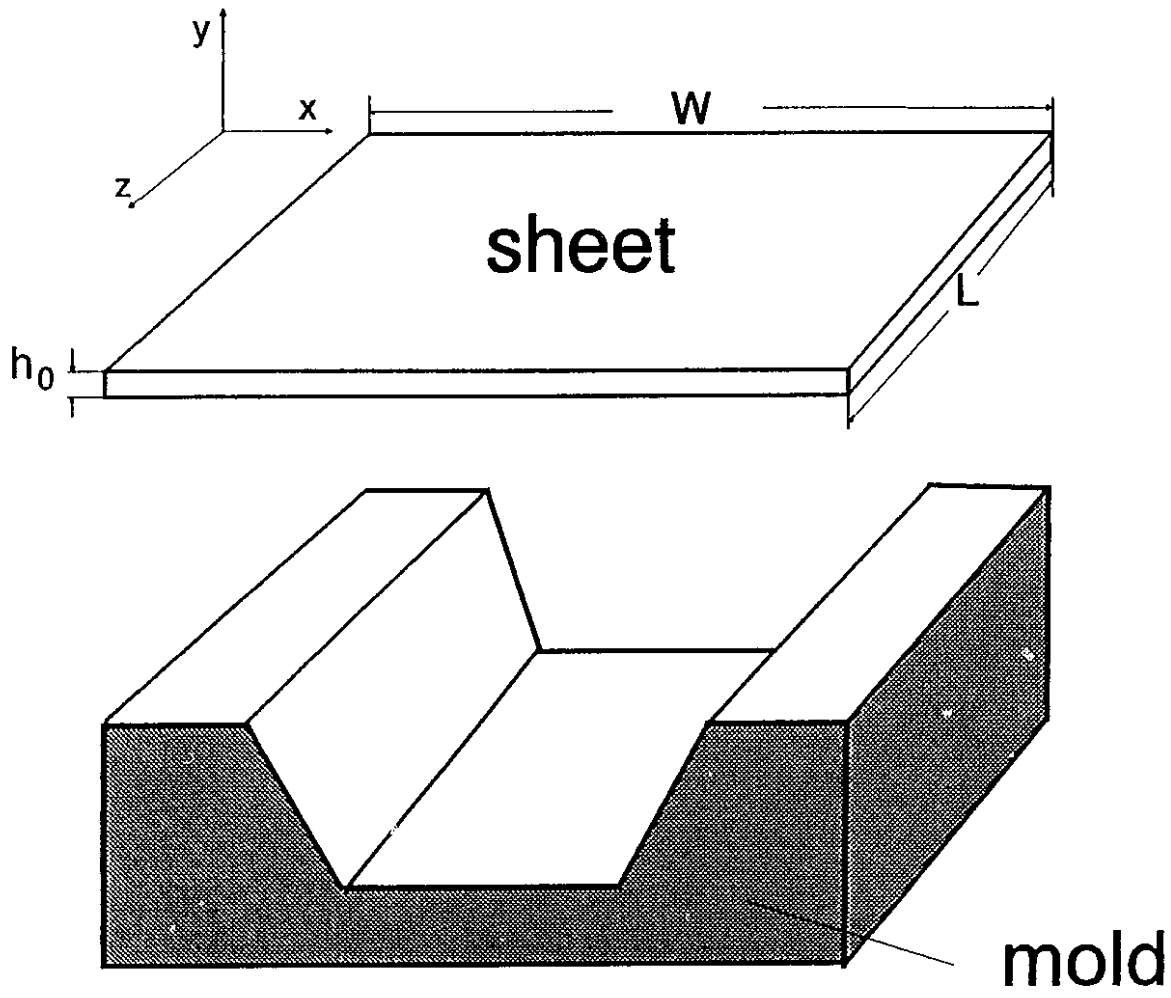

Figure 5.8 A sketch of forming of a rectangular part.

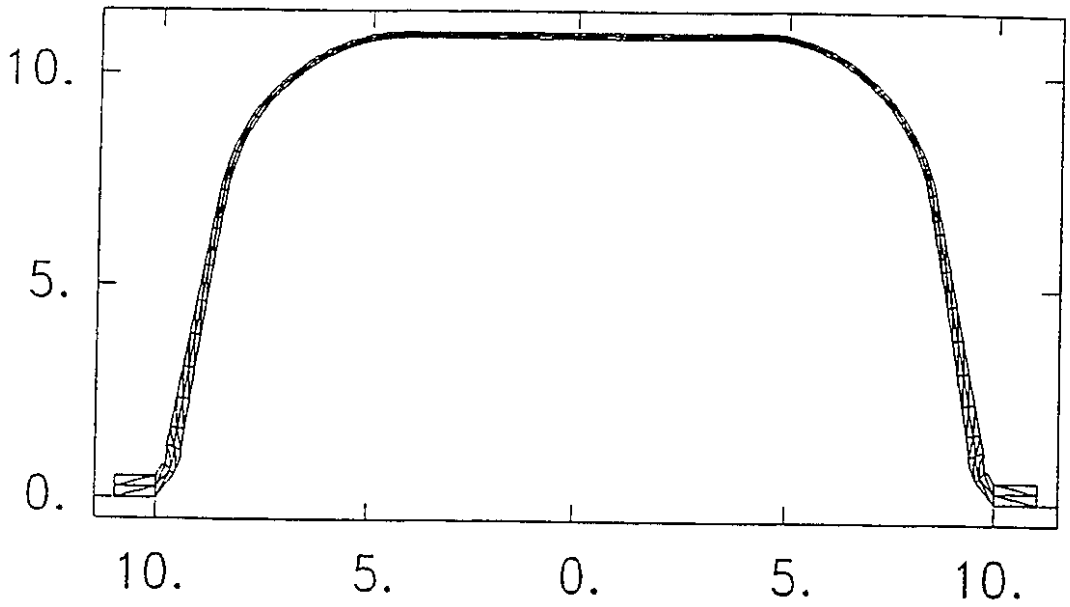

(a) 2-D view,

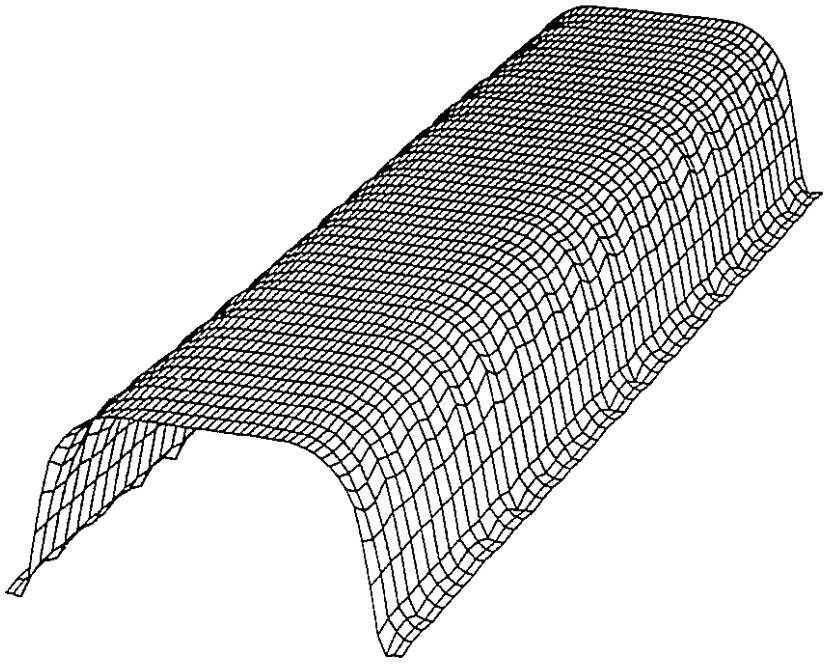

(b) 3-D view.

Figure 5.9 The formed rectangular part.

(Note: The wrinkling at boundary, or drawing-in from clamped end, is due to the three dimensional graphics software. The simulation is carried out with clamped end.)

5.4 Concluding Remarks

Finite element formulations of contact with finite friction are established. Then, simulations of polymer forming with contact are successfully carried out. The thickness variation characteristics in practical forming situation are captured numerically. Small incremental steps are used upon contact to avoid a large change in stiffness matrices and divergence. The convergence of the contact formulation remains quadratic. More numerical simulations are given in later chapters.

CHAPTER 6
FINITE ELEMENT SIMULATION OF PLUG-ASSIST FORMING

6.1 Introduction

Plug-assist forming is the process of stretching a heated thermoplastic sheet into a cavity by use of a plug. This pre-stretching process is used to promote uniformity of wall thickness distribution, allowing the formed part to have better structural properties, such as larger flexural strength. Straight vacuum, or pressure forming may produce undesirable thinner corners (Frados, 1976). Usually, plug-assist forming proceeds until a sheet is stretched up to about 80% of cavity depth with a plug that is up to 80% of the cavity diameter. When the plug completes its stroke, the cavity is sealed, and either vacuum is drawn, or air pressure is applied until the sheet fills the cavity (Throne, 1989).

Since sheet thickness variation, which is a function of processing conditions and rheological properties of a softened plastic sheet, can not be controlled during processing, several parameters, such as plug size, distance travelled by plug, bubble size, and temperature, are determined by trial-and-error. Although industrial thermoforming of plastics has been established for several decades, few theoretical and numerical investigations have been implemented. From a point of view of practical forming, accurate prediction of wall thickness distribution, the relation between applied force on a plug and sheet deflection, and locations of maximum strain and stress are

significant factors in process optimization.

Williams (1970) and Throne (1989, 1990) developed analytical models of plug-assist forming with use of the thin membrane approximation and incompressibility. Williams also conducted tests with sheets of PMMA at forming temperature of 160 $^{\circ}$C. Throne experimented with natural rubber at room temperature.

Williams' analysis, called large strain theory by Throne, assumes that the problem is biaxial stretching of a membrane, where the material behaves as neo-Hookean, and higher order terms of extension ratio λ^{-2} are negligible. Simple formulas were obtained for plug-assist forming by flat and by spherical plugs (1964, 1970), as well as formulas for vacuum forming and shaping of a plastic sheet into a cone. These formulas are in good agreement with Williams' experiments with respect to deformed profiles, and moderate agreement with respect to thickness distributions. Large deviations appear between predicted and measured force-deflection curves. With corrections and semi-empirical modifications, agreement is improved.

Throne (1989, 1990) carried out his simulations with a two-constant Mooney model and with higher order terms of λ^{-2}. Based on experimental observations, he assumed that plug-assist forming always resulted in plane strain deformation. He conducted experiments with two kinds of sheets, one was 0.01 in thick, the other, 0.03 in. His numerical results of force-deflection curves compare well with experimental data for the 0.01 in thick rubber sheet. Generally, Throne's analysis presents better predictions than Williams' large strain solution.

Other simulations of plug-assist forming as reported by Menges and Weinand (1988), and Esteghamatian et al. (1989) used the Ogden model.

Predictions, however, are not much improved over previous results and suggest that a reexamination of the whole modeling approach is necessary. Literature reviews on the inflation process in thermoforming and blow molding are found elsewhere (deLorenzi and Nied, 1991, Song et al. 1991 (a)) and the most recent results in conference proceedings (Terada and Yamabe, 1991, and Garcia-Rejon et al. 1991). Finite element simulation of deep-drawing of thin metal sheet, a similar process to plug-assist forming of plastics, can be found in Wennerstorm et al. (1984) and Massoni and Chenot (1992).

The non-linear finite element model for analysis of thermoforming of plastics has been revised to describe the plug-assist forming process. Numerical simulations agree well with experimental data for the plug-assist forming of PMMA and of natural rubber (Song et al. 1991 (b), 1992). The processing characteristics, such as the deformed profile, and thickness variation, are obtained with high accuracy. A complete stress analysis is also performed. Thus, strain and stress distributions near corners and plug edges are determined. These are important for damage analysis and forming of composites.

In this investigation, the plug-assist forming is simulated first, then combined plug-assist pre-stretching and vacuum forming is studied numerically. However, if a purely elastic model is used, the final formed part may contract back to a new equilibrium configuration upon removing the loading. The real situation is that after removing the loading, the formed part will keep its shape, i.e. permanent deformation takes place, although slight springback displacement may occur. This suggests that an elastic-viscoplastic constitutive model should be used to take these effects into account, as is the common practice in metal forming (Ghosh, 1989).

Unfortunately, no such model is available for general polymer forming, which incorporates nonlinear elastic and viscoplastic responses. Recently, methodology for metal forming has been directly applied for polymers by using constitutive equations and finite element program for metals (Lee et al. 1991).

6.2 Modeling of Process

Suitable for vacuum and pressure forming processes, the incremental finite element technique to simulate thermoforming can be called "load driving" solving process, i.e., knowing external loading distribution, to find displacement field as described in Chapter 3 and 4. In plug-assist forming with only total force on plug known and loading distribution unknown, a "displacement driving" procedure is needed.

Suppose the sheet is subjected to a moving kinematic constraint, instead of distributed loading. A moving plug, within time Δt, travels Δw upward in vertical direction, then the incremental equilibrium equation (3.1.15) is:

$$\begin{bmatrix} [K_{11}] & [K_{12}] \\ [K_{21}] & [K_{22}] \end{bmatrix} \cdot \begin{Bmatrix} \Delta \mathbf{u}_1 \\ \Delta \mathbf{u}_2 \end{Bmatrix} = \begin{Bmatrix} \mathbf{0} \\ \mathbf{0} \end{Bmatrix} \tag{6.1}$$

and the kinematic constraint is

$$\{ \Delta \mathbf{u}_2 \} = \Delta w \, \mathbf{I}_2, \quad \mathbf{I}_2 = \{ 1, 1, \ldots, 1 \}^T \tag{6.2}$$

where $\{\Delta \mathbf{u}_2\}$ is the incremental vector of vertical displacements of those nodes in contact with the plug. Then equation (6.1) can be changed into

$$\begin{bmatrix} [K_{11}] & [0] \\ [0] & [I] \end{bmatrix} \cdot \begin{Bmatrix} \Delta \mathbf{u}_1 \\ \Delta \mathbf{u}_2 \end{Bmatrix} = \begin{bmatrix} -[K_{12}] \\ [I] \end{bmatrix} \cdot \Delta w \, \mathbf{I}_2 \tag{6.3}$$

without constraint, where [I] is an identity matrix.

After each incremental loading step, Newton-Raphson iterations are performed to correct the predicted displacement vector until a predetermined tolerance is satisfied. In Newton-Raphson iteration, $\Delta \mathbf{u}_2 = \mathbf{0}$, we have,

$$\begin{bmatrix} [K_{11}] & [0] \\ [0] & [I] \end{bmatrix} \cdot \begin{Bmatrix} \Delta \mathbf{u}_1 \\ \Delta \mathbf{u}_2 \end{Bmatrix} = \begin{Bmatrix} -\{f_1\} \\ \{\mathbf{0}\} \end{Bmatrix} \tag{6.4}$$

where $\{f_1\}$ is the residual vector defined in eq.(3.1.15).

After the displacement field is obtained, stress distributions can be calculated by a proper stress calculation algorithm, as well as total force on the plug.

6.3 Comparison of Numerical Results with Williams' Experiments

In the finite element program, six-node isoparametric triangular elements are used. Only one layer of finite elements is used through the sheet thickness, since similar results have been obtained with two or more layers of elements (Song et al. 1991 (a), 1992).

A comparative study is made between our simulation and Williams' (1970) experiments for PMMA. The initial radius is $r_0 = 8.89$ cm, initial thickness is $_0 = 0.6985$ cm and plug radius is $r_p = 1.905$ cm. Mooney parameters measured by Williams are C_{10}=65.0 psi (0.448 MPa) and $C_{01} = 0.0$. Forty elements are used in the simulation. Figure 6.1 shows the deformed profiles, with outer perimeter assumed clamped. In Figure 6.1 (a), the sheet is allowed to slip from the plug during forming, while the sheet sticks in the example shown in Figure 6.1 (b). Plug force vs. deflection is illustrated in Figure 6.2. At large deflection, the experimental data seem to approach the curve with perfect slip, which suggests that inclusion of finite friction slip may

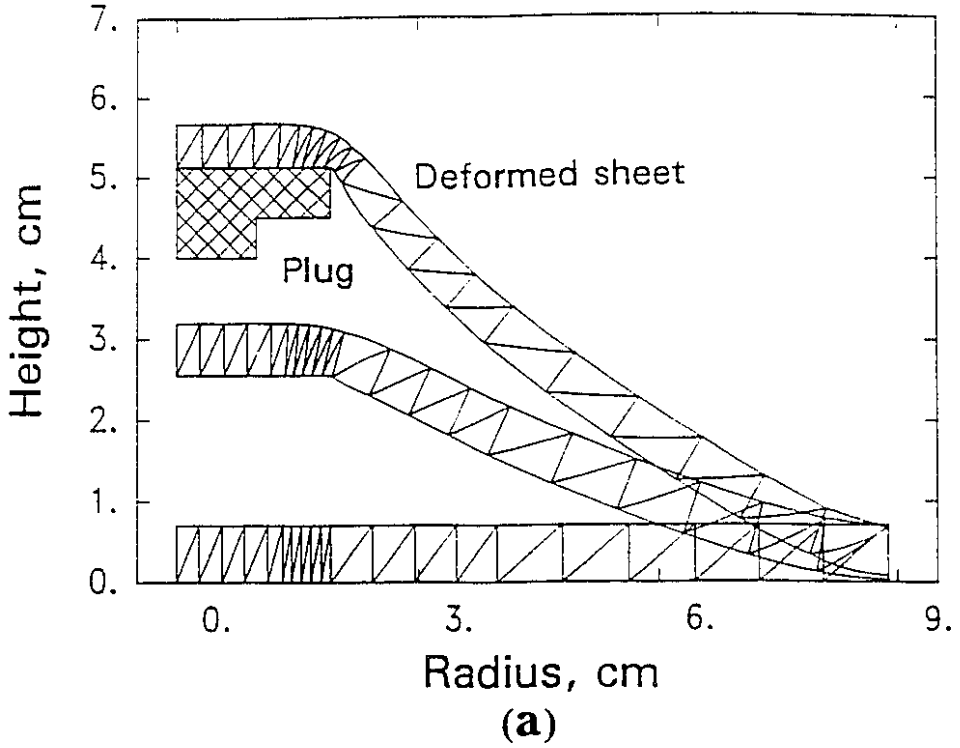

(a)

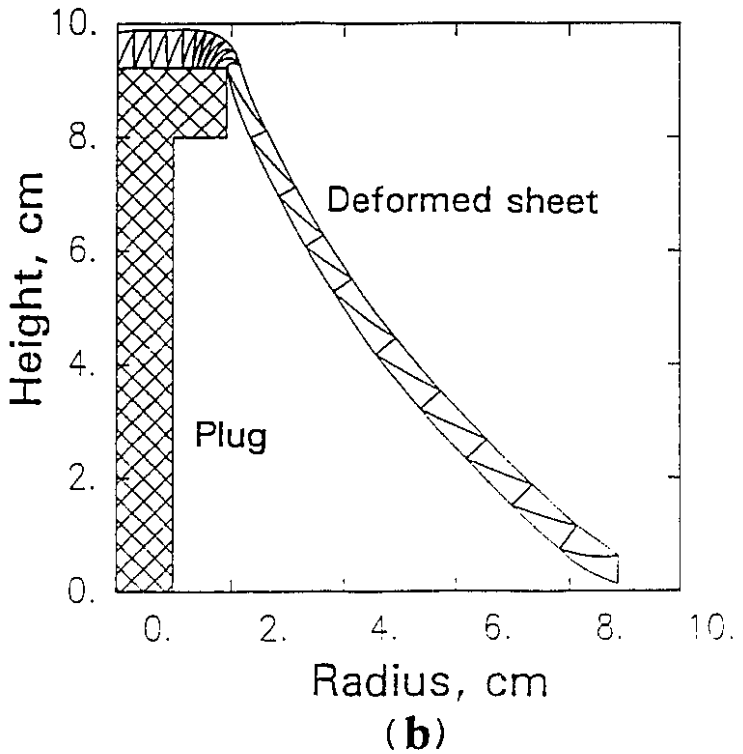

(b)

Figure 6.1 Calculated deformed profiles of plug-assist forming.
(a) Perfect (frictionless) slip (b) No slip

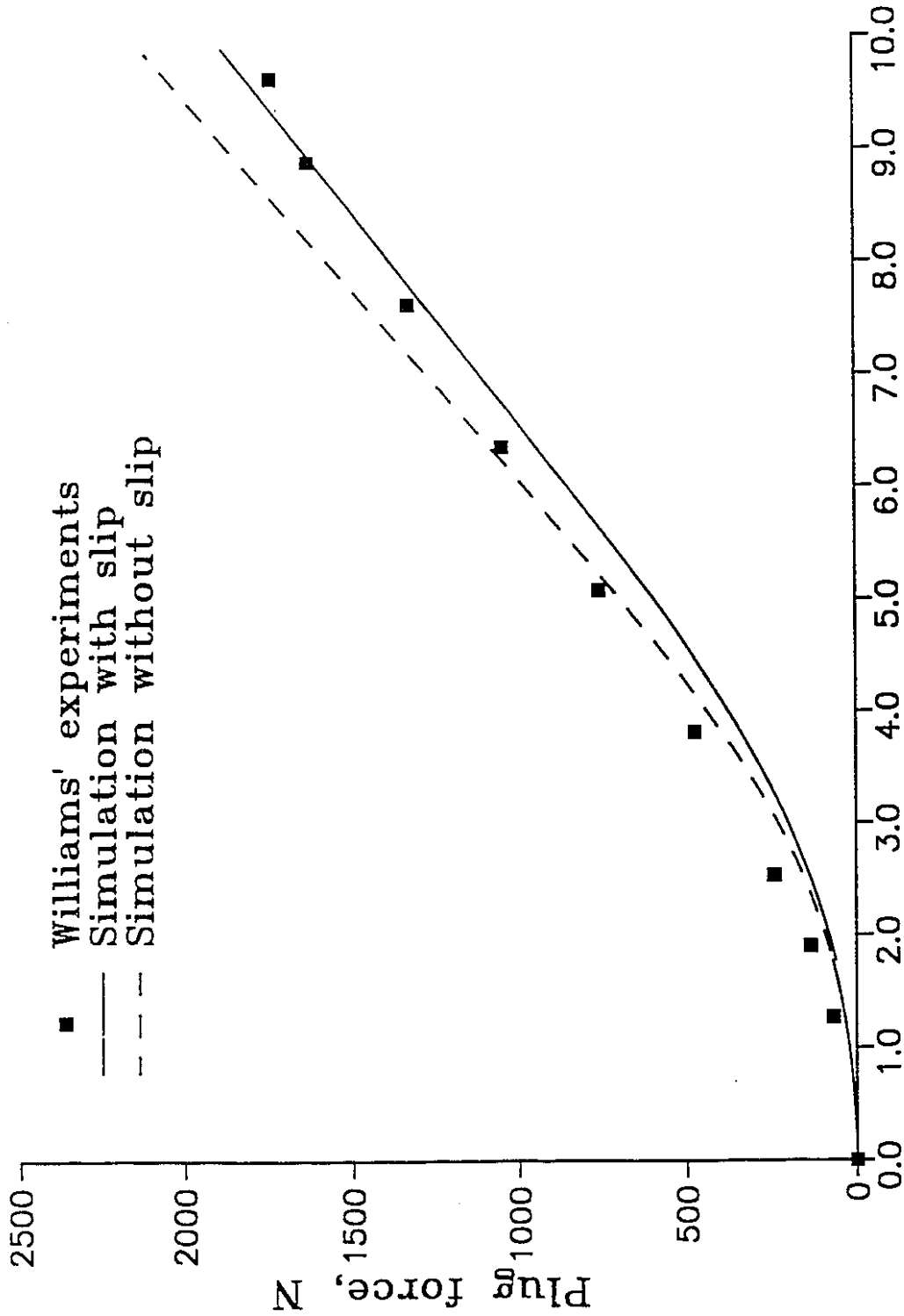

Figure 6.2 A comparison with Williams' experimental data of PMMA.

improve the overall agreement between the present simulation and Williams' results. However, no information is available on how fast the polymer slips on surface and only two extremes are examined, i.e. no slip or perfect slip.

One advantage of our simulation is that thickness variation over the plug can be obtained directly. Figure 6.3 shows simulations of thickness distributions with, and without slip, which are in good agreement with Williams' data. Williams reported in his measurements that a reduction in thickness on the flat top has a value of t/t_0= 0.51. In our simulation with slip, the values of t/t_0 on the flat top range from 0.3 to 0.7 (Figure 6.3). It is impossible to obtain thickness distribution over the plug top with the analyses of Williams and Throne. In the present study, thinning due to shear near the plug edge is considered. Strain state transits from equibiaxial extension at the pole (when there is slip) to plane strain state away from the plug as shown in Figure 6.4 by the curves of three principal extension ratios on the top face of the sheet. Corresponding Lagrange strains are shown in Figure 6.5. These two figures reveal that in the immediate vicinity of the pole, there is equibiaxial stretching, since $\lambda_1(=\lambda_r) = \lambda_3 = 1.25$. Near the edge, this is no longer true, λ_1 increases sharply, λ_3 decreases and there exists shear strain, which can be understood easily by looking at the deformed elements in Figure 6.1. Away from the plug, circumferential extension ratio $\lambda_3 = \lambda_\theta$ (= r/R) is approximately equal to 1.0 (Figure 6.4), and the sheet is subjected to plane strain. Material points are deflected upward from their original positions and average deviation of λ_3 is about 6.2 % away from 1.0 outside the plug.

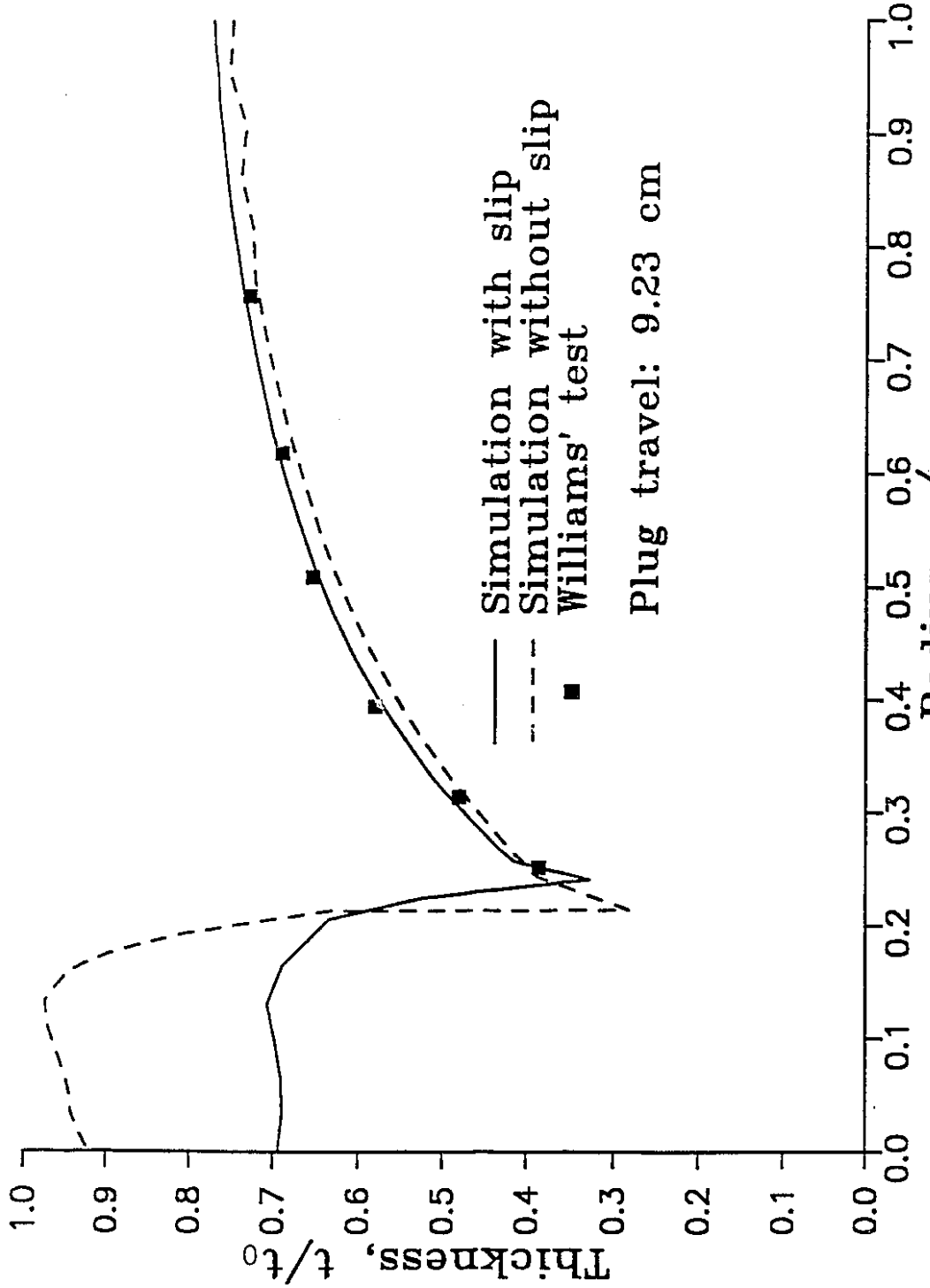

Figure 6.3 Thickness variations of deformed sheet.

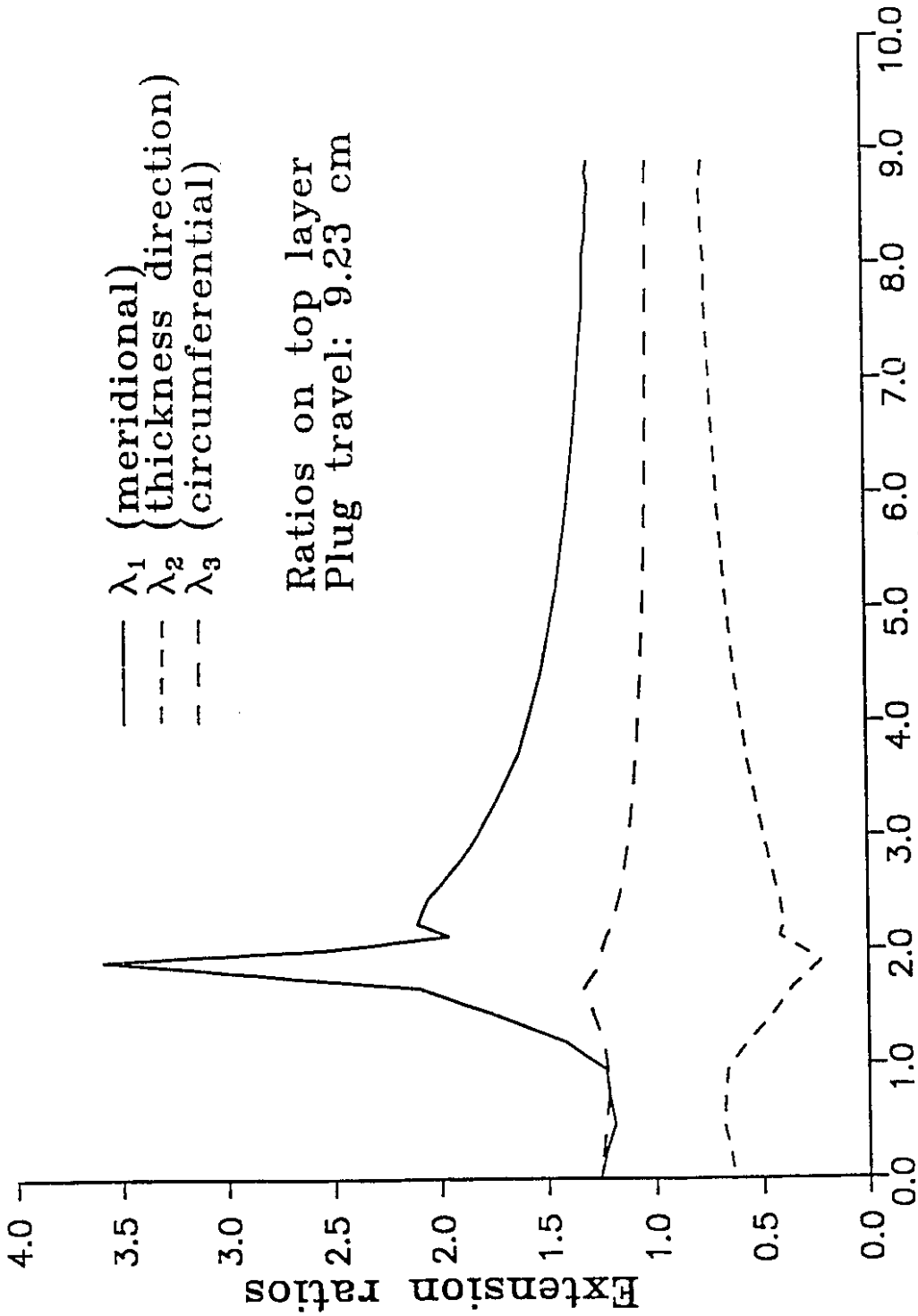

Figure 6.4 Principal extension ratios (slip at plug surface).

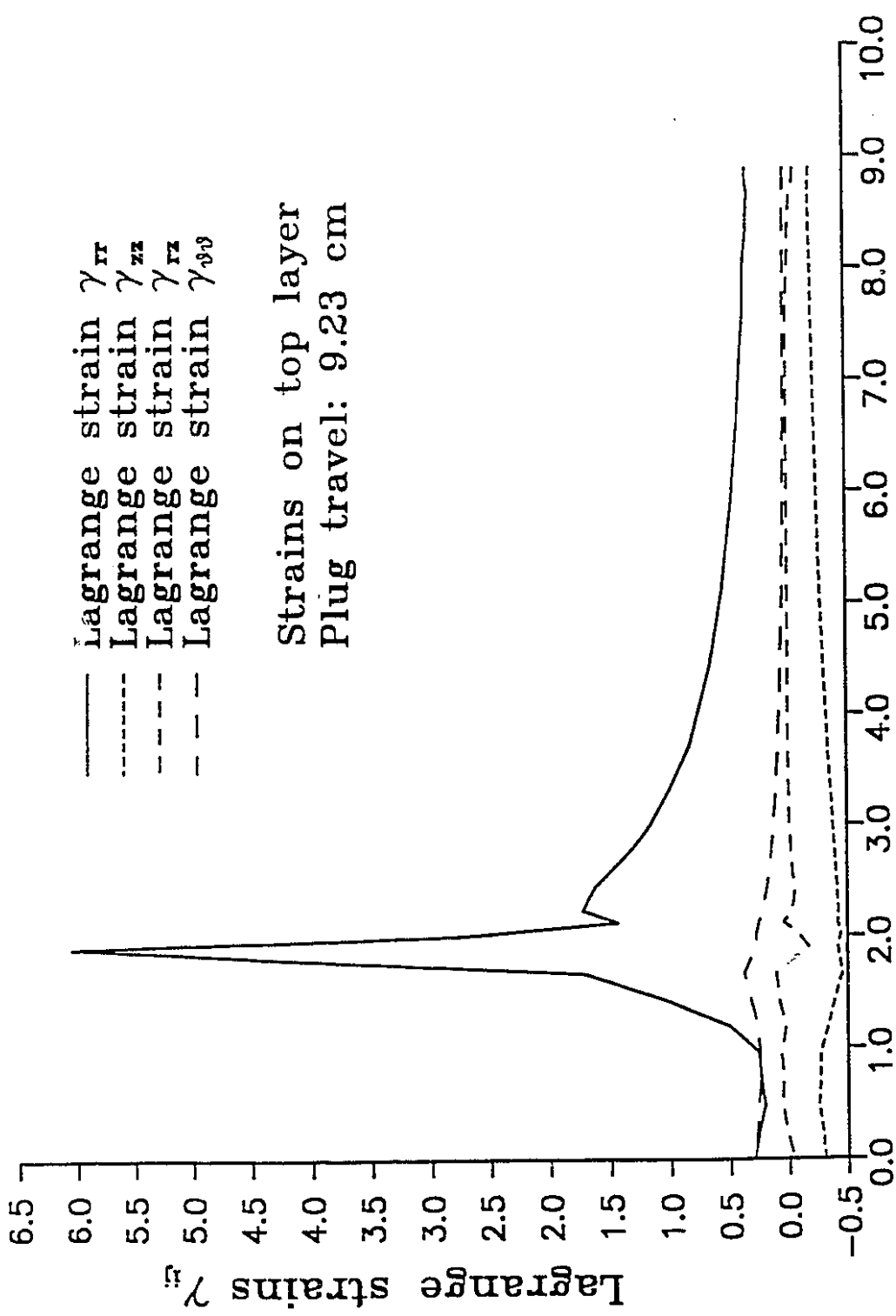

Figure 6.5 Lagrange strains (slip at plug surface).

6.4 Comparison of Numerical Simulations with Throne's Test Results

Throne's test results (1989) are also studied. For 0.01 inch (0.0254 cm) thick sheet and 0.03 inch (0.076 cm) thick sheet, plugs with radii 1.05 cm and 2.30 cm are chosen, respectively. Initial radius is r_0= 7.62 cm, and material parameters obtained by Throne are used. For t_0= 0.01 in sheet, C_{10}= 17.587 psi (0.1213 MPa) and C_{01}= 4.825 psi (0.3327 10^{-1} MPa); for t_0= 0.03 in sheet, C_{10}= 25.11 psi (0.1731 MPa) and C_{01}= 0.581 psi (0.4006 10^{-2} MPa). Gradually changing sheet profiles for 0.01 in thick sheet are shown in Figure 6.6. Views of three-dimensional formed part are shown in Figure 6.7. For 0.03 in thick sheet, our results seem better than those of Throne (Figure 6.8). While for 0.01 in thick sheet, Throne's C_{10} and C_{01} are smaller than those measured by Treloar for natural rubber (1975). Numerical simulations, together with Throne's show much softer force curves than experimental ones. If Treloar's material parameters are used, that is, C_{10}= 20.78 psi (0.143 MPa) and C_{01}= 4.825 psi (0.03327 MPa) [$6(C_{10}+ C_{01})$ = 153.6 psi], again, numerical simulations compare well with Throne's test (Figure 6.9). From Figure 6.4 for Williams' problem, it is known that the deformation is only approximately in plane strain state in the region away from the plug and the clamped end. This is why the present general finite element simulation is better than Throne's analytical solution where plane strain was assumed.

The effect of end boundary condition on the deformed profile is shown in Figure 6.10 for Williams' test. One boundary condition is a simple supported end, i.e., the end is allowed to rotate. Another is a clamped end, and no rotation is possible. Differences for various boundary conditions are significant for the deformed profiles. But small differences are observed in the plug force curves (Figure 6.8). It must be noted that if the thin membrane

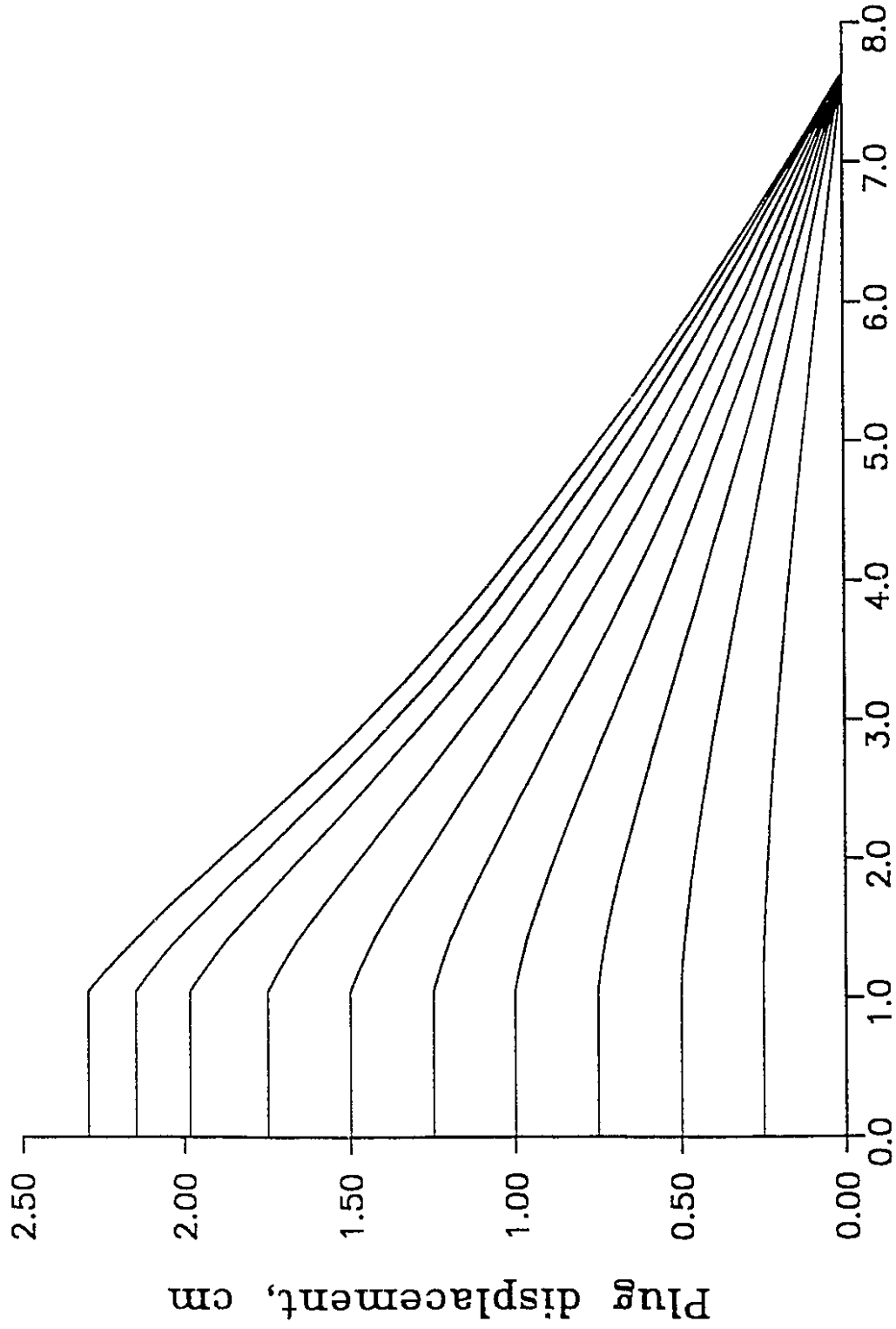

Figure 6.6 Calculated profiles with Throne's data of rubber sheet.

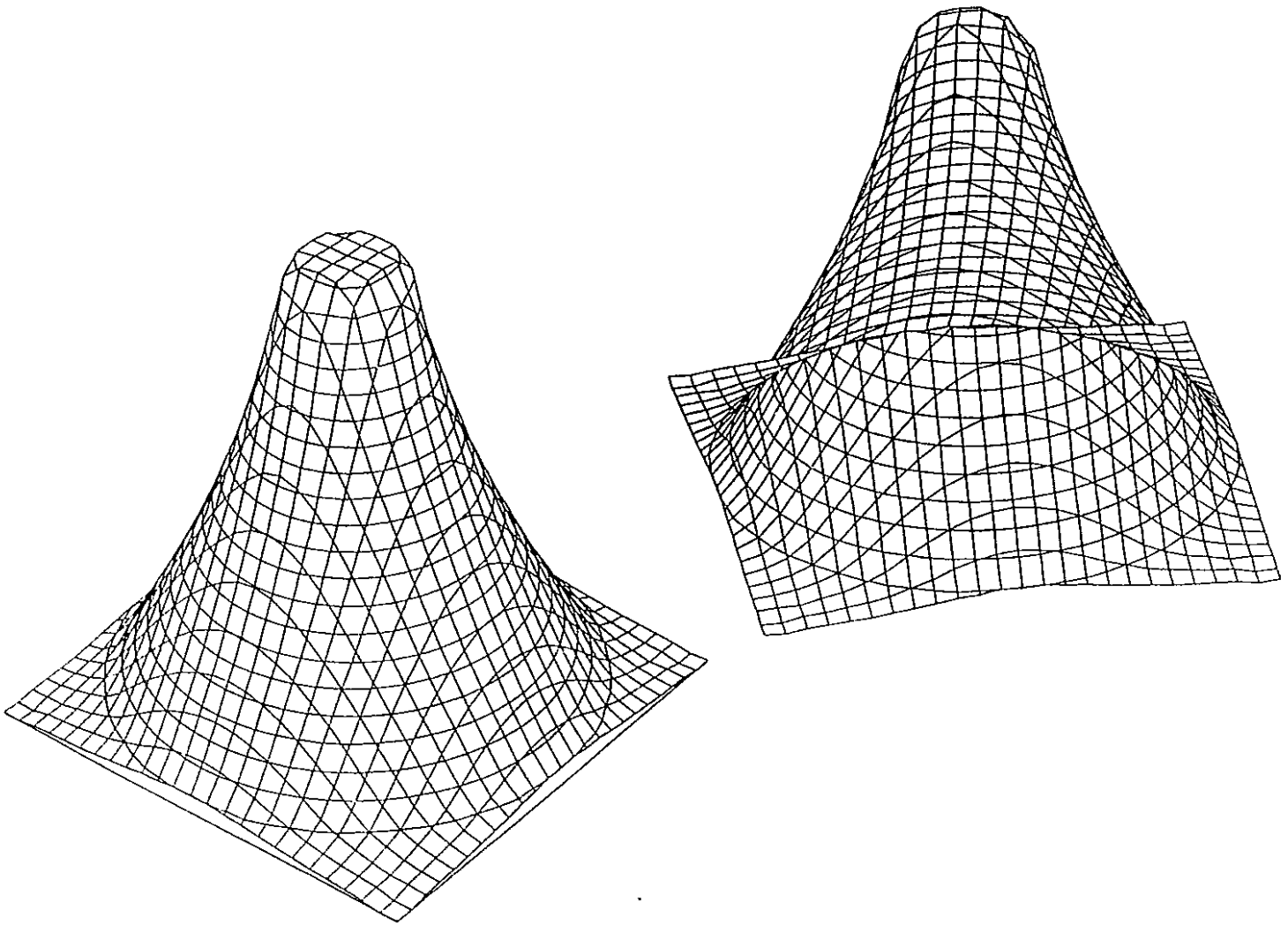

Figure 6.7 Three-dimensional views of the formed part.

(Note: The wrinkling at boundary, or drawing-in from clamped end, is due to the three dimensional graphics software. The simulation is carried out with clamped end.)

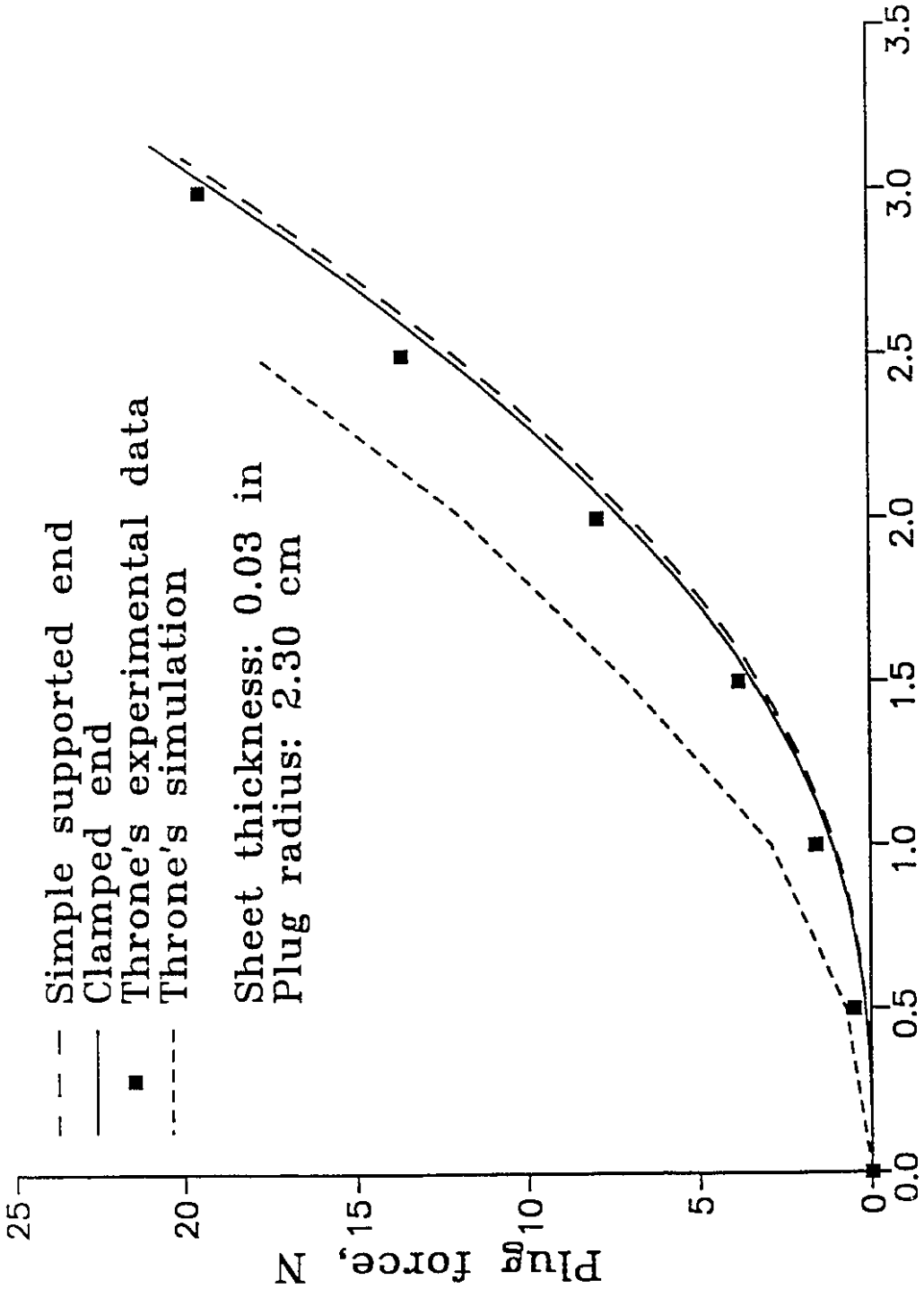

Figure 6.8 A comparison with Throne's experiment for a thick rubber sheet.

approximation is used, we are unable to incorporate the real clamped end condition, i.e. the rotation restriction, as no bending effect is considered in membrane approximation.

Unlike the thin membrane approximation, where the incompressibility condition in finite element formulation may not require consideration (deLorenzi and Nied, 1991), thick sheet approximation must include this condition and therefore, the computational difficulty increases. In implementing the penalty finite element model, numerical stability can be achieved if penalty terms in finite element matrices are evaluated by reduced integration and the so-called Babuska-Brazzi condition is satisfied (Engelman, et al. 1982). Otherwise, spurious oscillations may be encountered in the solution. In the present study, for example, computation will fail to converge at a very early stage of the stretching if no reduced integration is made. For the problems investigated, numerical experiments show that convergence of the approximation is improved with a seven-point Gaussian quadrature for the regular stiffness matrix and a three-point quadrature for stiffness contributed from the penalty terms.

6.5 Strain and Stress Analyses

Strain and stress analyses are made for Williams' problem for both slip and no slip simulations. Stresses at a nodal point are evaluated by averaging stresses over elements meeting at that node. One of the basic methods for detailed modeling of stresses near "sharp" corners, which may create large gradient and discontinuous stress patterns, is to use a refined mesh so that peak stresses at corners can be computed (Segerlind, 1975). With slightly refined meshes shown in Figure 6.1, simulations of Williams' problem

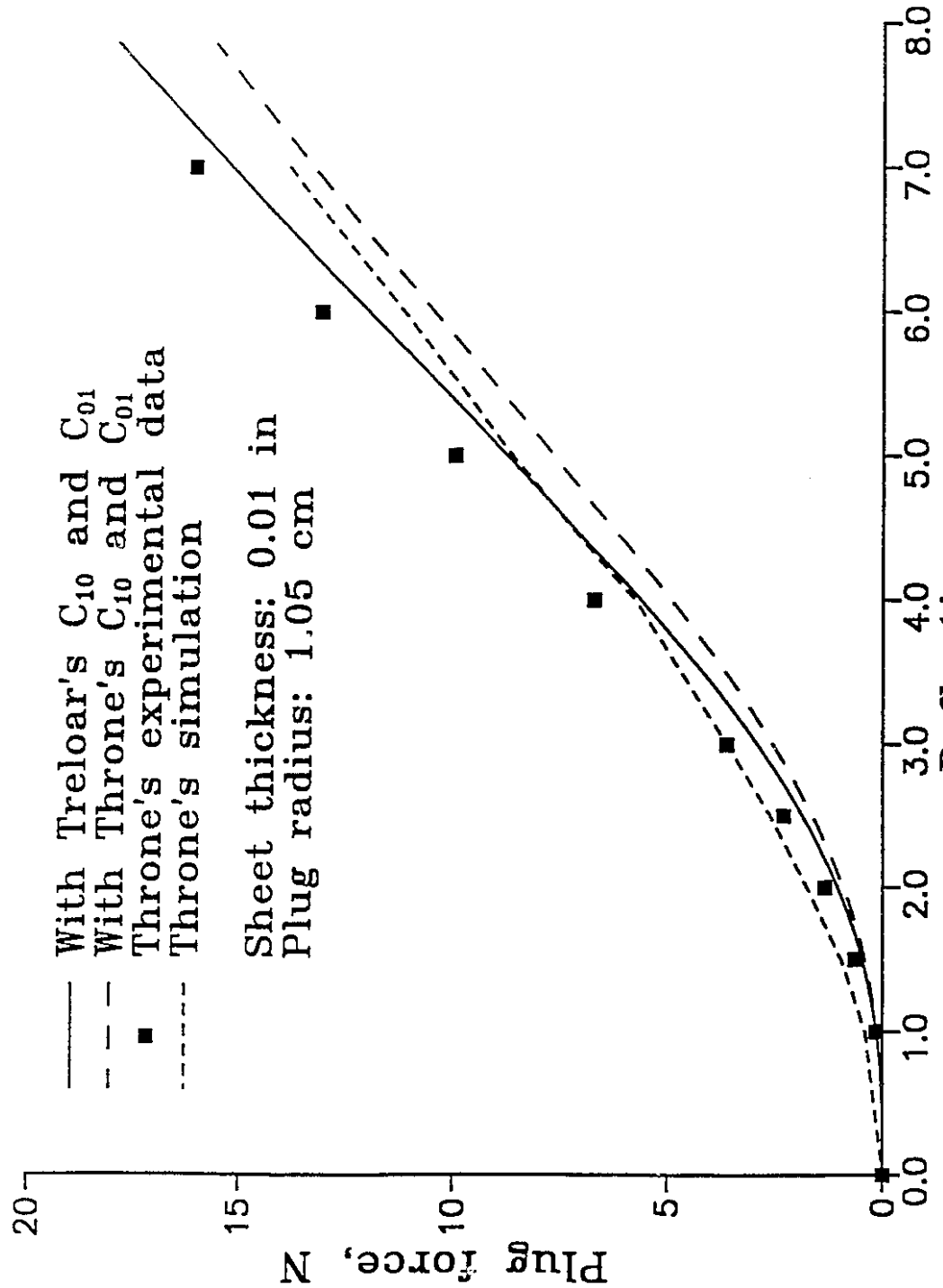

Figure 6.9 A comparison with Throne's experiment for a thin rubber sheet.

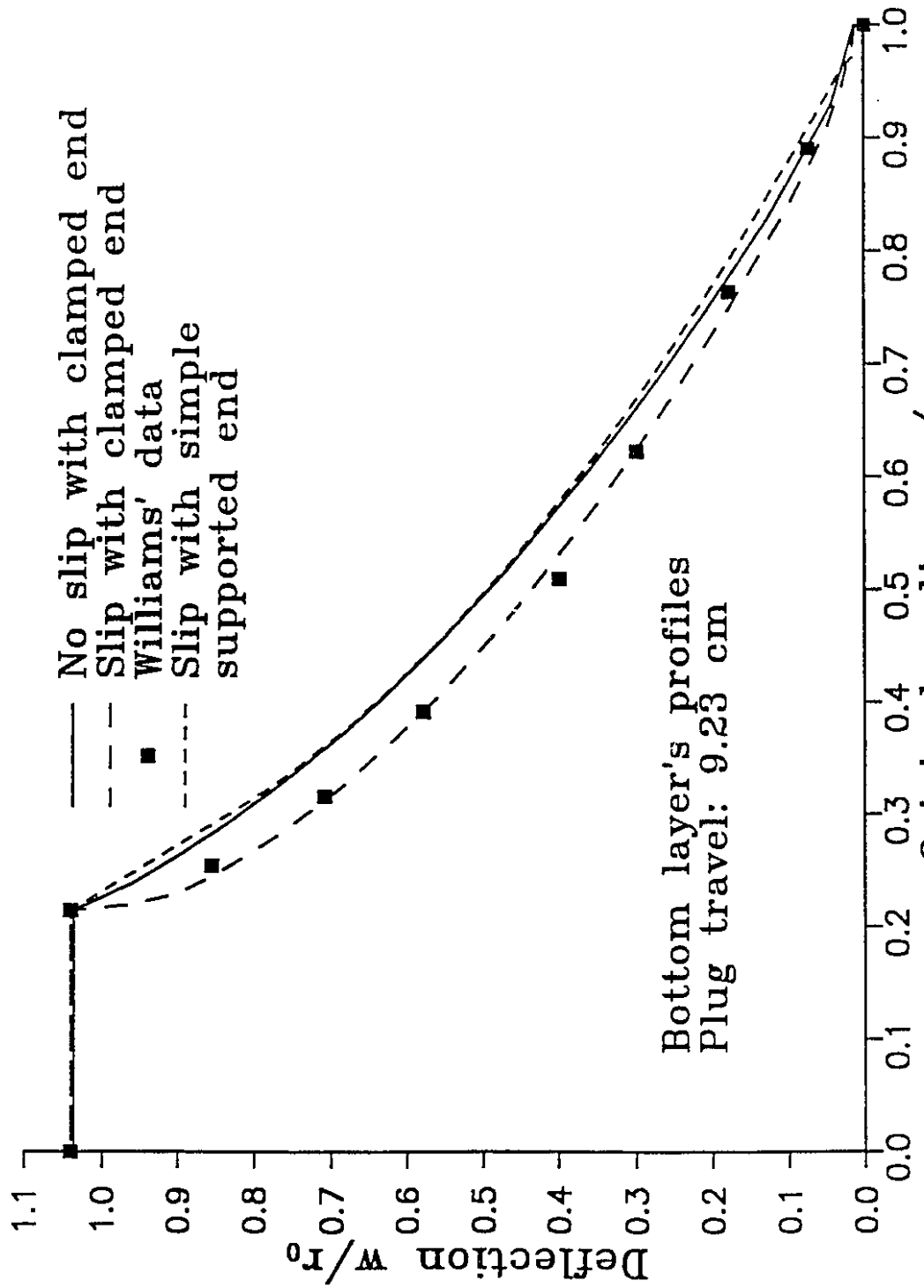

Figure 6.10 The effect of end boundary conditions.

without slip have been successfully carried out to a plug distance of about 20 cm, and could continue without divergence, even if a "sharp" corner exists and stresses near the corner vary dramatically. However, for Williams' problem with slip, simulations can not go that far before divergence occurs. Slip is realized by releasing the restriction on the horizontal displacement of the nodes in contact when these nodes are pulled out of the plug.

In the slip case, directions of principal Euler strains near the pole, and away from the plug are along meridional (ε_1), thickness, (ε_2), and circumferential (ε_3) directions, respectively, as shown in Figure 6.11. The principal directions of σ_1, σ_2, and σ_3 are the same as ε_1, ε_2, and ε_3. Calculated maximum stresses σ_1, σ_2, and σ_3 are at a point with an original radius 1.905 cm (plug edge point). After deformation, this point slips out of the plug edge. Surprisingly, maximum strain ε_1 and ε_2 happen at a point in the middle of the sheet, instead of at a surface point. Figure 6.11 shows maximum strain and stress points at which the sheet may eventually fracture, or be prone to stress cracking.

In the no slip case, strain state is very complex over the plug top and near the plug edge. All maximum principal strains occurred at the top face of the sheet. Maximum ε_1 and ε_2 are at the point with the original radius about 2.1 cm., which is slightly away from the plug edge. Maximum ε_3 is at the pole. Strain contours are plotted out in Figure 6.12. Strains and stresses are normalized according to the rule: $\bar{\varepsilon}_i = \{ [\varepsilon_i - (\varepsilon_i)_{min}] / [(\varepsilon_i)_{max} - (\varepsilon_i)_{min}] \}$. The 2nd principal strain $\varepsilon_2 (=\varepsilon_t)$ is always negative, which means thinning across the thickness direction happens everywhere on the sheet. Away from the plug and clamped end, equal ε_2 lines are approximately perpendicular to the sheet faces (Figure 12 (b)), i.e., there is little change of ε_2 in the

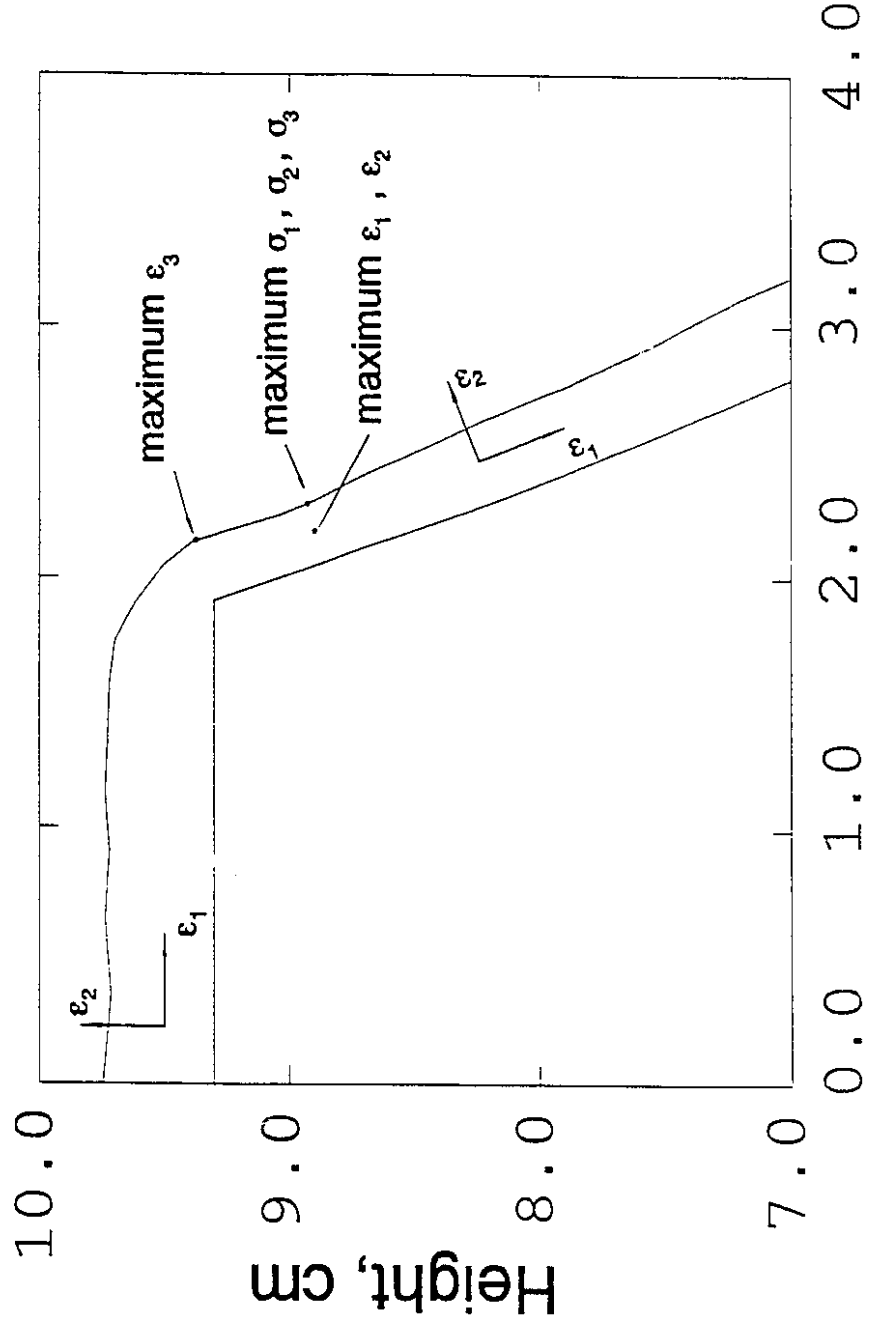

Figure 6.11 Principal strain directions and maximum strain and stress points (slip at plug surface).

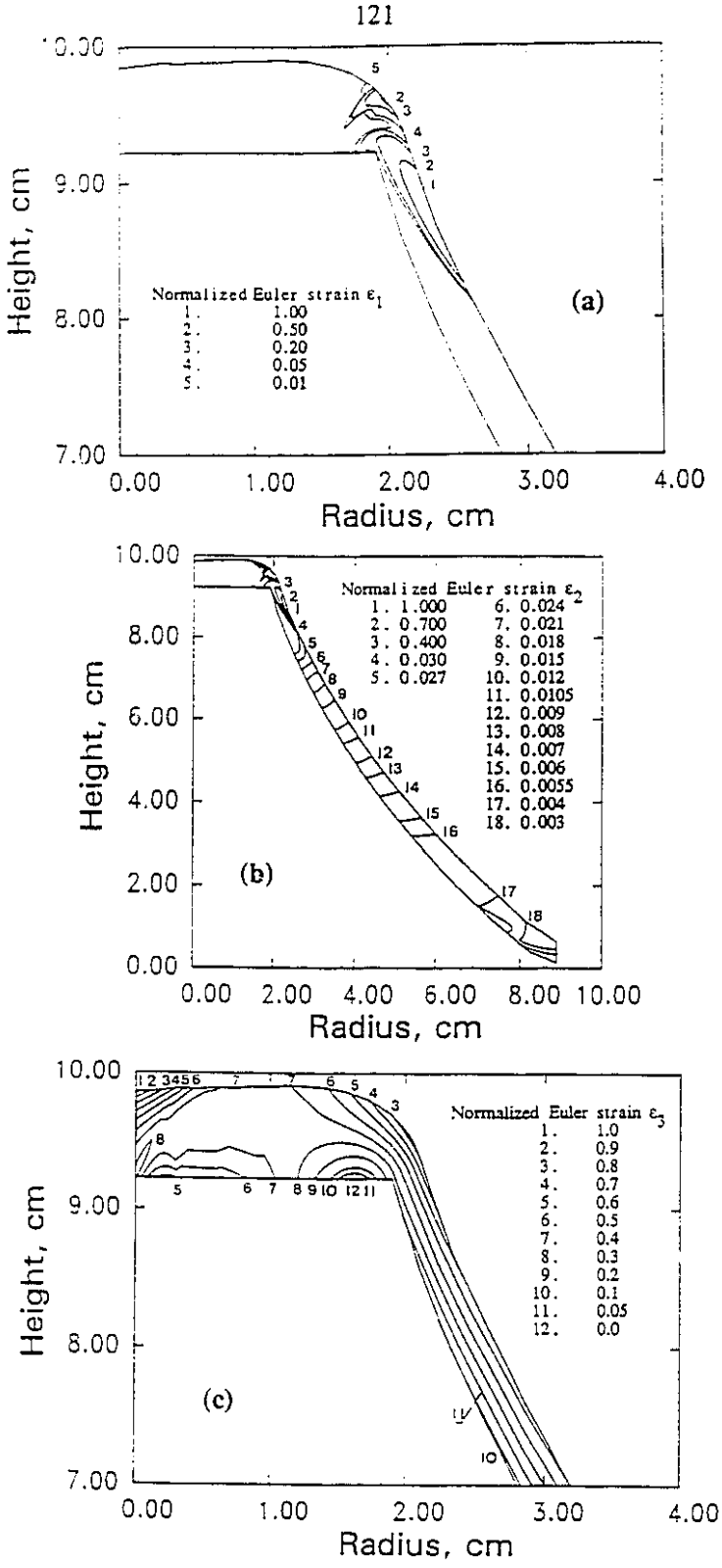

Figure 6.12 Parts of normalized principal strain contours (no slip).

thickness direction. The sheet in this range behaves as a thin membrane. This is the reason why thin membrane simulation can yield reasonable thickness approximation even for a relatively thick sheet (Williams, 1970).

All three maximum Cauchy stresses locate at tne same point on the top face with an original radius 1.905 cm (edge point) as shown in Figure 6.13. In the deformed configuration, the distance between locations of maximum stress(σ_1, σ_2) and maximum strain (ε_1, ε_2) is less than 10% of the plug radius. In Figure 6.13 stress contours are plotted in which stress concentration at the plug edge is clearly shown. Principal stresses on the bottom face of the sheet also achieve their local maximum at the edge. Figure 6.14 illustrates stress distributions on top and bottom surfaces. Fracture of final products is likely to occur at regions of maximum stress concentration, or at regions of maximum strain. In fact, fracture phenomena were observed in deep drawing experiments of a cross-ply laminated oriented polypropylene by Di Pede and Woodhams (1989), who found that the outer ply of laminated wall had a greater strain after forming than the inner wall and the transverse direction side wall of the outer ply tended to fail before the inner wall. In their experiments, no slip between the punch and deformed sheet is mentioned.

Figure 6.15 shows the circumferential principal strain ε_3 in both slip and no slip cases. Maximum strain occurs at both the center and the edge, where strain cracking is prone to happen. Further experiments are needed for a better understanding of stress distribution. However, the present simulation shows clearly the regions where the sheet is likely prone to fracture.

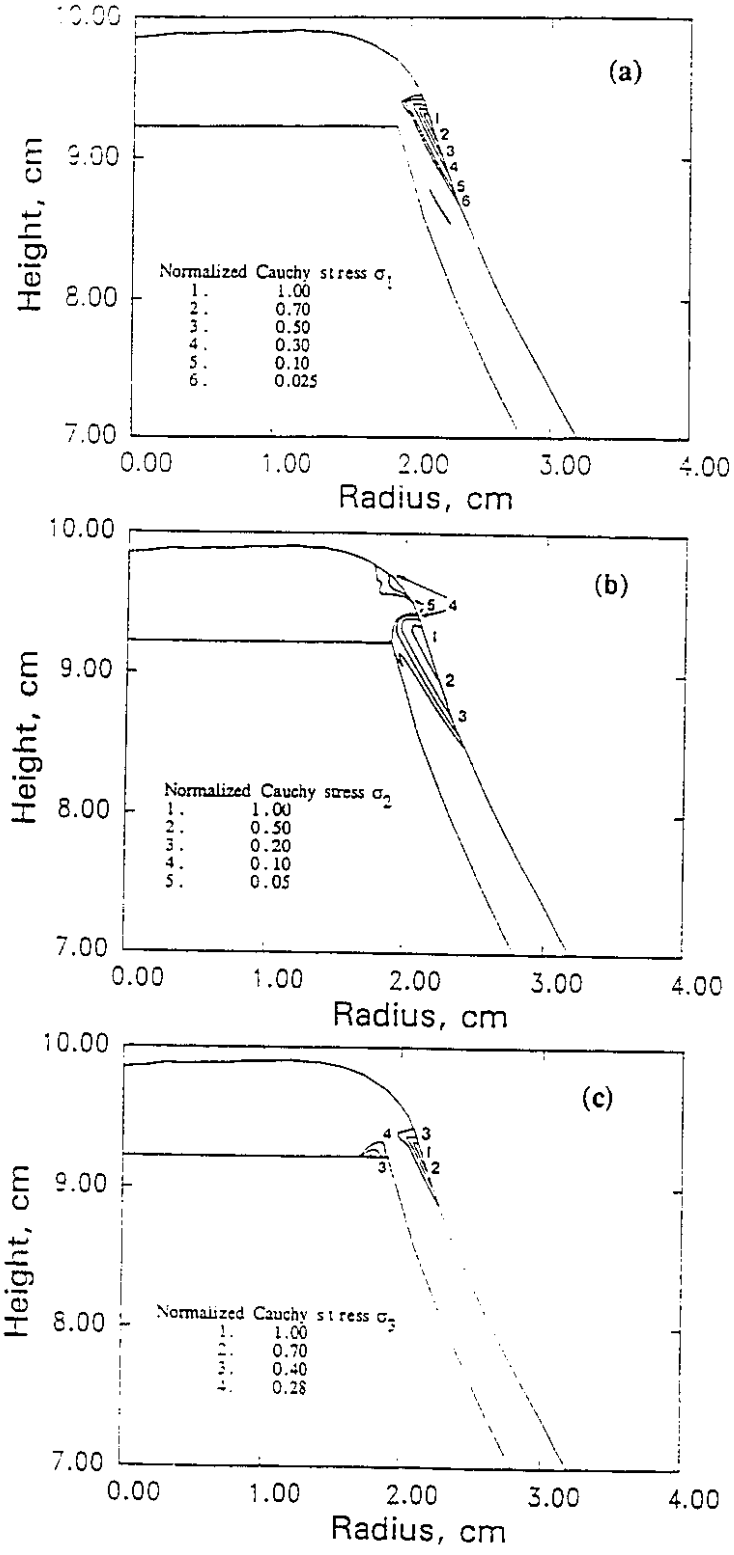

Figure 6.13 Parts of normalized principal stress contours (no slip).

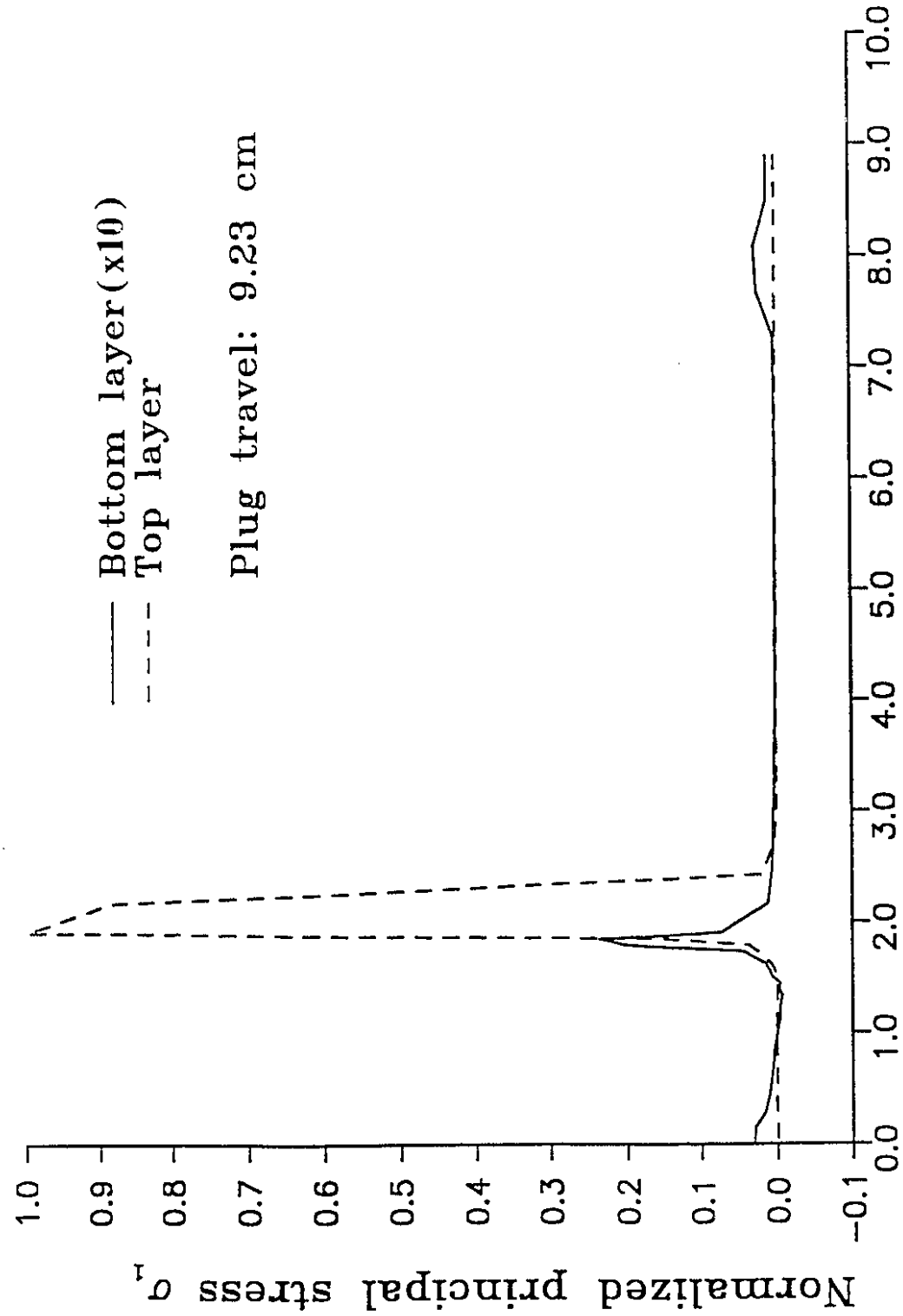

Figure 6.14 Normalized principal stress σ_1 on surface layers of the sheet.

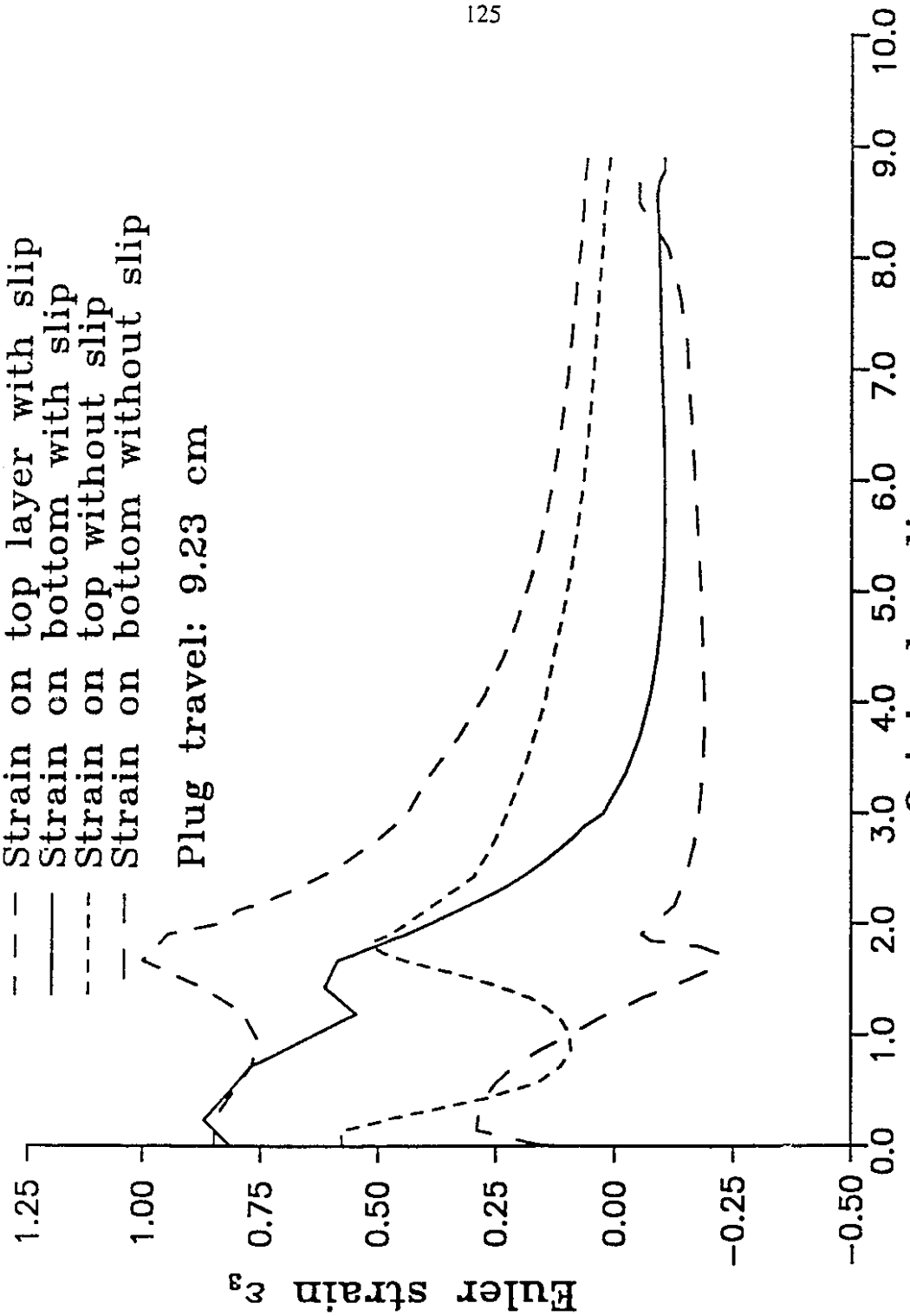

Figure 6.15 Circumferential strain ε_3 in both slip and no slip cases.

6.6 Combination of Plug-assist Pre-stretching and Vacuum Forming

Plug-assist pre-stretching is used to improve thickness distribution of a formed part. In this section, for thermoforming of an industrial part, simulation of plug-assist pre-stretching is performed first. When plug travels to about 60 % of the mold depth, the process is switched to vacuum forming until the sheet fills the mold, as shown in the gradually changing sheet profiles in Figure 6.16. The same geometrical and material parameters as those in the example of straight vacuum forming (Figures 5.5 and 5.6) are used so that a comparison of thickness variation can be made, see Figure 6.17. It is clear that combination of plug-assist pre-stretching and vacuum forming changes thickness distribution dramatically. In this case, the plug-assist pre-stretching thermoforming yields much thicker bottom. By choosing plug size and plug distance, thickness distribution can be controlled to achieve optimization. Non-isothermal heating can also be used as a control means to change thickness distribution, which is detailed in Song and Meguid (1993).

6.7 Concluding Remarks

Thick sheet finite element analysis can simulate the plug-assist forming of thermoplastic and rubber sheets and accurately predict thickness variations. Sheet thickness variations and plug force versus deflection show good agreement with experimental data available in the literature. Combination of plug-assist pre-stretching and vacuum forming changes thickness distribution and can be used to optimize process design. The present analysis can also provide complete stress and strain distributions and locate critical regions where fracture phenomena are likely to be initiated.

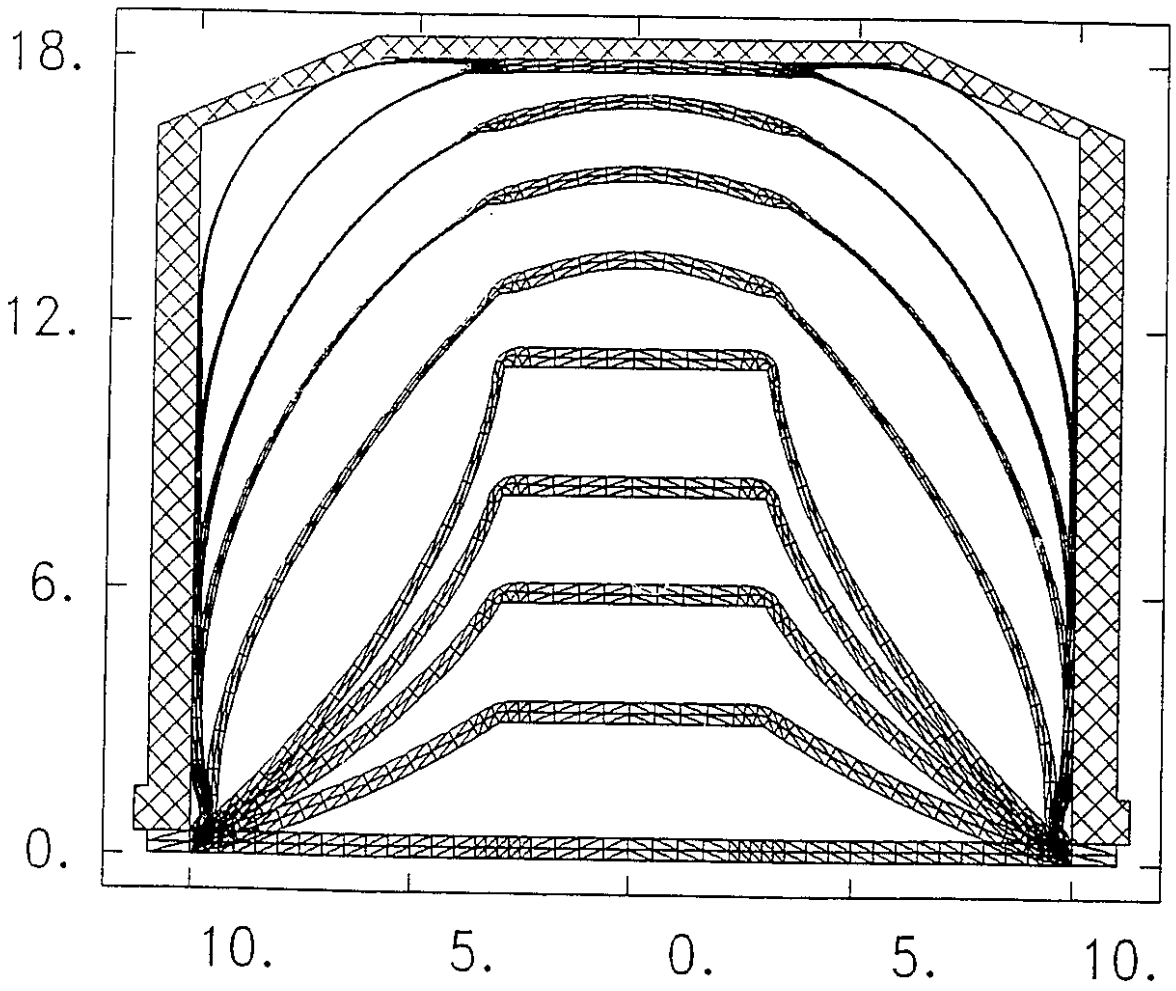

Figure 6.16 Combination of vacuum forming and plug-assist forming.

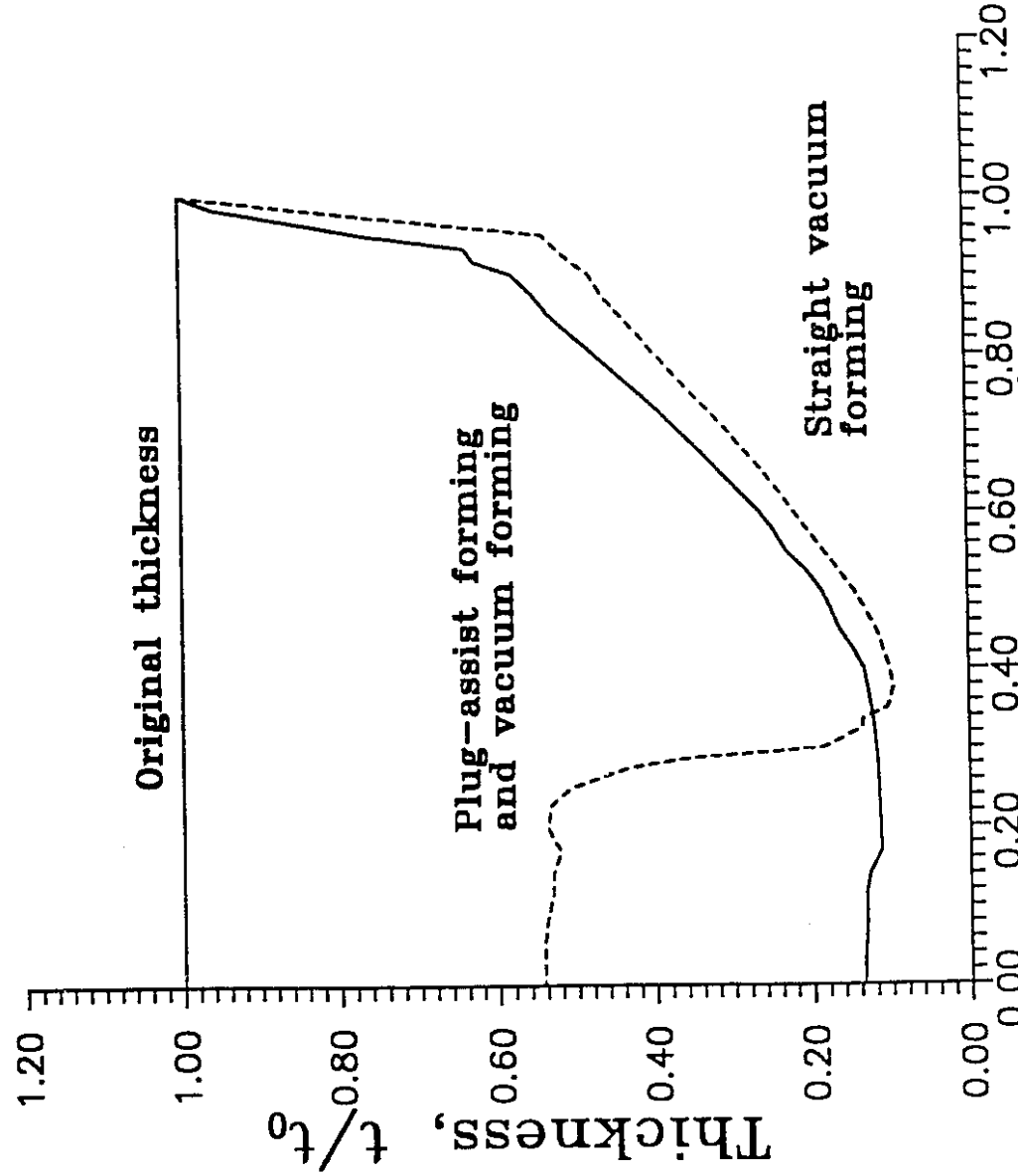

Figure 6.17 A comparison of thickness variation of straight vacuum forming with the combined forming.

CHAPTER 7
SIMULATION OF COMPRESSION FORMING

7.1 Introduction

Compression forming involves compression of materials. The behavior of material during the process is of concern. The material can be metal, polymer solid or melt. The usual compression ratio of deformed thickness to the original is about 1% to 40 %. Polymer compression forming is a special polymer processing operation, in which a polymer block, either in glassy-state or melt state, is squeezed into some final product. The compression ratio can be as high as 99%. Compression of polymer melts is also called squeezing flow. Product fabricated in compression forming has good molecular orientation and strength properties. Compression forming is used for thermosetting compounds such as urea, phenolic, epoxy, metamines, and rubber, for sheet molding compounds, bulk molding compounds, thermoplastic sheet stamping, and compounding reinforcements (Whiteside, 1990).

Three different analysis methods are used to handle compression and compression forming of polymeric materials.

1. Analytical methods

In studying compression of bonded rubber cylinder, Lindley (1970) obtained a closed-form relation between compressive force and deflection, which was used in design and fabrication of elastomeric products. The solution is purely nonlinear elastic. Thornton and Dillard (1988) used a linear elastic

model to study the frictional force for elastomeric disk in compression and produced an implicitly closed-form solution.

In analysis of squeezing flow, closed-form solutions of applied force, pressure distribution, and velocities can be obtained if lubrication approximation is used with Newtonian flow, or power-law viscometric flow, or simple viscoelastic flow models (Leider and Bird, 1974, and Leider, 1974). It is assumed that only shear deformation is considered and instantaneously the flow can be described as steady-state flow between two parallel plates. These analytical solutions help to understand the individual effect encountered in this flow, such as shearing, stretching, elasticity, stress overshooting, and inertial effects. They also serve as basis of various rheometers to measure flow-properties of polymers. Yet, Isayev and Azari (1986) obtained closed-form solutions, or analytical solutions with simple numerical technique, by using shear-free squeezing flow. Closed-form solutions are preferred by design and processing engineers for their simplicity. Of course, the closed-form solutions are not applicable when complex, irregularly-shaped components are designed, or more complicated viscoelastic models are incorporated. Therefore, the analysis is carried out by employing the finite element method more frequently at the present time.

Rogers established a simple continuum model to describe the viscous squeezing flow of highly anisotropic material such as fibre-reinforced resins (1989). Simple relationship between the compressive force and deflection obtained for fibre-reinforced Newtonian fluid are similar to Scott's equation (1931, 1932), also see Leider and Bird (1974). Recently, Vancso et al. (1990), and Bruce et al. (1992) carried out experiments to investigate the development of molecular orientation (anisotropic structure) during compression of

cylindrical polypropylene (PP) disks. There has been much less work done on compression forming of reinforced polymers.

2. Application of metal forming finite element analysis

Many nonlinear finite element analysis commercial packages are available on the market, such as ADINA (ADINA, 1988), ABAQUS (ABAQUS, 1984), which can be used in metal compression forming (upsetting) simulation with Prandtl-Reuss plasticity theory (or von-Mises yield with its associated flow rule) and some hardening rules (Shih and Yang, 1991). Simulations are quite successful with a compression ratio which is not high. Anisotropy is also considered in numerical analysis (Bay and Chenot, 1990). This methodology can be applied to analyze polymer compression forming (Lee et al. 1991) by introducing pseudo viscoplastic, or elastic-viscoplastic models of polymer, which are similar to that of metal. However, the deformation mechanisms of metal and polymer are quite different. In polymer forming, elastic response may not be linear and it may be difficult to identify where the yielding begins. For polymers, yield phenomenon is usually a gradual transition from an elastic to an inelastic behavior (see Figure 2.1).

3. Viscoelasticity based finite element analysis

Morman and Pan (1987) analyzed compression of elastomers by following the methodology of polymer rheology with ABAQUS program. They developed a correspondence principle for a class of incompressible isotropic, nonlinear viscoelastic rubber-like materials that exhibit time and strain separability effects under stress relaxation. For a given boundary-value problem, a nonlinear elastic response was obtained first by the finite element simulation. Time-dependent viscoelastic effects were introduced a posteriori by performing a temporal integral transformation. Viscoelastic effect can be

predicted in a much easier way than by direct use of K-BKZ model, which is time-consuming. In Morman and Pan's analysis, a bonded cylinder of rubber is compressed to a ratio of 0.35. The force vs. compression ratio curve was obtained by finite element analysis and compared with a closed-form solution. The normal stress distribution at the bonding interfaces was predicted along with its relaxation. In compression forming of thermoplastics, however, a much larger compression ratio, such as 0.01, is expected and some area of cylindrical surface will establish contact with the end punch.

Compression with large compression ratio was studied using finite element analysis by Mavridis et al. (1992). A simple power-law viscometric model was used in their simulations, which focused on deformation pattern. The predicted material particle trace was found to be similar to that of fountain flow in injection molding (Mavridis, 1988). No stress analysis results were reported.

General theoretical and numerical analysis on compression forming of polymers with large compression ratios and a more realistic constitutive equations are still needed.

As shown in Figure 7.1, deformation in compression is nonhomogeneous. Both shear and extension exist and kinematics are not known a priori. The prediction of the deformation pattern in compression forming is the major concern in this work. Comparisons of numerical simulations with analytical solutions and experiments are carried out.

7.2 Modeling of Process

A "displacement drive" solving process similar to plug-assist forming is employed in finite element simulations of a cylindrical block compression.

Due to symmetry, only a quarter of the problem domain (the shadowed area in Figure 7.1) is discretized. When the upper plate moves down, the outer surface of the cylinder swings up and gradually establishes contact with the plate. A contact check routine is used to guarantee satisfaction of changing boundary conditions, which was outlined in Chapter 5.

Finite element simulations are carried out based on general large deformation analysis and hyperelasticity for fast compression process, where there is little time for viscous dissipation. The finite element results are compared to analytical solutions for compression without friction at the end interfaces and for stick interfaces with excellent agreements. Practical compression forming is then analyzed. Compression force characteristics, deformation pattern, stress distribution at the end interface are obtained.

7.3 Numerical Results

7.3.1 Comparison of Finite Element Results with Analytical Solution (Compression without Friction)

An ideal compression without friction between mold and deformed circular cylinder is considered first. The material is assumed to be Mooney hyperelastic. This deformation is a homogeneous process and is equivalent to equibiaxial extension. The geometry is shown in Figure 7.1.

Let us assume that

$$\lambda_r = \frac{r}{R} = \frac{r_1}{R_0}, \text{ and } \lambda_z = \frac{z}{Z} = \frac{h}{H} \tag{7.1}$$

then

$$\lambda_\theta = \frac{2\pi r}{2\pi R} = \lambda_r \tag{7.2}$$

From the incompressible condition $I_3 = \lambda_r^2 \lambda_\theta^2 \lambda_z^2 = 1$, we obtain

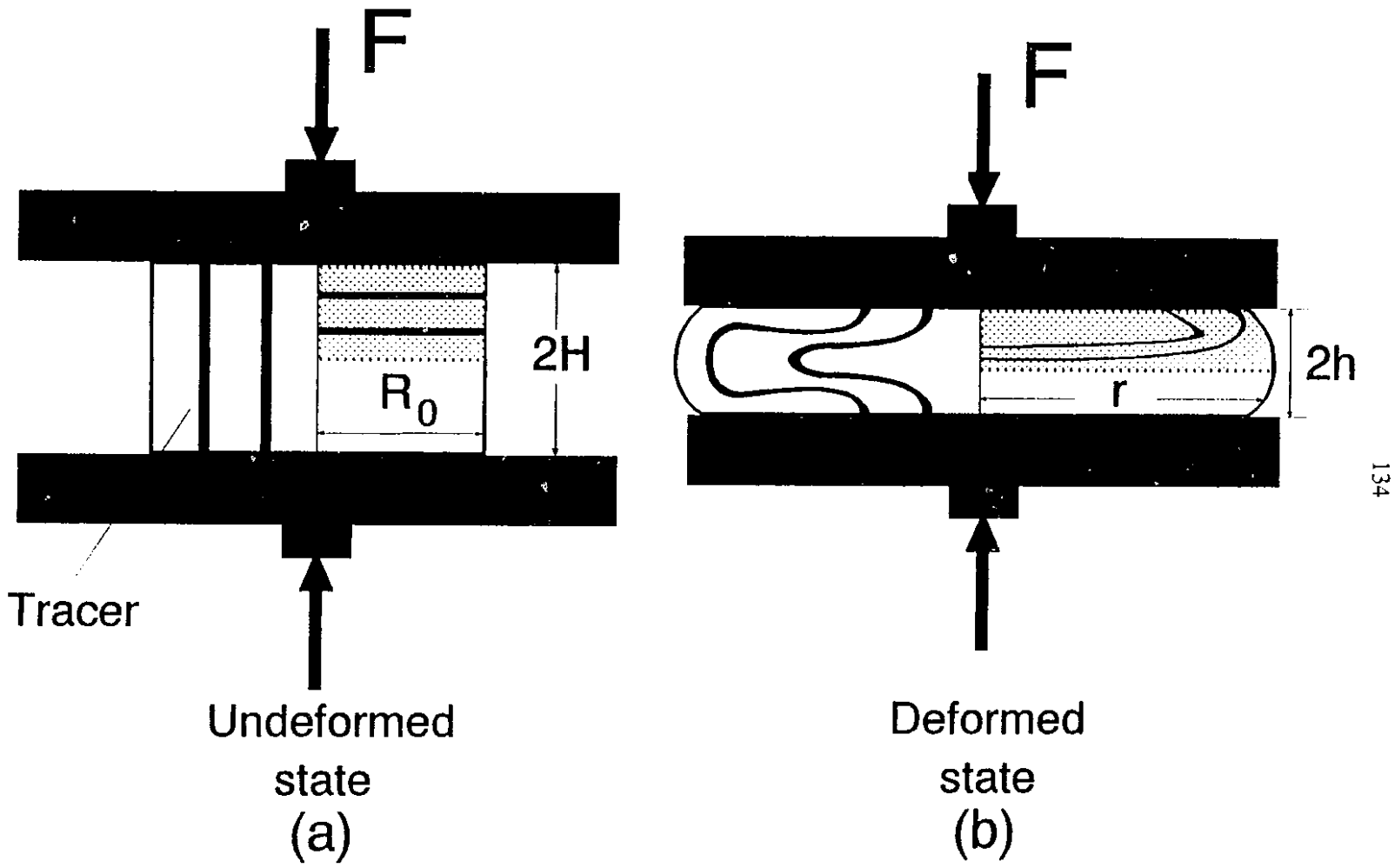

Figure 7.1 Deformation characteristics in compression forming.

$$\lambda_r^2 = \frac{1}{\lambda_z},\ I_1 = 2\lambda_r^2 + \frac{1}{\lambda_r^4},\ \text{and}\ I_2 = \frac{2}{\lambda_r^2} + \lambda_r^4 \tag{7.3}$$

and

$$\begin{cases} \sigma_{rr} = \sigma_{\theta\theta} = 2\,C_{01}\lambda_r^2 - 2\,C_{10}\dfrac{1}{\lambda_r^2} - p \\ \sigma_{zz} = 2\,C_{01}\lambda_z^2 - 2\,C_{10}\dfrac{1}{\lambda_z^2} - p \end{cases} \tag{7.4}$$

where C_{01} and C_{10} are Mooney constants, p, hydrostatic-pressure as described in Chapter 2.

Since deformation is homogeneous and no traction is applied at the surface of $r = r_1$, then pressure p can be determined from the boundary condition $\sigma_{rr} = 0$ at $r = r_1$,

$$p = 2\,C_{01}\lambda_r^2 - 2\,C_{10}\frac{1}{\lambda_r^2} \tag{7.5}$$

and the total compressive force F is given by

$$F = -\int \sigma_{zz}\, d^1A = 2\pi R_0^2 \left(\lambda_r^4 - \frac{1}{\lambda_r^2}\right)(C_{01} + C_{10}\lambda_r^2) \tag{7.6}$$

Using the expressions above the 2nd Piola-Kirchhoff stress S^{zz} can be obtained as

$$S^{zz} = \sigma_{zz}/\lambda_z^2 = -2\,(\lambda_r^6 - 1)(C_{01} + C_{10}\lambda_r^2) \tag{7.7}$$

which, in turn, can be used to check the correctness of stress calculation from finite element simulations.

The finite element simulation is carried out with eight elements. The related parameters are shown in Table 7.1 A comparison of finite element results and the analytical solution in Eq.(7.6) shows excellent agreement, as shown in Figure 7.2. A simple check of incompressibility is also made. When h = 0.3288 cm, r_1 = 2.569 cm, the relative error of volume conservation is

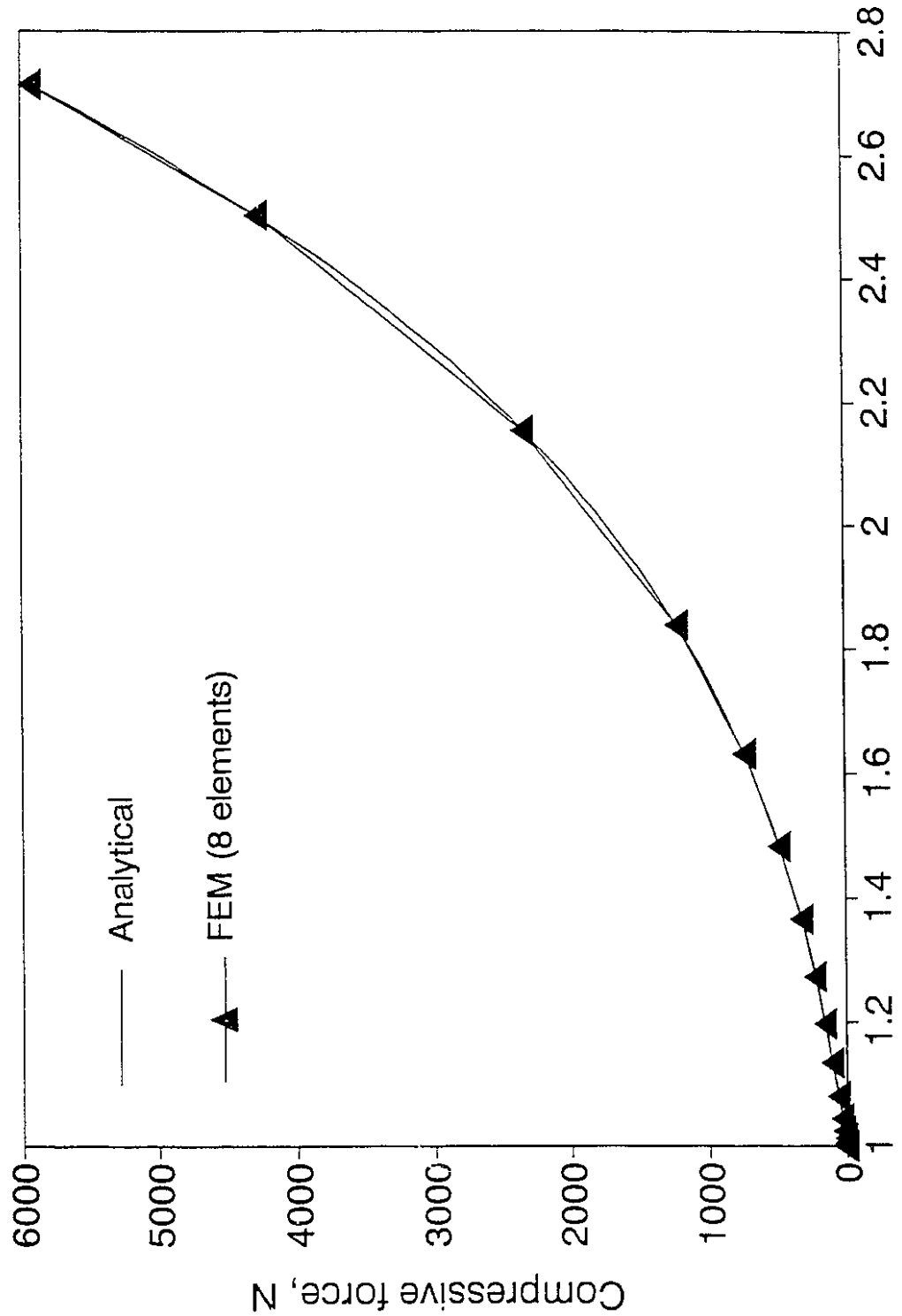

Figure 7.2 A comparison of finite element result with analytical result for homogeneous compression.

$$\frac{V_0 - V}{V_0} = \frac{\pi R_0^2 H - \pi r_1^2 h}{\pi R_0^2 H} = 3.6 \times 10^{-3}.$$

It indicates that volume is well preserved as constant.

It should be noted that by ignoring p, the correct stresses may not be obtained [see, eq.s (7.4) and (7.5)]. For Cauchy stresses, $\sigma_{rr} - \sigma_{zz}$ eliminates pressure p, while for the Poila-Kirchhoff stresses,

$$S^{rr} - S^{zz} = 2\, C_{10}(\lambda_r^8 - \lambda_r^{-4}) + p\,(\lambda_r^4 - \lambda_r^{-2}) \tag{7.8}$$

stress difference depends on the hydrostatic-pressure p. In the thin membrane simulation, the incompressibility condition should be included in the finite element formulation, by either Lagrange multiplier or penalty method, then the value of p corresponding to a specific boundary-value problem could be evaluated, and therefore, complete information on stresses could be obtained.

7.3.2 Comparison of Finite Element Results with Closed-form Solution (Compression with Stick Condition)

Lindley (1970) developed a closed-form equation for no slip allowed between the interface of mold and cylinder. In terms of current nomenclature, Lindley's equation is

$$F = 6\pi\, R_0^2 (C_{01} + C_{10})\left(1 + \frac{kR_0^2}{8H^2}\right)\left(1 - \frac{1}{\lambda_r^2}\right)\left(2 - \frac{1}{\lambda_r^2}\right) \tag{7.9}$$

where k is a numerical factor depending on material hardness, $(R_0/2H)$. Here k is simply chosen to be 1.0. C_{01}= 1.0 MPa, and C_{10} = 0.1 MPa. R_0 and H are listed in Table 7.1.

Sixty four elements and forty five incremental steps are used to simulate this problem. The cylinder is compressed to a total deflection $\delta = 2(H-h) = 1.3$ before contact occurs. A comparison with Lindley's analytical

Table 7.1 Material and geometric parameters used in compression simulation

C_{01}(MPa)	C_{10}(MPa)	R_0(cm)	H (cm)	h (cm)	r_1(cm)
0.10	0.00	1.32	1.25	0.3288	2.569

results is shown in Figure 7.3. Both closed-form solution and finite element results are in good agreement up to $\delta = 0.4$. Thereafter, the two results diverge rapidly with increasing deflection. This observation is similar to Morman and Pan's (1987) result. Lindley's results were based on neo-Hookean material model ($C_{10} = 0$) and higher order terms of strain hardening were neglected, which is the reason the current simulation with Mooney model becomes stiffer than Lindley's at large deflection. The different force-deflection responses for neo-Hookean and Mooney materials were also observed in Figure 4.12 for large inflation of plastic sheet. In Figure 7.3, the force curve of finite element simulation without friction is also given, which is lower than that with friction. From an energy point of view, when friction is present, extra external energy is consumed to overcome shear resistance at the interface.

Another interesting comparison is made between current finite element results and Tanner's analytical solution of squeezing flow for viscoelastic fluid. Tanner (1965, also see Leider and Bird, 1974) used an upper convected Maxwell (UCM) viscoelastic model (see Chapter 2) with a power-law shear viscosity to determine the effect of elasticity of polymer fluid. From Tanner's results we obtain a relationship when $h = H/2$

$$\frac{t_{1/2}}{n\lambda} = K_n \left(\frac{\pi R_0^2 m}{F\lambda^n} \right)^{1/n} \cdot \left(\frac{R_0}{h} \right)^{1+1/n} - 1 \qquad (7.10)$$

where $t_{1/2}$ is the half-time at which $h = H/2$, λ, the relaxation time in UCM,

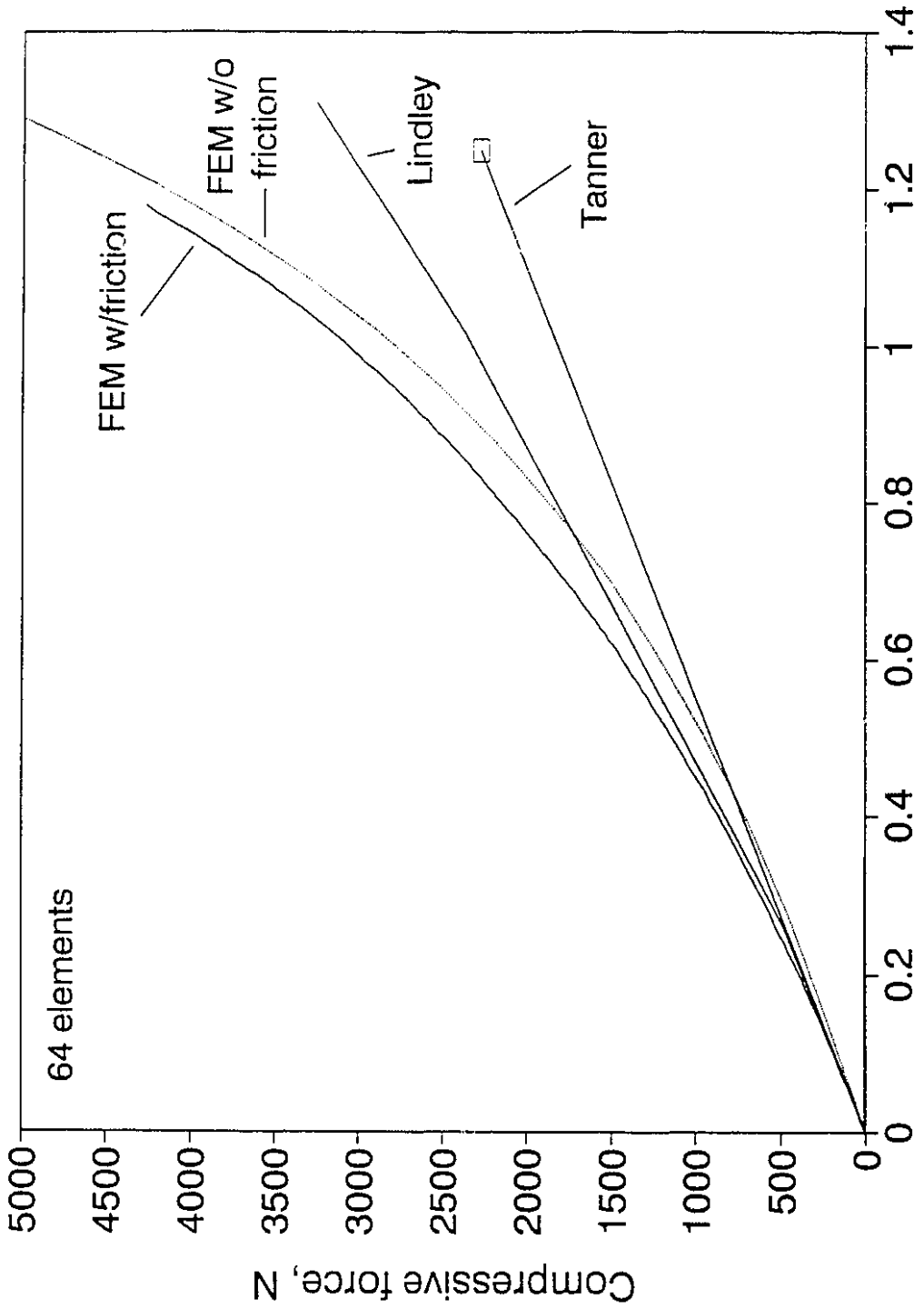

Figure 7.3 A comparison of finite element results with closed-form results for compression with friction.

n, m, the power-law index of viscosity $\eta = m\,\dot{\gamma}^{n-1}$, and a constant, and

$$K_n = \left[\frac{2^{1+1/n} - 1}{2n}\right]\left[\frac{2n+1}{n+1}\right]\left[\frac{1}{n+3}\right]^{1/n}$$

When $t_{1/2}/n\lambda$ is very small, the calculated compressive force F is related to initial elastic response. If a constant viscosity is assumed, i.e. $n = 1$, $\eta = m$, then the Young's modulus $E = \eta/\lambda = 6(C_{01} + C_{10})$. From (7.10) (and the condition $t_{1/2} = 0$), we have

$$F = \frac{9}{16}\pi R_0^2 E (R_0/H)^2 \tag{7.11}$$

This is the force at $h = H/2$. Since linear elastic response is assumed in UCM, it follows that a linear relation of initial elastic response is also valid for other compression ratios. This result is also plotted in Figure 7.3. Compared with Lindley's solution and finite element results, we observe that the latter two are much stiffer than Tanner's. This is because nonlinear elastic response is involved in the latter two cases.

7.3.3 Compression Forming with Contact

A finite element grid with sixty-four elements is used in simulation of compression forming with contact and is shown in Figure 7.4. Material and geometric constants are those used for the example in Section 7.3.2 and presented in Table 7.1. The plot of compressive force vs. extension ratio appears in Figure 7.5. Since the total Lagrangian description is adopted in current finite element simulation, finite element grid lines represent material lines. Figure 7.6 shows gradual compression processing. It also shows that on the vertical lines, material points near the centre move much further than those near the upper plate, while the horizontal lines swing up. A fountain-like pattern of material lines is clearly observed. If the nodes on

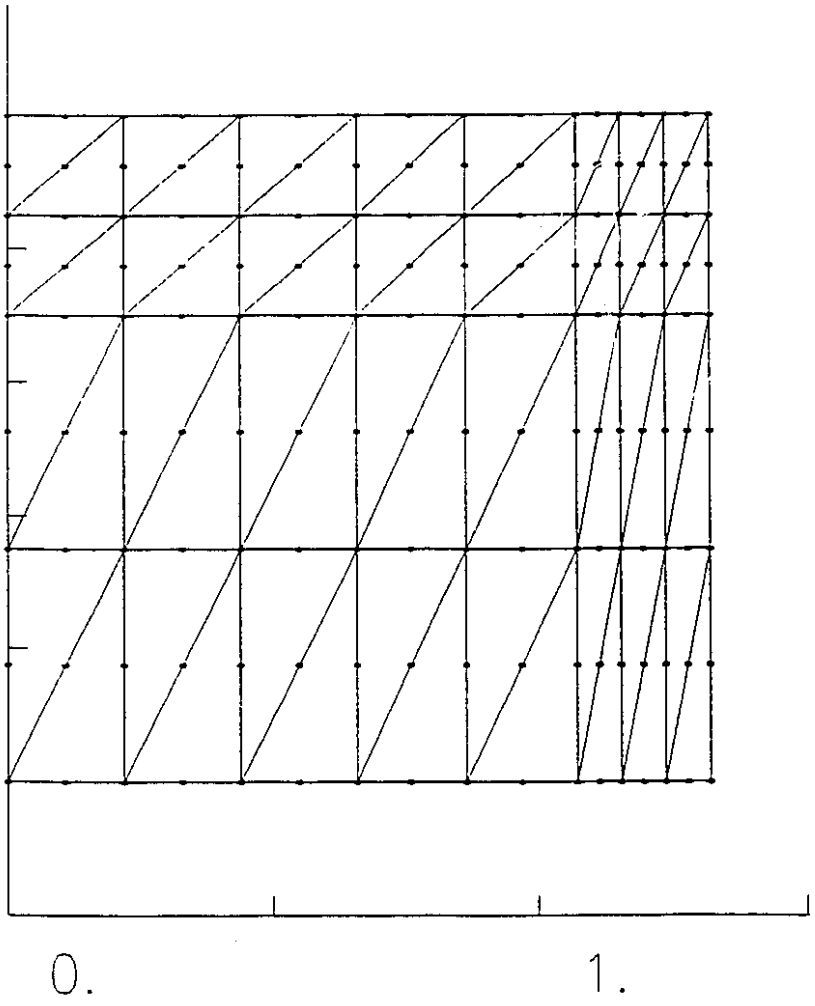

Figure 7.4 Finite element grid with 64 elements.

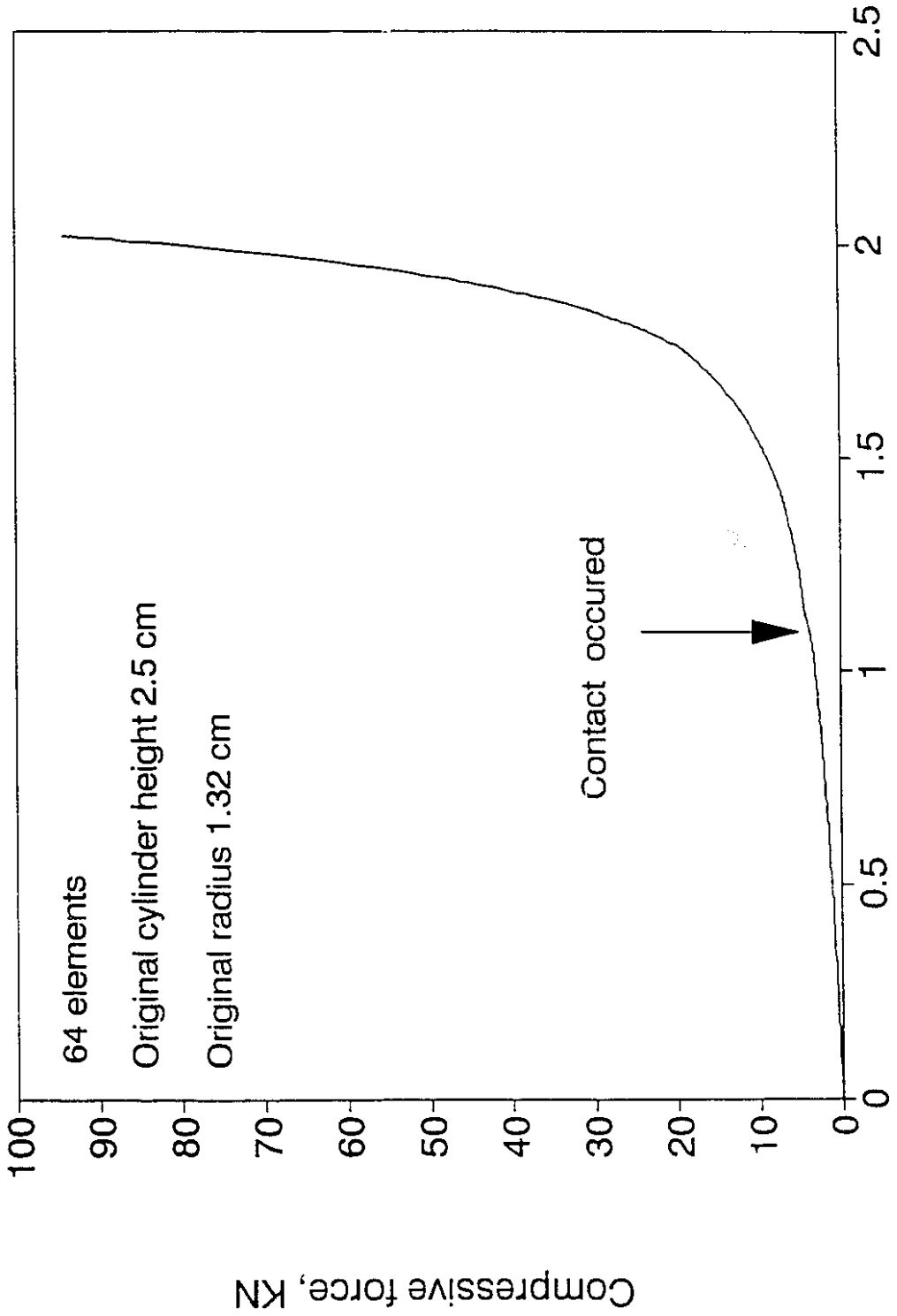

Figure 7.5 Compressive force curve.

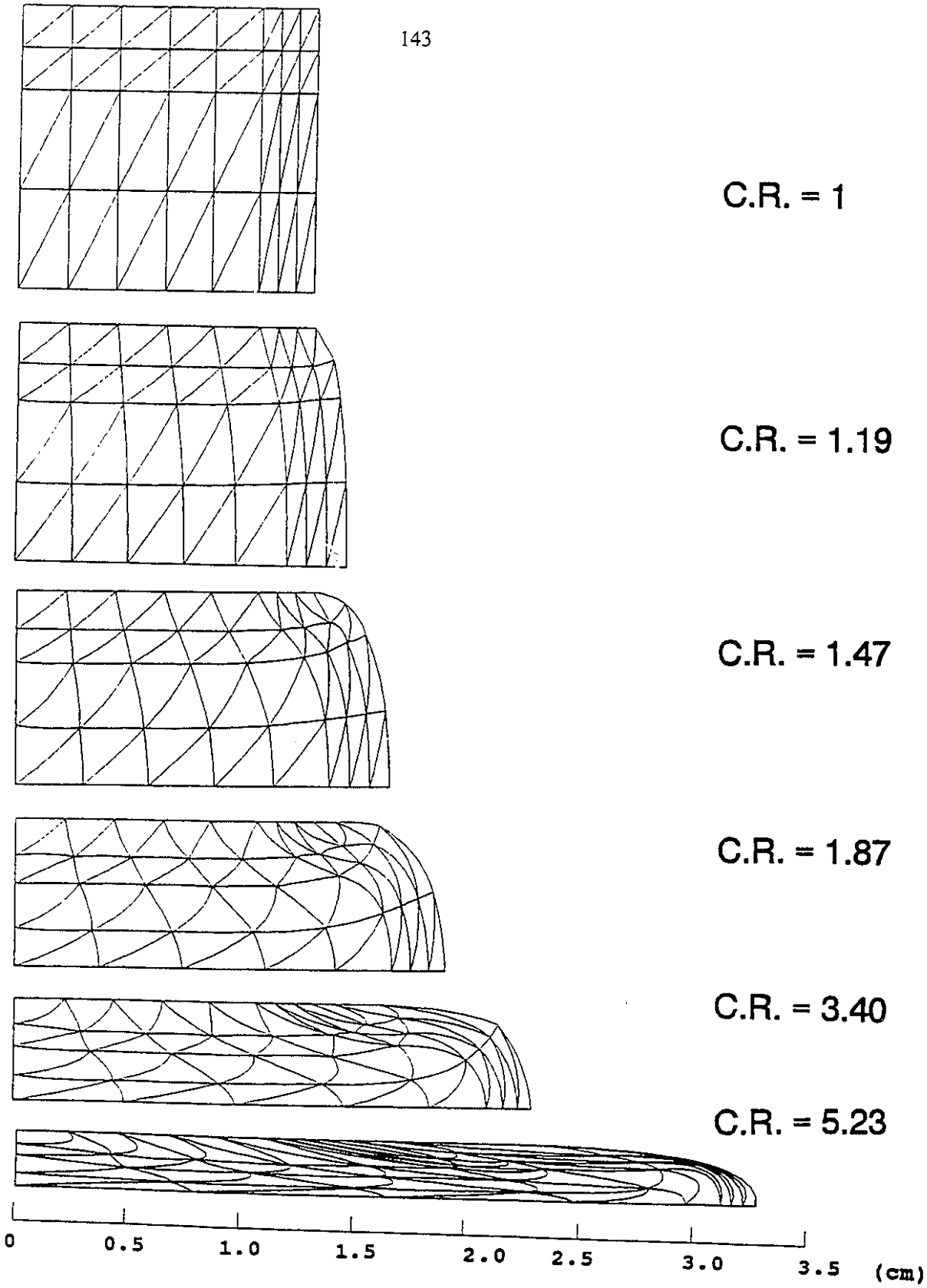

Figure 7.6 Deformed grids during forming process.

vertical and horizontal lines (Figure 7.4) are marked and their motions followed, then the deformation patterns of compression can be clearly observed, as shown in Figures 7.7 and 7.8. Deformation patterns are similar to flow patterns observed and predicted by Mavridis et al. (1992) with power-law viscous fluid simulation, as shown in Figures 7.7 and 7.8. Outer surface development, or the contact line is obtained naturally with Lagrangian description and is shown in Figure 7.9. In Eulerian formulation (Mavridis et al.), part of the contact line is a free surface, which has to be considered as an extra unknown. Special care is needed.

Similar to the stress analysis in Chapter 6, stresses can be obtained. For each element contacting with the mold, the average of stresses at the Gaussian quadrature points is obtained as averaged stress for the element. This method of calculation is more accurate than the conventional one used in Chapter 6. In compression, the normal compressive stress distributions on the interface with the upper plate are shown in Figure 7.10 at different compression ratios, which are important to understand the compression process. Current predictions are similar to those made with ABAQUS by Morman and Pan (1987).

7.3.4 Compression Forming without Contact

In laboratory study, the compression forming is sometimes performed without contact so that the outer surface of the cylinder can freely inflate, as performed in our laboratory (Zhang, 1992). This process is also used to measure extensional viscosity, as did Chatraei et al. (1981). Figure 7.11 (a) illustrates a photo of a deformed part obtained by Chatraei et al. A finite element simulation of the present study is shown in Figure 7.11 (b). Due to

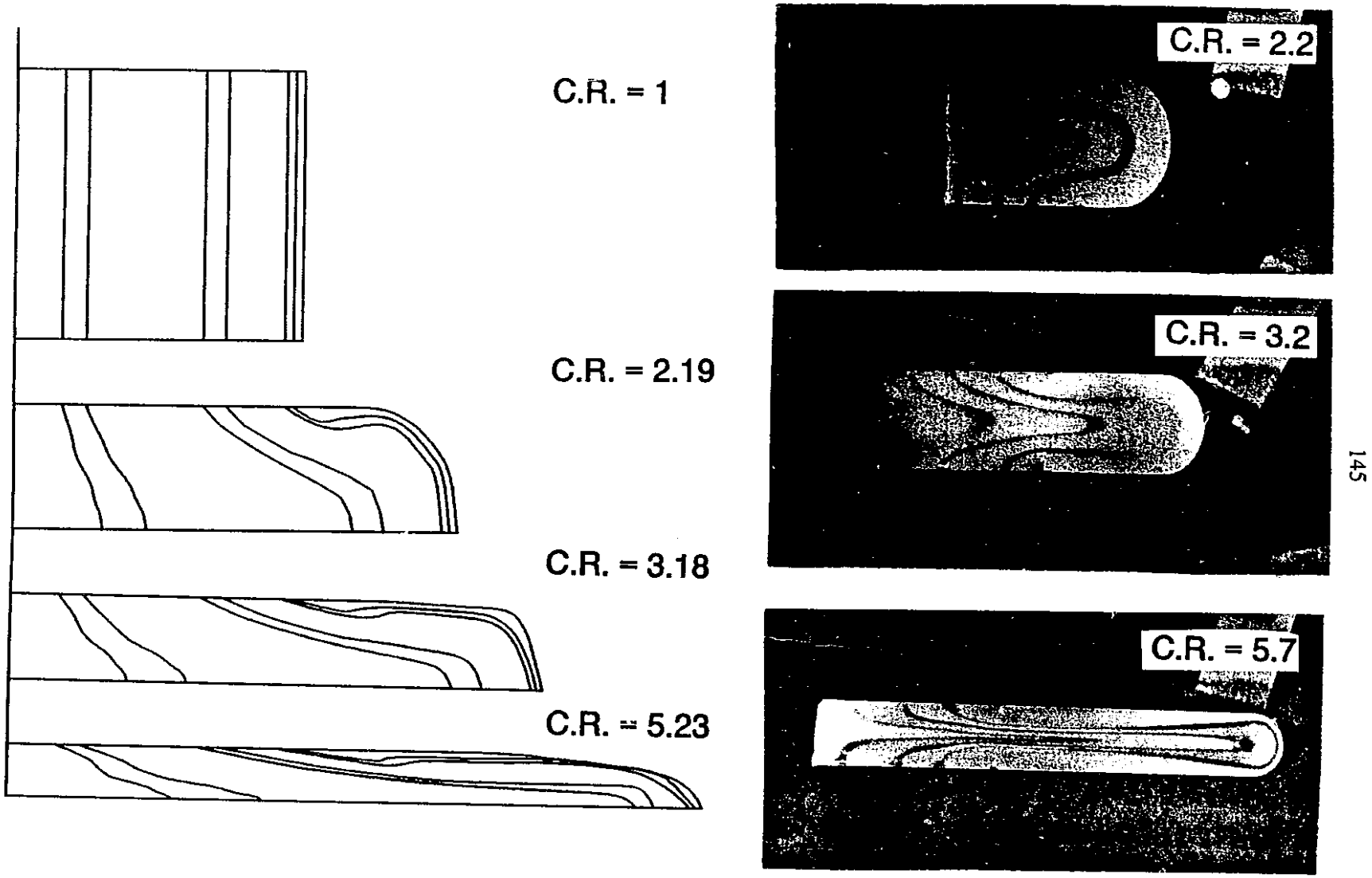

Figure 7.7 A comparison of predicted deformation patterns (evolution of vertical material lines) with experiments by Mavridis, et al. (1992).

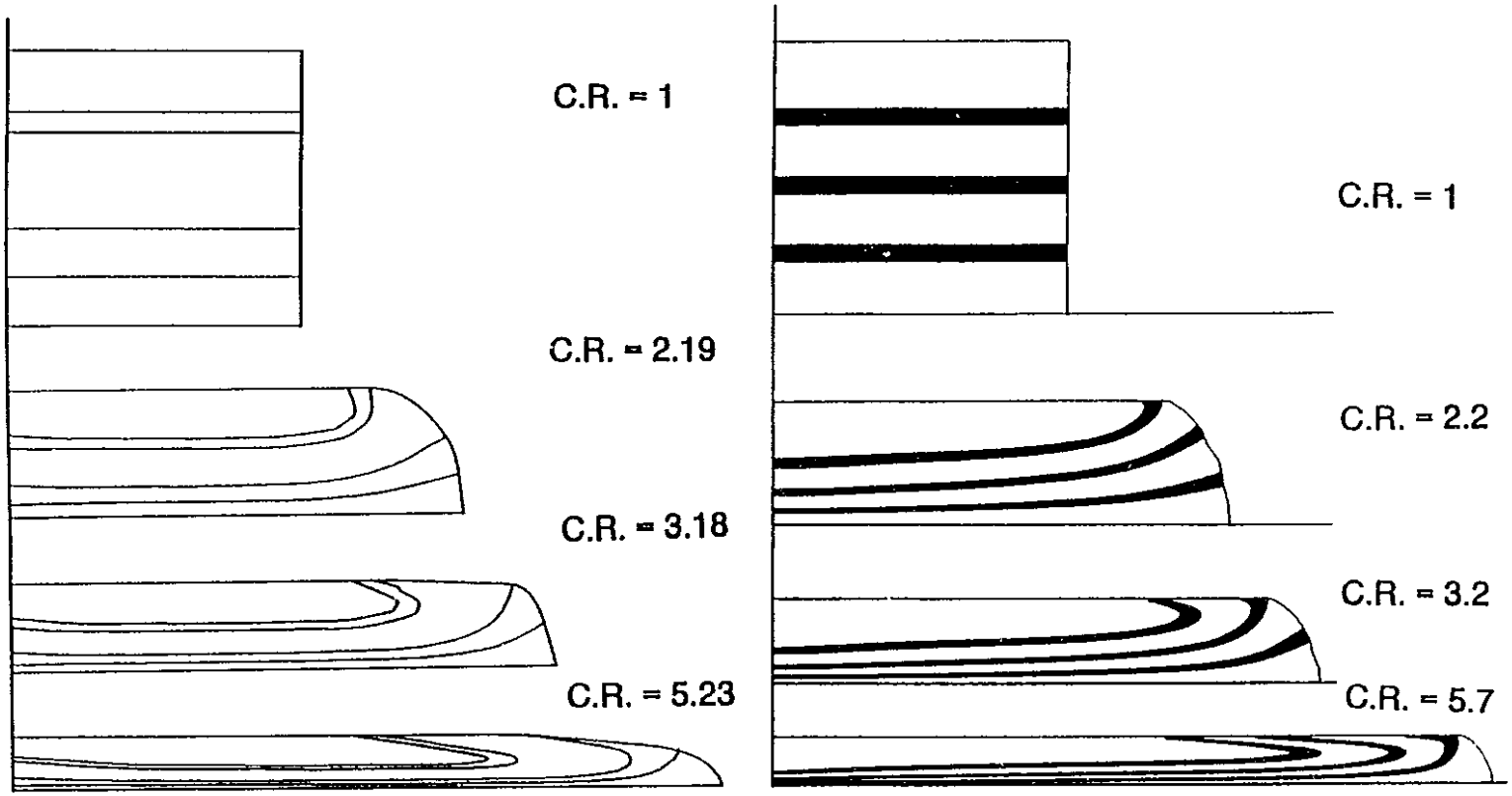

Figure 7.8 A comparison of predicted deformation patterns (evolution of horizontal lines) with predictions by Mavridis, et al. (1992).

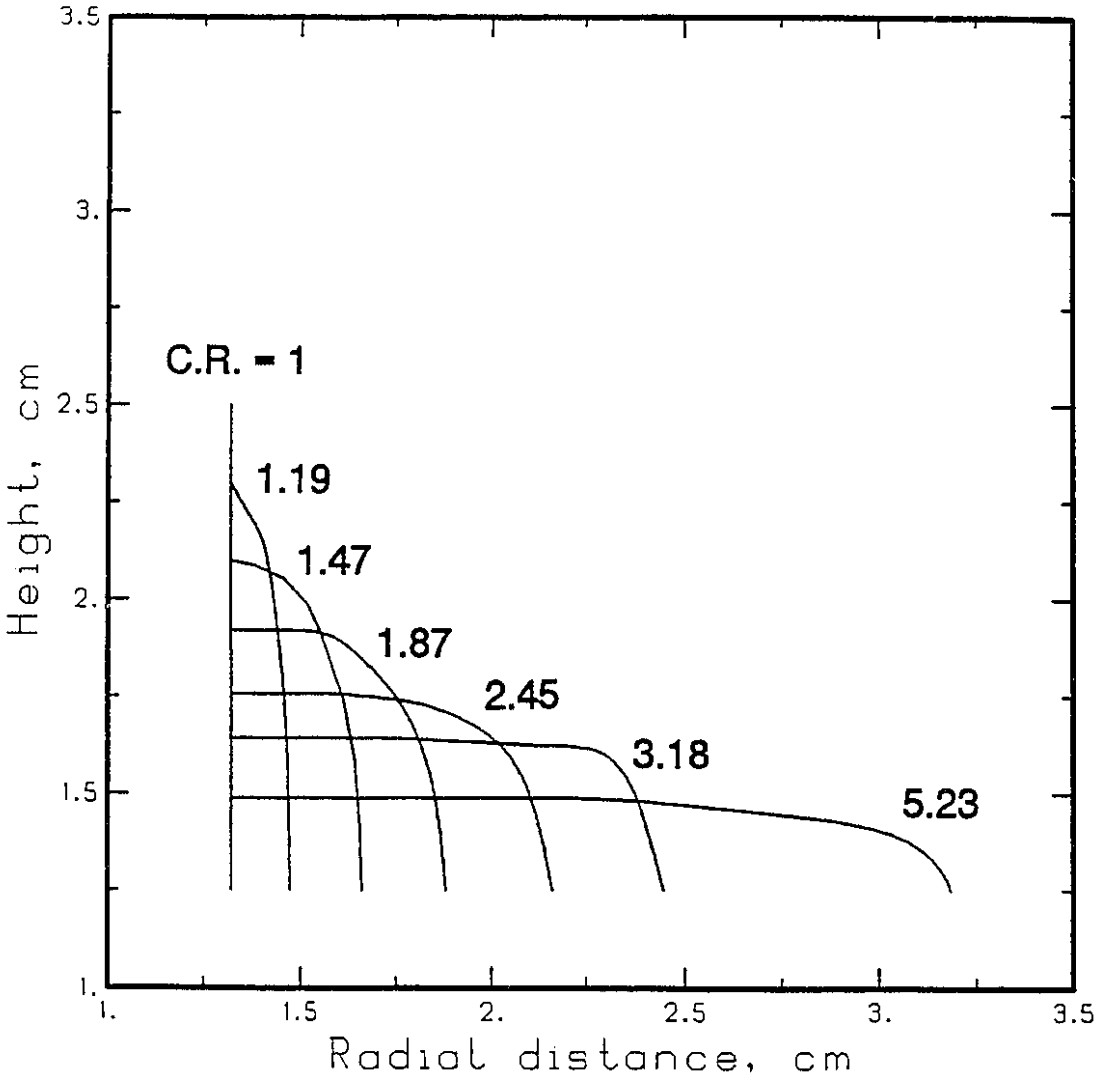

Figure 7.9 Evolution of outer surface during forming.

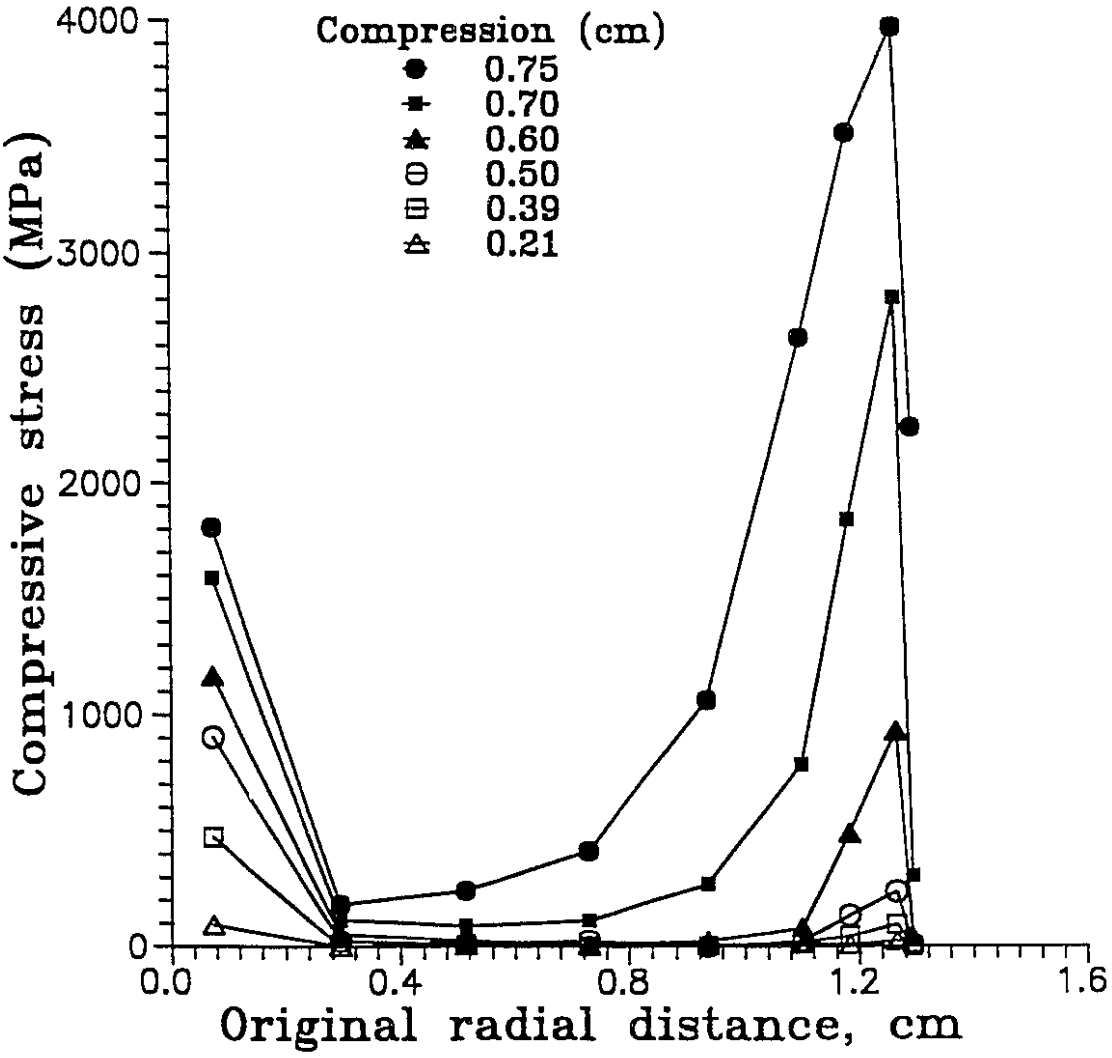

Figure 7.10 Normal stress distributions on mold interface at various compression stages.

lack of experimental data, only a qualitative comparison of deformation pattern is made. The comparison shown in Figure 7.11 indicates good agreement.

7.4 Compression Forming of Reinforced Composite

The finite element program can deal with compression forming of a sandwich composite without difficulty, which is illustrated through the example shown in Figures 7.12 (a) and 7.12 (b), where a strip of much stiffer material (C_{01}=10.0 MPa, C_{10}=1.0) is sandwiched between a softer material (C_{01}=1.0 MPa, C_{10}=0.1). No slip is allowed between the different material layers. Figure 7.12 shows that deformation of the stiffer strip is basically extension. It is smaller than the remaining part and a waist is formed. In Figure 7.13, force curves are given for a homogeneous material with, and without contact, and for the sandwich composite. Clearly, the compression process for composite is much stiffer than the homogeneous material. For the homogeneous material, the force characteristics with, and without contact (with the mold) approach the same curve at large deflection.

7.6 Concluding Remarks

Simulations of compression compare well with available analytical solutions. Deformation characteristics of compression forming can be predicted qualitatively well, compared to experimental observations and predictions by others. The current general finite element program can also predict stress distributions at interfaces between the deformed body and mold, and it can be useful to designers in optimizing their designs of forming processes.

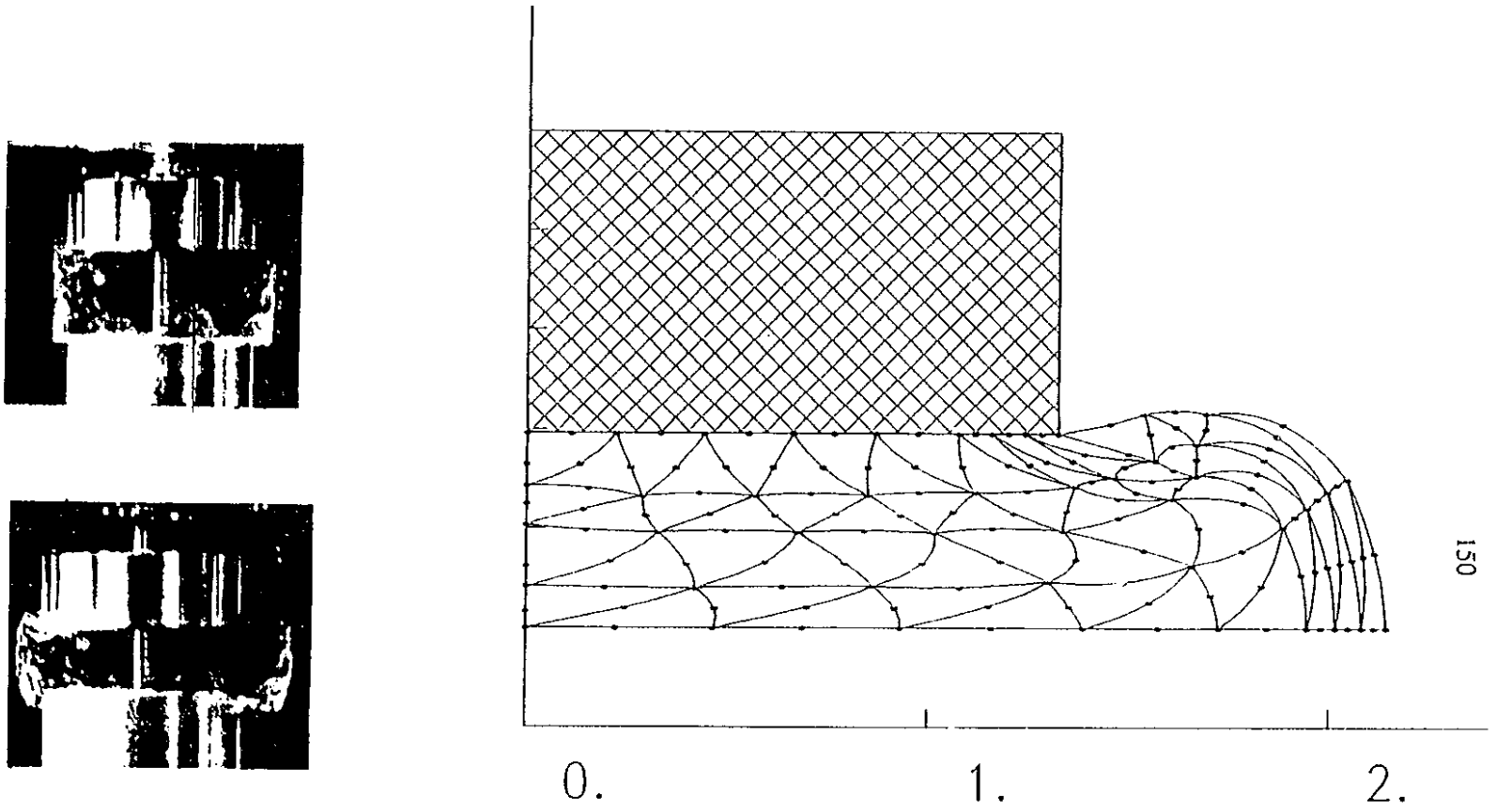

Figure 7.11 Compression of a block without contact (outer surface is free to inflate).

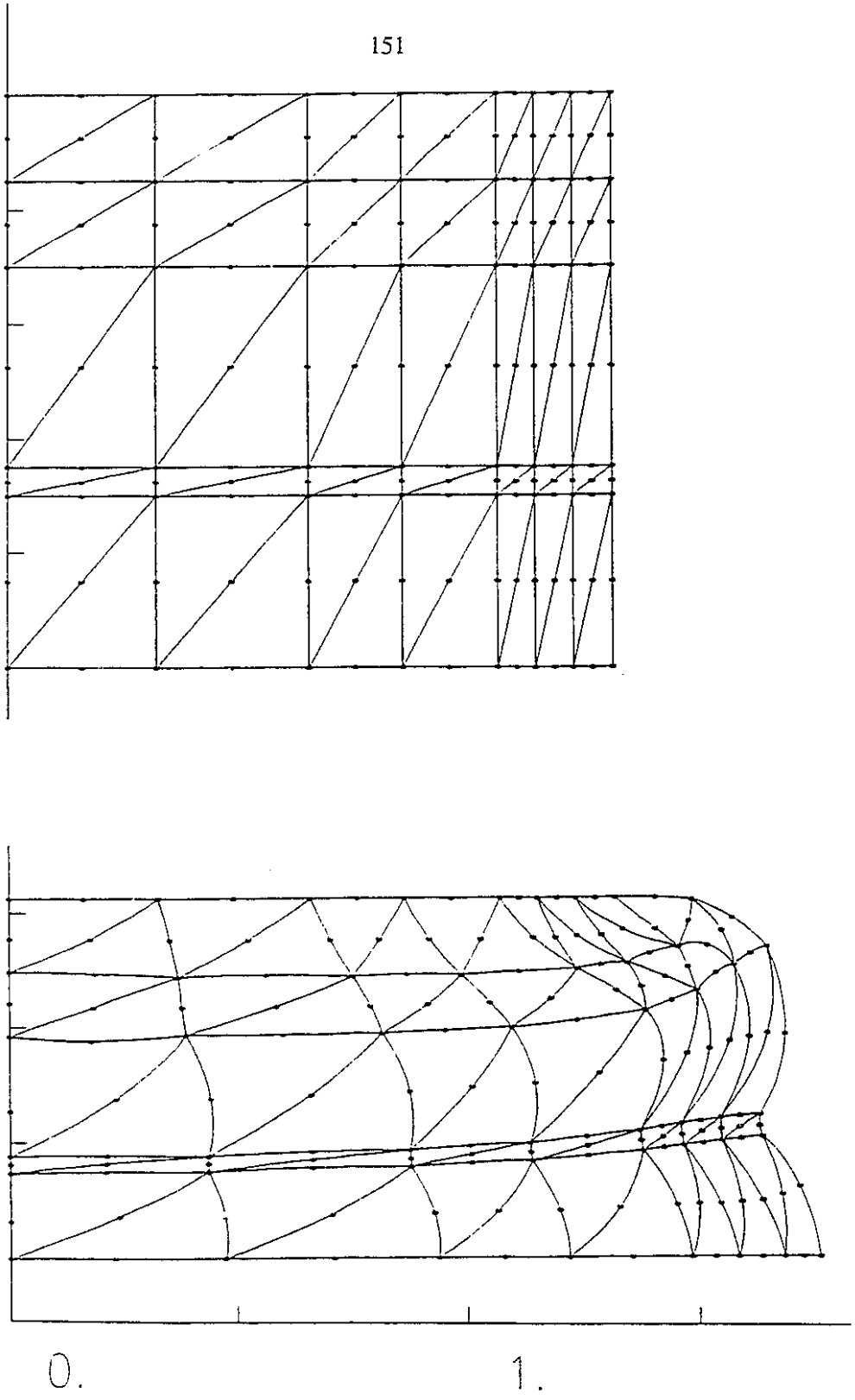

Figure 7.12 Compression of a sandwich composite block.

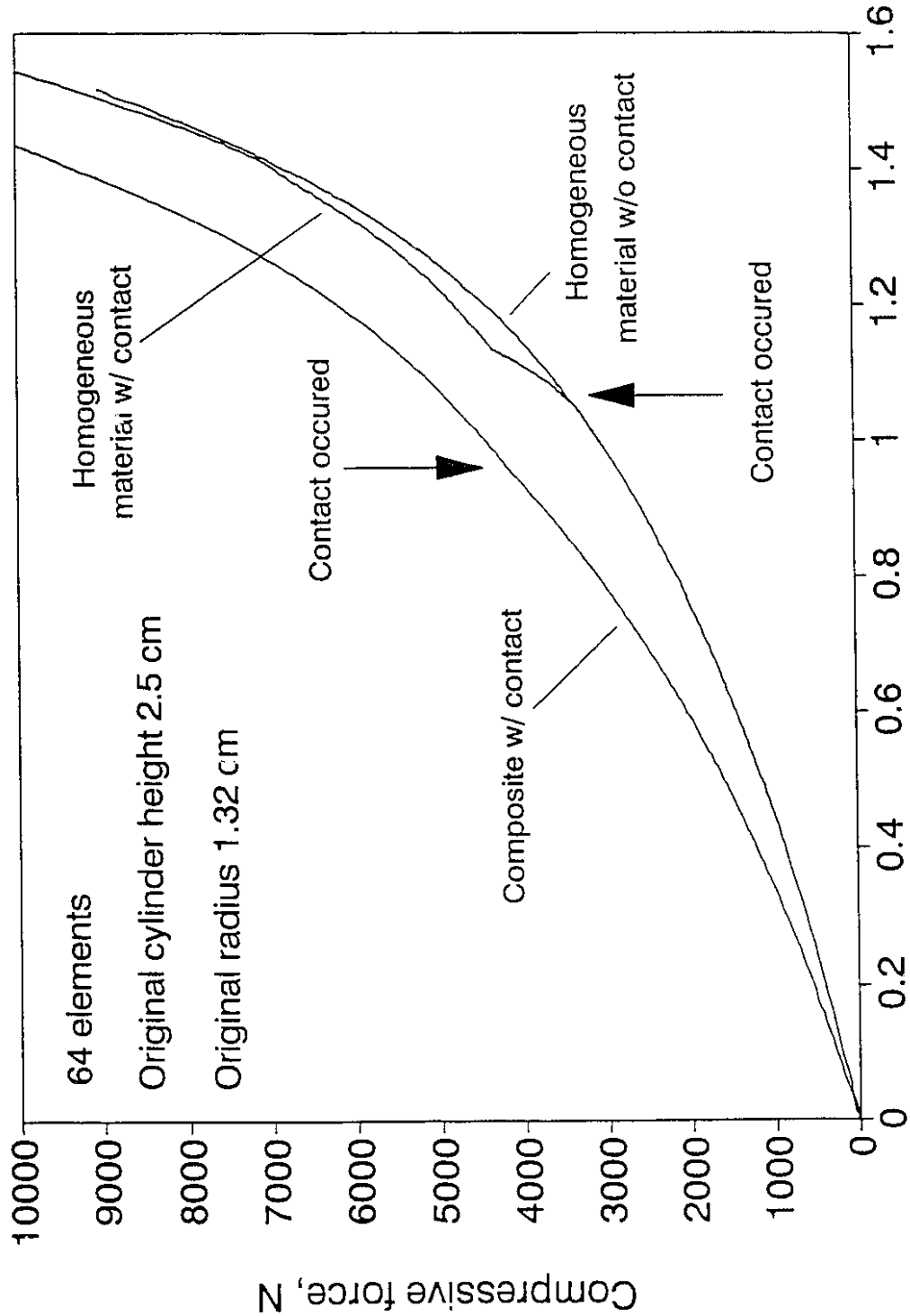

Figure 7.13 Compressive force characteristics of homogeneous material (with and without contact), and of composite material.

CHAPTER 8

CONCLUSIONS AND RECOMMENDATIONS

8.1 Conclusions

Finite element simulations of polymer processing operations have shown great potential to help the industry to achieve processing and product design optimization, reduction of the cycle from design to manufacture, and fabrication of high performance products with less material waste, although such simulations emerged only in the middle of 1980's. This thesis reports on a comprehensive investigation on a variety of polymer forming processes using large deformation finite element analysis. The following main areas are covered:

Theoretical study of the mechanical behavior of polymer solids under the situation of large deformation;

Establishment of large deformation finite element formulation and corresponding solution techniques;

Comprehensive numerical simulations of thermoforming and comparisons with experiments;

Development of algorithms for the simulation of practical forming processes with contact boundary;

Detailed analysis of practical plug-assist forming employing a different finite element algorithm;

Simulations of compression forming.

Polymer forming processes involve nonlinear material behavior of polymers under large deformations. It is found that for thermoplastics in thermoforming there exists a strain energy function, which determines the relationship between strain and stress. Such material is called hyperelastic. Assuming hyperelasticity for thermoplastics in thermoforming is reasonable even for some thermoplastics known as viscoelastic materials, because the forming process is rapid and there is no time for viscous dissipation.

When a material undergoes large deformation, a proper description of motion must be chosen. In this thesis, the total Lagrangian description method is selected due to the ease of tracing material motion. Large deformation characteristics of forming are provided, such as different strain and stress measures.

Simple, efficient large deformation formulations are established. The nonlinearities involved in the forming processes are incorporated, such as large deformation, large strain, moving boundary, contact and material nonlinearities. The incompressibility condition is accurately incorporated by employing the penalty method. The deformation-dependent loading and stiffness are detailed, which requires an unsymmetrical solution technique, which is chosen as unsymmetrical frontal solver in this work.

A modified Riks' method to deal with the limit point is introduced for the first time in the literature to simulate thermoforming. Limit point in thermoforming is a numerical instable point in regular incremental loading plus Newton-Raphson iteration processes, rather than a physical unstable point. The implementation of the algorithm yields good results compared to the

benchmark tests of Treloar (1944). Such comparison has not been reported before.

The nonlinear finite element models developed are capable of dealing with thermoforming of single layer or multilayer composite sheets of finite thickness. A comparison of finite element simulations for inflation of thick, rubber, or PMMA, sheets with experimental data of Treloar, and Lai and Holt (1975) provides good agreement. The application of the hyperelastic constitutive model with proper choice of material constants provides good simulation of practical forming process. Inflation of multilayer composite is also successfully calculated, as is one of the unique features of current modeling. Effects of material parameters on the formed product are discussed, which reveals that nonlinear material properties of polymer must be taken into account in processing design.

Finite element formulations of various contact problems, including frictional contact, are presented. Forming of circular cup and rectangular part are calculated. Small incremental steps are selected to guarantee convergence upon contact.

A slightly different finite element analysis is established for plug-assist forming. Comprehensive comparisons with experimental data of various plug-assist forming processes show again good agreement. Major concerns related to plug-assist forming are studied, such as loading vs. deflection curve, thickness variation, and the effects of material parameter and boundary conditions on the formed part. Detailed strain and stress distributions near the edge and corner of a formed part are obtained which are useful to evaluate the structural properties of the formed product. Comparison of

different processing operations shows that thinner base is predicted in straight vacuum forming, while combined vacuum and plug-assist forming affects thickness distribution dramatically and provides a thicker base. By choosing plug size and plug travelling distance, thickness distribution can be optimized.

The finite element modeling is extended to the simulations of compression forming. Comparison with analytical solutions are conducted. Fountain-like deformation patterns are predicted, which compare qualitatively well with experimental observations and predictions by others. The motion of the free surface is obtained without extra effort in Lagrangian modeling, in contrast to Eulerian fluid mechanics modeling. Stress distribution at interface between deformed body and mold are also obtained.

In this thesis, better understanding of the studied polymer forming processes has been achieved through numerical simulations of the processes. Nonlinear finite element programs are successfully developed and used to predict the practical forming operations. Comparative studies of numerical simulations with experimental results indicate that current analyses capture the fundamental mechanical behavior of polymers in forming and processing characteristics in corresponding forming processes.

8.2 Recommendations

In this thesis, several practical polymer forming problems are successfully simulated with the large deformation finite element analyses developed. To further research in simulation of polymer forming by current methodology, the following recommendations are made:

1. To incorporate more realistic constitutive models in finite element formulation. Viscoelastic model, or elastic-viscoplastic model, can handle broader problems in industrial forming operations. For example, wrinkling may happen after removing formed part from mold. While in compression forming, the deformed body retains its deformed shape and spring-back deformation is observed. Elastic-viscoplastic model with yielding should be used to study permanent deformation. When stress relaxation phenomena are studied, viscoelastic model is a better choice. With these material models, similar metal forming operations can be simulated with the finite element analysis.

Material behavior in polymer forming needs to be investigated experimentally, especially in thermoforming, and compression forming, so that better constitutive models and simulations can be obtained. So far, few material data, or good models are available.

Fibre-reinforced plastic composites have drawn more and more engineering applications for their high strength and stiffness. Their deformation behavior in forming should be studied and corresponding material models should be incorporated in finite element analysis.

2. A mixed Lagrangian-Eulerian method is recommended for simulation of compression forming with large compression ratio, as well as an adaptive meshing technique.

3. Non-isothermal condition is common in practical polymer forming. Sometimes, non-uniform heating is intentionally placed in thermoforming to control polymer deformation. At first, the thermal effects concerned can be temperature-dependent material parameters (Song and Meguid, 1993). Then heat transfer, even solidification processes after forming can be considered.

4. Buckling (forming of irregular shaped parts) are often encountered in industrial thermoforming, blow molding, and compression forming. Prediction and elimination of such behavior can have beneficial impact on the industry. The Riks' method is proved to be capable of handling bifurcation (Ramm, 1981).

Theoretically, nonlinear hyperelastic rubber material exhibits path-dependent behavior, and possesses multiple solutions in the range of nonlinear elasticity (Ogden, 1984). It is an open question that whether the non-uniqueness of solution for the rubber-like plastics plays any role in thermoforming if either loading, or process parameters experience small perturbation.

REFERENCES

"ABAQUS — Theory Manual", Hibbitt, Karlsson, and Sorensen, Inc., Providence, Rhode Island, 1988.

"ADINA — A Finite Element Program for Automatic Dynamic Incremental Nonlinear Analysis", Report AE 84-1, ADINA Engineering, Watertown, MA, 1984.

Alexander, H. "A Constitutive Relation for Rubber-like Materials." *Int. J. Eng. Sci.*, **6**, 549-563 (1968).

Allard, R., J.-M. Charrier, A. Ghosh, M.Marangou, M.E.Ryan, S. Shrivastava, and R. Wu "An Engineering Study of the Thermoforming Process: Experimental and Theoretical Considerations." *J. Polym. Eng.*, **6**, 363-394 (1986).

Argyris, J.H., J.St. Doltsinis, W.C. Knudson, J. Szimmat, K.J.Willam, and H. Wüstenberg "Computational Methods in nonlinear Mechanics." (J.T. Oden, ed.), *Proc. TICOM 2nd Int. Conf.*, 13-66, 1979.

Argyris, J.H., and S.P., Symeonidis, "A sequel to: Nonlinear Finite Element Analysis of Elastic System Under Nonconservative Loading-Natural Formulation, Part I. Quasistatic Problems", *Comput. Meth. Appl. Mech. Eng.*, **26**, 377-384 (1981).

Argyris, J.H., J.St. Doltsinis, H. Fischer, and and H. Wüstenberg, *Comput. Meth. Appl. Mech. Eng.*, **51** 289-362, (1985).

Babuska, I., *Int. J. Numer. Meth. Eng.*, **20**, 1085-1109, 1111-1129, and 2311-2324 (1984).

Bay, F. and J.L. Chenot, "Introduction of Anisotropy in the Numerical Simulation of the Forging Process", *Eng. Comput.* 7, 235-240 (1990).

Bergan, P.G., Horrigmoe, G. Krakeland, B., and Soreide, T.H., "Solution Techniques for Nonlinear Finite Element Problems", *Int. J. Numer. Meth. Eng.*, **12**, 1677-1696 (1978).

Bird, R.B., R.C. Armstrong, and O. Hassager, *Dynamics of Polymeric Liquids*, 2nd ed. Volume 1, John Wiley & Sons, Inc., New York, 1987.

Bruce, G.D., G.J. Vancso and G.C. Weatherly, *Appl. Polym. Sci.*, to appear 1992

Carey, G.F. and J.T. Oden, "*Finite Elements: A Second Course*", Prentice-Hall, Inc., Englewood Cliffs, NJ, 1983.

Chan, S.K., and I.S. Tuba, *Int. J. Mech. Sci.*, **13**, 615-639 (1971).

Chatraei, SH., C.W. Macosko, and H.H. Winter, *J. Rheol.* **25**, 433-443 (1981)

Cheng, J.-H. and N. Kikuchi, *Comput. Meth. Appl. Mech. Eng.*, **49**, 71-108 (1985).

Chung, K., "Finite Element Simulation of PET Stretch/Bolw-Molding Process", *J. Mat. Shap. Tech.*, 7, 229-239 (1989).

Crisfield, M.A., "A Fast Incremental/Iterative Solution Procedure that Handles Snap-Through", *Comput. Struct.*, **13**, 44-62 (1981).

deLorenzi, H.G. and H.F. Nied "Blow Molding and Thermoforming of Plastics: Finite Element Modeling."*Comput. Struct.*, **26**, 197-206 (1987).

deLorenzi, H.G., and H.F. Nied, "Finite Element Simulation of Thermoforming and Blow Molding.", in *Progress in Polymer Processing*, A.I. Isayev, (ed), Carl Hanser Verlag, München, 1991

Denson, C.D. and D.C. Hylton "A Rheometer for Measuring the Viscoelastic Response of Polymer Melts in Arbitrary Planar and Biaxial Extensional Flow Fields." *Polym. Eng. Sci.*, **20**, 535-539 (1980).

Di Pede, S., and R.T. Woodhams, *Polym. Eng. Sci.*, **30**, p. 1185-1199, (1989)

Endo, T., J.T. Oden, E.B. Becker and T. Miller, *Comput. Struct.*, **18**, 899-910 (1984).

Engelman, M., R.L. Sani, P.M. Gresho, and M. Bercovier, *Int. J. Numer. Meth. Fluids*, **2** p. 25 (1982)

Esteghamatian, M., N.G. Zamani, and D.F. Watt, in: Proceeding of the Int. Conf. on Numerical Methods in Industrial Forming Processes, E.G. Thompson, R.D. Wood, O.C. Zienkiewicz, and A. Samuelsson (eds), Rotterdam, the Netherlands, 1989

Florian, J. *Practical Thermoforming, Principles and Applications.* Marcel Dekker, New York, Basel, 1987.

Frados, J., *Plastics Engineering Handbook,* 4th ed., Van Nostrand Reinhold, New York, 1976

Francavalla, A. and O.C. Zienkiewicz, *Int. J. Numer. Meth. Eng.*, **9**, 913-924 (1975).

Gadala, M.S., G. AE. Oravas, and M.A.Dokainish "A Consistent Eulerian Formulation of Large Deformation Problems in Statics and Dynamics." *Int. J. Non-linear Mech.* **18**, 21-35 (1983).

Gadala, M.S., G. AE. Oravas, and M.A. Dokainish, "A Consistent Eulerian Formulation of Large Deformation Analysis with Reference to Metal-Extrusion Process." *Int. J Non-linear Mech.* **23**, 37 (1988).

Garcia-Rejon, A., A. Derdouri, R. Khayat, M.E. Ryan, and W.P. Haessly, *SPE ANTEC Tech. papers*, **49**, p. 836 (1991)

Ghosh, S., in: Proceeding of the Int. Conf. on Numerical Methods in Industrial Forming Processes, E.G. Thompson, R.D. Wood, O.C. Zienkiewicz and A. Samuelsson (eds), Rotterdam, the Netherlands, 1989

Green, A.E. *Theoretical Elasticity.* Clarendon Press, Oxford, 1968.

Halldin, G.W., and Y.C. Lo, "Solid-Phase Flow Behavior of Polymers", *Polym. Eng. Sci.*, **25**, 323-331 (1985).

Hibbit, H.D., P.V. Marcal, and J.R. Rice "A Finite Element Formulation for Problems of Large Strain and Large Displacement." *Int. J. Solids Struct.*, **6**, 1069-1086 (1970).

Hirt, C.W., A.A. Amsden and J.L. Cook, *J. Comput. Phys.*, **14**, 227-253, (1974).

Igl, S.A. and T.A. Osswald, "A Study of the Thermoformability of Woodfiber Filled Polyolefin Composites", *SPE ANTEC Tech. Papers*, **50**, 122-125 (1992).

Isayev, A.I., and A.D. Azari, *Rubber Chem. Technol.*, **59**, 868-882 (1986).

Kalker, J.J., "Aspects of Contact Mechanics", in: Proc. Symp., IUTAM, The Mechanics of the Contact between Deformable Bodies", Delft, 1-25, 1975.

Kennedy, J.M., and T.B. Belytschko, *Nucl. Eng. Des.*, **68**, 129-146 (1981).

Kikuchi, N., and J.T. Oden, *Contact Problems in Elasticity* (SIAM, Philadelphia, PA, 1981).

Kikuchi, N., and J.T. Oden, *Contact Problems in Elasticity: A Study of Variational Inequalities and Finite Element Methods*, SIAM Studies in Applied Math., Philadelphia, 1988.

Kouba, K., O. Bartos, and J. Vlachopoulos, "Computer Simulation of Thermoforming in Complex Shapes", to appear in *Polym. Eng. Sci.*, 1992.

Kouba, K., M.O. Ghafur, and J. Vlachopoulos, "Computer Modeling of Blow Molding", to be presented on *SPE ANTEC'93*, New Orleans, May, 1993.

Kueppers, M. and W. Michaeli "Simulation of the Stretching Process of Complex Geometries with Respect to Thermoforming Conditions." *SPE ANTEC'90 Tech. Papers*, **48**, 462-464 (1990).

Lai, M.O. and D.L. Holt, (a) "The Extensional Flow of Poly-methyl-methacrylate and High-Impact Polystyrene at Thermoforming Temperatures." *J. Appl. Polym. Sci.*, **19**, 1209-1220 (1975).

Lai, M.O. and D.L. Holt, (b) "Thickness Variation in the Thermoforming of Poly(methyl Methacrylate) and High-Impact Polystyrene Sheets." *J. Appl. Polym. Sci* , **19**, 1805-1814 (1975).

Larson, R.G., *Constitutive Equations for Polymer Melts and Solutions*, Butterworths, Stoneham, MA. 1988.

Lee, L.J., J.D. Fan, J. Kim, and Y.-T. Im, *Int. Polym. Processing*, **6**, 61 (1991)

Leider, P.J., and R.B. Bird, *Ind. Eng. Chem. Fundam.* **13**, 336-341 (1974).

Leider, P.J., "Squeezing Flow Between Parallel Disks. II. Experimental Results", *Ind. Eng. Chem. Fundam.*, **13**, 342-346 (1974).

Lindley, P.B., "Engineering Design with Natural Rubber", Natural Rubber Technical Bulletin No.8, The Natural Rubber Producers' Research Assoc., London, 1970.

Liu, W.K., T.B. Belytschko, and H. Chang, *Comput. Meth. Appl. Mech. Eng.*, **58**, 227-245, (1986).

Massoni, E. and J.L. Chenot, "3D Finite Element Simulation of Deep-drawing Process", in J.-L. Chenot, R.D. Wood, and O.C. Zienkiewicz, (ed.s), *Proc. 4th Int. Conf. on Numerical Methods in Industrial Forming Processes - NUMIFORM'92*, A.A.Balkema, Valbonne, France, 503-507, 1992.

Malvern, L.E., *Introduction to the Mechanics of a Continuous Medium*, Prentice-Hall, Inc., Englewood Cliffs, N.J., 1969

Mavridis, H., "*Finite Element Studies in Injection Mold Filling*", Ph.D. Thesis, Department of Chemical Engineering, McMaster University, 1988.

Mavridis, H., G.D. Bruce, G.J. Vancso, G.C. Weatherly, and J. Vlachopoulos, "Deformation Patterns in the Compression of Polypropylene Disks: Experiments and Simulation", *J. Rheol.*, **36**, 27-44 (1992).

McMeeking, R.M. and J.R. Rice, "Finite Element Formulations for Problems of Large Elastic-plastic Deformation", *Int. J. Solids Struct*, **11**, 601-616 (1975).

Menges, G. and D. Weinand "Modellierung des Verstreckprozesses beim Warmformen." *Kunststoffe* **78**, 456-460 (1988).

Menezes, M. and D.F. Wa: *SPE ANTEC Tech. Papers*, **50**, 109-113 (1992).

Miller, T.H. "A Finite E ment Study of Instability in Rubber Elasticity." *Ph.D. Thesis*, University of Texas at Austin, 1982.

Morman, K.N., "An Adaption of Finite Linear Viscoelasticity Theory for Rubber-like Viscoelasticity by Use of A Generalized Strain Measure", *Rheol. Acta*, **27**, 3-14 (1988).

Morman, K.N. and T.Y. Pan, *Rubber Chem. Tech.*, **61**, 503-533 (1988).

Mulcahy, C.M. and E.M. Berns "Thermoforming Takes on More Engineering Applications." *Plastics Eng.*, 21-29, Jan. 1990.

Oden, J.T. *Finite Elements of Nonlinear Continua*, McGraw Hill, New York, 1972.

Oden, J.T. and J.E. Key "Analysis of Finite Deformations of Elastic Solids by the Finite Element Method." *Proc. IUTAM Colloq. High Speed Computing Elastic Struct.*, Liège, 65-103, 1971.

Oden, J.T., and N. Kikuchi, *Int. J. Numer. Meth. Eng.*, **18**, 865-877 (1982).
Oden, J.T., and J.A.C. Martins, "models and Computational Methods for Dynamic Friction Phenomena", *Comput. Meth. Appl. Mech. Eng.*, **52**, 527-634 (1985).

Ogden, R.W., "Large Deformation Isotropic Elasticity — on the Correlation of Theory and Experiment for Incompressible Rubberlike Solids", *Proc. R. Soc. Lond.* **A326**, 565-584 (1972).

Ogden, R.W., *Non-linear Elastic Deformations*, Ellis Horwood Ltd., West Sussex, England, 1984.

Poller, S. and W. Michaeli, *SPE ANTEC Tech. Papers*, **50**, 104-108 (1992).

Ramm, B. *"Strategies for Tracing the Nonlinear Response Near Limit Points."* in W. Wunderlich, E. Stein, and K.-J. Bathe (eds.), *Non-linear Finite Element Analysis in Structural Mechanics*, Springer-Verlag, New York, 63-89, 1981.

Rhi-Sausi, J. and J.M. Dealy "A Biaxial Extensiometer for Molten Plastics." *Polym. Eng. Sci.*, **21**, 227-232, (1981).

Riks, E., "An Incremental Approach to The Solution of Snapping and Bucking Problems", *Int. J. Solids Strct.*, **15**, 529-551 (1979).

Rogers, T.G., "Squeezing Flow of Fibre-reinforced Viscous Fluids", *J. Eng. Math.* **23**, 81-89 (1989).

Rothert, H., H. Idelberger, W. Jacobi and L. Niemann, *Comput. Meth. Appl. Mech. Eng.*, **51**, 139-155 (1985).

Schmidt, F.M., J.F. Agassant and M. Bellet, "Numerical Simulation of Polyester Stretch-Blow Molding Process", in J.-L. Chenot, R.D. Wood, and O.C. Zienkiewicz, (ed.s), *Proc. 4th Int. Conf. on Numerical Methods in Industrial Forming Processes - NUMIFORM'92*, A.A.Balkema, Valbonne, France, 383-388, 1992.

Schmidt, L.R. and J.F. Carley,(a) "Biaxial Stretching of Heat-Softened Plastic Sheets Using an Inflation Technique." *Int. J. Eng. Sci.* **13**, 563-578 (1975).

Schmidt, L.R. and J.F. Carley,(b) "Biaxial Stretching of Heat-Softened Plastic Sheets: Experiments and Results." *Polym. Eng.Sci.*, **15**, 51-62 (1975).

Scott, J.R., *Trans. Inst. Rubber Ind.*, 7, 169-186 (1931); **10**, 481-493 (1935).

Segerlind, L. J., *Applied Finite Element Analysis*, Wiley, New York, 1975.

Shih, A.J.M. and H.T.Y. Yang, "Experimental and Finite Element Simulation Methods for Rate-depdent Metal Forming Processes", *Int. J. Numer. Meth. Eng.*, **31**, 345-367 (1991).

Song, W.N., F.A. Mirza, and J. Vlachopoulos, (a) *J. Rheol.*, **35** p.93-111 (1991)

Song, W.N., K. Kouba, F.A. Mirza, and J. Vlachopoulos, (b) *SPE ANTEC Tech. papers*, **49**, 1025-1027 (1991).

Song, W.N., F.A. Mirza, and J. Vlachopoulos, "Finite Element Simulation of Plug-assis Forming", *Int. Polym. Processing*, **7**, 248-256 (1992).

Song, W.N., "Study of Mechanical Behavior of Polymer Solids", report, Dept. of Civil Eng., McMaster Univ., 1993.

Song, W.N., (a), "A Phenomenological Viscosity Model for Non-Newtonian Fluid", and (b),"The Role of Extensional Viscosity in Entry Flow", to be presented at the 64th Annual Meeting of the Society of Rheology, Santa Barbara, CA, Feb., 1993.

Song, W.N., and S.A. Meguid, "Large Deformation Finite Element Analysis of Various Thermoforming Processes", to be presented at *SPE ANTEC'93*, New Orleans, May, (1993).

Stein, E., and R. Ahmad, "An Equilibrium for Stress Calculation Using Finite Element Displacement Models", *Comp. Meth. Appl. Mech. Eng.*, **10**, 175-198 (1977)

Suh, N.P., and H.C. Sin, "The Genesis of Friction", *Wear*, **69**, 91-114 (1981).

Tanner, R.I., *ASLE Trans.*, **8**, 179 (1965).

Tanner, R.I., *Ind. Eng. Chem. Fund.* **5**, 55-59 (1966).

Timoshenko, S. and J.N. Goodier, *Theory of Elasticity*, 3rd ed., McGram--Hill, NY., 1968.

Thornton, J.S., and D.A. Dillard, "Analysis of Interfacial Stresses for Elastomeric Disks in Compression", *Polym. Eng. Sci.*, **28**, 655-659 (1988).

Throne, J. *Thermoforming*. Hanser Publishers, New York, 1987.

Throne, J.L., *Adv. Polym. Technol.*, 9, p. 309-320 (1989)

Throne, J.L., *Adv. Polym. Technol.*, **10**, p. 75-76 (1990)

Treloar, L.R.G. (a) "Strains in an Inflated Rubber Sheet, and the Mechanism of Bursting." *Trans. Inst. Rubber Ind.* **19**, 201-212 (1944).

Treloar, L.R.G. (b) "Stress-Strain Data for Vulcanized Rubber under Various Types of Deformation." *Trans. Faraday Soc.*, **40**, 59-70 (1944).

Treloar, L.R.G. "*The Physics of Rubber Elasticity.*" 3rd ed. Oxford University Press, London, 1975

Treloar, L.R.G. "The Mechanics of Rubber Elasticity." *Proc. R. Soc. Lond. A* **351**, 301-330 (1976).

Tucker III, C.L., ed., *Fundamentals of Computer Modeling for Polymer Processing*, Carl Hanser Verlag, Münich, 1989.

Vancso, G.J., G.D. Bruce and G.C. Weatherly, *Polym. Comm.*, **31**, 272 (1990).

Vlachopoulos, J., N. Silvi, and J. Vleck, "A Finite Element Package for Molten Polymer Flow", in "Computer-Aided Engineering for Polymer Processing: Application to Extrusion and other Continuous Processes", K.T. O'Brien, ed., Hanser Verlag, Münich, 1992.

Warby, M.K. and J.R. Whiteman "Finite Element Model of Viscoelastic Membrane Deformation." *Comput. Meth. Appl. Mech. Eng.*, **68**, 33-54 (1988)

Ward, I.M., *Mechanical Properties of Solid Polymers*, second edition, J. Wiley, London, 1983.

Washizu, K., *Variational Methods in Elasticity and Plasticity*, 3rd ed., Pergamon Press, Oxford, England, 1982.

Wennerstorm, H., A. Samuelsson, and K. Mattiasson, "Finite Element Method for Sheet Metal Stretching", in *Numerical Analysis of Forming Processes*, J. Wiley, New York, 1984.

Whiteside, R. "Compression Molding", 258-262, and "Thermoforming." 318 - 322, in *Modern Plastics Encyclopedia*, R. Juran (ed.), McGraw Hill, N.J., 1990.

Williams, J.G., *J. Strain Anal.*, **5**, p. 49-57 (1970)

Williams, J.G., and H. Ford, *J. Mech. Eng. Sci.*, **6**, p. 405-417 (1964)

Wilson, E.A. and B. Parsons, *Int. J. Numer. Meth. Eng.*, **2**, 387-395 (1970).

Wolfe, M.A., *Numerical Methods for Unconstrained Optimization — An Introduction*, Van Nostrand Rheinhold, New York, 1978.

Wong, Y.S., and M. Hafez, "Application of Conjugate Gradient Nethods to Transonic Finite Difference and Finite Element Calculations", **AIAA J., 20**, 1526-1533 (1982).

Yamada, Y., Y. Ezawa, I. Nishiguchi and M. Okabe, *Trans. 5th Int. Conf. on SMIRT* (1979).

Zamani, N.G., D.F. Watt, and M. Esteghamatian "Status of the Finite Element Method in the Thermoforming Process." *Int. J. Numer. Meth. Eng.*, **37**, 2681-2693 (1989).

Zhang, W.P., "*Squeezing Flow of Polymer Melts*", M. Eng. thesis, Dept. of Chemical Engineering, McMaster University, 1992.

Zhong, Z.H., "Contact Problems with Friction", in: Proc. of the Int. Conf. on Numerical Methods in Industrial Forming Processes, E.G. Thompson, R.D. Wood, O.C. Zienkiewicz, and A. Samuelsson (eds), 599-606, Rotterdam, the Netherlands, 1989

Zienkiewicz, O.C., "Constrained Variational Principles and Penalty Function Methods in Finite Element Analysis", in G.A. Watson (ed.), *Lecture Notes in Mathematics: Conference on the Numerical Solution of Differential Equations*, Springer-Verlag, Berlin, 207-214 (1974).

Zienkiewicz, O.C., and R.L. Taylor, *The Finite Element Method in Engineering Science*, 4th ed., McGraw-Hill Co., London, 1989.